ROCKET BORNE STUDIES OF MESOSPHERE AND AIRGLOW EMISSIONS

Uma Kota

Ph. D. Thesis
July 2008

PHYSICAL RESEARCH LABORATORY,
AHMEDABAD - 380 009, INDIA

ROCKET BORNE STUDIES OF MESOSPHERE AND AIRGLOW EMISSIONS

A thesis submitted to

Gujarat University

for the degree of

Doctor of Philosophy in Physics

by

Uma Kota

July 2008

Space and Atmospheric Sciences Division
PHYSICAL RESEARCH LABORATORY,
AHMEDABAD - 380 009, INDIA

CERTIFICATE

I hereby declare that the work presented in this thesis is original and done by me. It has not formed the basis for the award of any degree or diploma by any University or Institution, except where due acknowledgment has been made in the text.

Uma Kota
(Author)

Certified by :

Prof. H. S. S. Sinha
(Thesis Supervisor)
Space and Atmospheric Sciences Division,
Physical Research Laboratory,
Navrangpura, Ahmedabad, INDIA

In the memory of

Late Shri. Malladi Sree Rama Sarma

&

Late Smt. Kota Krishna Veni

Acknowledgements

I thank everyone for all the help, advice, support, inspiration and encouragement that I received during the past five years which ultimately resulted in this thesis. I thank God for giving me the courage to face and strength to sail through all hurdles that came my way and finally complete my Ph.D.

I thank,

Prof. H. S. S. Sinha, *my thesis supervisor, for his guidance and support during all these years. His expertise in the field and research insights have been of immense help. He is a constant driving force and a person full of positive energy, who helped me out of many problems during my Ph.D. The encouragement and strength he gave made me complete this thesis successfully.*

Prof. Shyam Lal, *for his constant support and encouragement during all these years.*

Our group - Mr.R.N.Misra, Mr.M.B.Dadhania, Swaroop da, Gohil ji and Mr.N.Dutt, *for their immense help through out my five-year tenure, especially during the fabrication of all those rocket payloads. All of us had a great time during the field trips and I thank them for the support they had given me through out.*

Som Kumar Sarma (and family), *A never ending source of encouragement, a friend, guide and philosopher and a great person to share office with.*

Dr. Raghu, *my mentor. I fall short of words to thank him for the support he gave me. I offer my special thanks to him for introducing me to the world of wavelets.*

Prof. Panigrahi, *for all those discussions on wavelets. I have gained immensely from his vast knowledge in the subject. I thank him for all the time he spared for me.*

Prof. D. N. Madhusudhan Rao, *my teacher at Andhra University. His blessings made me reach here.*

The RSR team at VSSC, Trivandrum, *for their technical support during the rocket flights.*

The NARL team at Gadanki, Tirupati, especially Dr. A. K. Patra, *for providing the MST radar data.*

World Data Center C2 for Airglow, *for providing free access to the data.*

The workshop, *who have really toiled and finally made the payloads. I thank the personnel of the Computer Center, Library, Canteen, Accounts and all other sections of Administration for their help and support.*

Profs. Harish Chandra, *A. Jayaraman, S. A. Haider, R. Sekar, D. Pallamraju, K. P. Subramaniam and S. Ramachandran; Drs. Bhas Bapat, Dipu, and Y. B. Acharya; Mrs. Manisha ben, Mr. Pillai and Philips; Nathuramji, and all other members of the Space and Atmospheric Sciences Division; Colleagues and friends - Subimal, Satya, Shreyas, Sasadhar, Neeraj, Manoj, Santosh Bhai and Anuradha Bhabhi, Harish bhai, Rajneesh, Rashmi and Charan, Antra, Vandana, Charu, Latha, Kushwaha, Gyan, Sumanta, Shuchita, Sumita, Sarika, and all other students especially the tea-time teams starting from 2003; Dr. Nandita Srivastav, Mrs. Pauline, Preeti, Parul, Vijaya, Nishtha, Leela, Uma Desai, Joshi and Nandini, Ms. Jayashree, Late Mrs. Purobi, and all others in PRL's Women's Association; Mr. P. Raghavan, Shaikh ji, Keyur, Jigar, Sivadasan and everybody in PRL who have helped me directly or indirectly during the past five years.*

Directors, *Profs. J. N. Goswami and G. S. Agarwal; Deans, Profs. A. K. Singhvi, S. K. Bhattacharya and V. B. Sheorey. My special thanks are due to Dr. P. Sharma. I* *also offer my sincere thanks to the members of academic committees and experts of all reviews for their comments and suggestions. I also thank all the faculty members who taught me during the course work (2003-04).*

Everyone who have gone through the thesis very carefully and their valuable suggestions helped me in bringing it out in its best form.

All my old friends of B.Sc., M. Sc. and UN Course days for their constant encouragement: Radha, Madhu, Madhavi, Narsaiah, Harsha (and Sanjeev), Vikas, Nirvikar. I also thank Prakash and Anuja (Kousi's friends).

Late Shri. Malladi Sree Rama Sarma, my pedananna garu (mausaji), and Late Smt. Kota Krishna Veni, my attayya (bua), whose blessings were always with me. Unfortunately both of them passed away recently and I would like to pay my tributes to them by dedicating this thesis.

Finally, I thank my family (for tolerating me and my tantrums) - ***Sanat, Kousi, Mom and Dad****, Parents-in-law and Sisters-in-law, Srikanth, Bindu. And above all, my eight-month old son* ***Adi****, for not keeping me awake during the nights. I have deprived him of many things as I could not give him sufficient time; my apologies and I promise to spend more quality time with him and with my other family members from now on.*

HURRAY! It's finally DONE!!!

Uma.

Contents

List of Tables

List of Figures

Abstract

The work presented in this thesis deals with two important issues related to the mesosphere. The first one is the neutral turbulence, produced mostly due to breaking of gravity waves. It is an important heating source in this region. The second issue is the long term variations in the OI 557.7 nm mesospheric airglow emission.

Chapter 1 gives a brief introduction to the Earth's atmosphere and its structure, the hydrostatic equilibrium, gravity waves and tides. It is followed by a detailed introduction to the mesospheric neutral turbulence and mesospheric green line emission. In the turbulence section, the Kolmogorov's theory, energy cascade process and the various turbulence parameters are discussed. Past rocket borne and radar studies are described in detail. Mesospheric turbulence has been studied extensively by the MST radars at Gadanki (13.5°N, 79.2°E, 6.4°Dip), Jicamarca (11.95°S, 76.87°W) and Shigaraki (35°N, 136°E). Using rocket borne instruments, turbulence was studied by measuring electron, ion and neutral density fluctuations. Due to the limitation of the techniques of analysis of rocket data used in the past the altitude resolution of the turbulence parameters estimated was of the order of few km. In radars this has been improved from a few km to ∼150 m by using smaller pulse widths to probe the atmosphere. In the mesospheric airglow section, the oxygen green line emission is discussed. The emission mechanism is

given in brief, followed by the known long term and the short variations. Ground based as well as satellite based studies show that the semi-annual, annual and the quasi-biennial oscillations are seen in the green line emission and the amplitudes of the oscillations vary with latitude.

Chapter 2 describes the instrumentation, data and analysis. The first section describes the Langmuir probe, its function, its limitations as a rocket borne sensor of electron density fluctuations, and finally the rocket experiments conducted for the present study. The second section comprises of the description of data of the Langmuir probe for the turbulence study and the photometer data for the airglow study. In both these studies, the continuous wavelet transform is used to obtain time frequency localization. The use of this technique enabled the understanding of the fine structure of the mesospheric turbulence and the temporal variation of the long term oscillations in the mesospheric oxygen airglow. This technique is discussed in detail in the last section of this chapter.

Chapter 3 presents the results of the mesospheric turbulence study. Three rocket flights carrying Langmuir probes were conducted from Sriharikota (14°N, 80°E, 13.8°Dip) and Thumba (8.5°N, 76.9°E, 0.4°Dip). The electron density measurements were used to estimate the turbulence parameters. With the use of the continuous wavelet transform, turbulence parameters could be studied with an altitude resolution of 100 m. The most important result of the present study is the identification of thin layers of turbulence of thickness 100 m. The energy dissipation rate showed an increasing trend with altitude during all the three flights. During the summer flight, the energy dissipation rate was of the order of 10 mW/kg at 75 km and was as high as 500 mW/kg at 87 km. During the equinox flight, the energy dissipation rates were an order of magnitude smaller. At 75 km, it was 1 mW/kg and at 85 km, it was 30 mW/kg. During the winter flight, weak turbulence was observed and the energy dissipation rate was less than 10 mW/kg below 80 km. Anisotropic turbulence, effects of geomagnetic storm and electrojet instabilities are also discussed.

Chapter 4 presents the results from the mesospheric airglow study. An analysis of 16 years long ground based photometric data of the oxygen green line (557.7 nm) over a mid latitude station Kiso (35.79°N, 137.63°E) was made using the continuous wavelet transform. This analysis shows the presence of semi-annual, annual and quasi-biennial oscillations in the airglow emission. The intensities of these oscillations show inter-annual as well as nocturnal variations. The semi-annual component is present during certain epochs and absent at other times. Also, it is statistically significant at 2000 hrs JST and weakens as the night progresses. This variation is similar to the variation seen in WINDII satellite data and TIME-GCM model predictions. The annual oscillation is present during the entire epoch, but its amplitude shows a minimum during the midnight. In addition, a strong quasi-biennial oscillation is also seen at 2000 and 0200 hrs JST, the amplitude of which exceeds the semi-annual component during certain epochs. This oscillation was not detected in earlier studies using the same data. These variations in the oxygen airglow show the effect of tidal dynamics in the mesosphere and lower thermosphere.

Chapter 5 summarizes the results of the present work. Experiments that can be conducted to improve the present understanding are also discussed.

CHAPTER 1

Introduction

Earth's atmosphere is divided into horizontal layers or *spheres* which have the same temperature gradient, separated by transitional regions called *pauses* (Fig. 1.1). The lowest layer is called the *troposphere*, in which temperature decreases with height upto the *tropopause* to about 190 K at 8 km in polar regions, and 220 K at 18 km at the equator. The main heating process is the absorption of direct solar infrared radiation by water vapour and the re-emitted infrared radiation by the Earth's surface which is absorbed at short wavelengths. Above the tropopause is the *stratosphere*, in which the temperature increases with altitude up to about 260 K at 50 km called the *stratopause*, due to the absorption of solar radiation by ozone. This layer of ozone shields the Earth's surface from harmful solar UV radiation. Above the stratopause is the *mesosphere*, in which the temperature decreases with height to a minimum at the *mesopause* of about 180 K at 85 km. The combination of low absorption of solar radiation, dynamics, and strong cooling due to infrared emission from CO_2, results in the summer mesopause being the coldest place in the terrestrial environment. Temperatures as low as 120 K have been measured in the summer polar mesopause. Above the mesopause is the *thermosphere*, in which

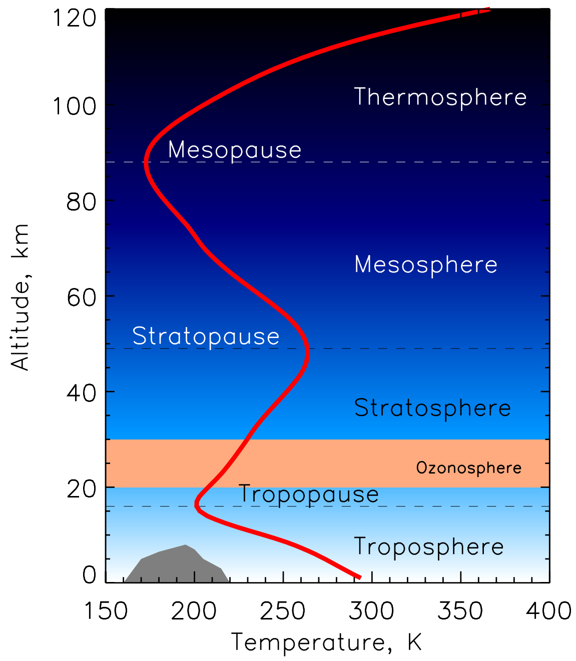

Figure 1.1: *The variation of temperature in the Earth's atmosphere.*

absorption of solar UV and EUV results in a large positive temperature gradient up to about 150-200 km. In the upper thermosphere molecular heat conduction dominates and the temperature remains constant with increasing altitude. The temperature of the thermosphere is a strong function of solar cycle due to the associated large solar cycle variability in UV and EUV radiation. Above ∼600 km is a region called the *exosphere*, in which particles have ballistic orbits and can escape into space.

The atmosphere is also classified on a different basis into regions called *homosphere* and *heterosphere* based on the general homogeneity of chemical composition. Former is the region where principal constituents maintain same relative proportions per unit volume, with about 78% Nitrogen, 21% Oxygen, $<$ 1% Argon and other trace gases. The mean molecular mass remains almost constant, which is approximately 29 kg per 1000 moles. This is the result of eddy diffusion or mixing due to turbulence. Scale height, H, in this region is only a function of temperature, T, and acceleration due to gravity, g, *i.e.,* $H \propto T/g$. Homosphere extends approximately up to a height of 100 km. Above this height eddy diffusion ceases and the molecular diffusion takes over. This region is called the heterosphere and the boundary between the two is termed as *turbopause*. Vertical distribution of a species in the heterosphere depends on its molecular weight, m, and the scale height in this region is therefore a function of molecular weight also, *i.e.*, $H \propto T/mg$. The density of the heavier molecules decreases faster with height. There is little or no nitrogen above 200 km; atomic oxygen dominates between 300 and 1000 km and helium dominates between 1000 and 2000 km with hydrogen above.

In the past different layers of the atmosphere have been studied independent of each other using ground-based, rocket-borne, balloon-borne and satellite-borne instruments. However, it is now very well known that there is a very strong coupling between the various layers of the atmosphere. Coupling between the troposphere, stratosphere and mesosphere, and coupling between the neutral upper atmosphere and the ionosphere have been the subject of study during the past two decades. Coupling includes transport of physical constituents like ozone, atomic oxygen, etc and also the transport of energy and momentum between the various regions of the atmosphere.

1.1 Mesosphere

The mesosphere is the coldest region in the terrestrial atmosphere extending from about 50 to 85 km, with a negative temperature gradient. The temperature minimum occurs at around 85 km and is called the mesopause. Direct solar heating of this region is relatively low and strong cooling due to infrared emission from CO_2 results in the low temperatures. The EUV component of sunlight is primarily absorbed above the mesosphere and most of the UV component is absorbed below. The major heating sources include the absorption of solar radiation in Hartley bands, in the range 242-310 Å by ozone, quenching of $O(^1D)$, stored chemical potential energy due to three body atomic oxygen recombination reaction, exothermicity of hydrogen and ozone reaction, breaking of gravity waves of tropospheric origin, dissipation of tidal energy, adiabatic compressional heating due to vertical motions etc., while the mesospheric cooling is dominated by radiative processes involving CO_2, NO, O and O_3, with radiation from CO_2 playing the dominant role (*Killeen and Johnsson*, 1995).

Mesosphere and the lower thermosphere from 60 to 110 km is still a region of extensive study as it is a transition region from the neutral atmosphere to the ionized atmosphere as well as from the homosphere, where the eddy diffusion dominates, to the heterosphere, where molecular diffusion dominates. Dynamics plays a very important role in this part of the atmosphere. Wave motions over periods from few minutes to few days change the structure and composition of the middle atmosphere considerably. These include gravity waves, of periods less than few hours, tides of periods in fractions of a day and planetary scale waves of longer periods of few days.

1.1.1 Hydrostatic Equilibrium

In the absence of atmospheric motions, the gravitational force acting on a parcel of air of unit volume must be exactly balanced by the vertical component of the pressure gradient force. This is called the hydrostatic equilibrium. Hence,

$$\frac{dP}{dz} = -g\rho \tag{1.1}$$

where P is the pressure, g is the acceleration due to gravity and ρ is the gas density. The ideal gas law,

$$P = nkT \tag{1.2}$$

where n is the number of molecules, k is the Boltzmann constant ($k = 1.38 \times 10^{-23}$ JK^{-1}) and T is the temperature, can be written as

$$P = \frac{\rho kT}{m} \tag{1.3}$$

where $n = \rho/m$ and m is the mean molecular mass. Eq. 1.1 thus becomes,

$$\frac{dP}{P} = -\frac{dz}{H} \tag{1.4}$$

where $H = kT/mg$, is the scale height. If H is constant, *i.e.,* if the atmosphere is isothermal then the pressure reduces exponentially with geopotential height,

$$P(z) = P_{\circ}e^{-z/H} \tag{1.5}$$

If $T = T(z)$ and $H = H(z)$, then

$$P(z) = P_{\circ} \exp\left(-\int_{\circ}^{z} \frac{dz'}{H(z')}\right) \tag{1.6}$$

Consider the vertical displacement of an air parcel from z to $z + dz$, *i.e.,* from P to $P + dP$. When an air parcel is displaced upwards, it is slightly heavier than the surrounding air and gravity tries to restore it to its original position. However, the inertia of the fluid parcel overshoots it the parcel reaches a position below its rest level and is slightly lighter than the surrounding air. The parcel now floats upwards towards its rest level. The fluid parcel therefore oscillates up and down, pushed by the buoyancy force generated by gravity acting on slight density differences, and balanced by the inertial forces due to the fluid's mass. The frequency of this oscillation is called the Brunt-Väisala frequency, ω_B, and is given by

$$\omega_B^2 = \frac{g}{T}\left\{\frac{dT}{dz} + \Gamma_g\right\} \tag{1.7}$$

where, T is the temperature, dT/dz is the vertical temperature gradient and Γ_g is the adiabatic lapse rate defined as $\Gamma_g = g/C_P$, g is the acceleration due to gravity and C_P is the specific heat of air for constant pressure ($C_P = 1020$ J K^{-1} kg^{-1}).

1.1.2 Gravity waves

Buoyancy waves are also called internal gravity waves, as the restoring force is gravity. In a medium like the atmosphere, where there is no rigid upper boundary, these waves can travel upward. Hence, these waves are important as they transport momentum and energy from the lower atmosphere to the middle atmosphere, produce turbulence, trigger convection and can also affect the mean flow significantly. The concept of gravity waves as a major contributor to motions in the upper atmosphere was first introduced by *Hines* (1960), and that paper has led to many publications describing wave motions in the atmosphere. Most of the motions on time scales of tens of minutes to hours with horizontal wavelengths of few 100 km in the middle atmosphere are ascribed to gravity waves that have propagated from the lower atmosphere. The origin of such waves can be due to tropospheric weather disturbances like large thunderstorms, tropospheric overflow over mountains etc. These disturbances generate atmospheric density fluctuations, which propagate upward and grow in amplitude with height. At mesospheric and lower thermospheric (MLT) altitudes, the amplitude becomes very high and the wave can perturb the atmospheric density and temperature by a few percent. The wave cannot propagate further and it breaks down to generate turbulence. Such diffusion controls the distribution of species such as atomic oxygen (*Garcia and Solomon*, 1985). However, gravity wave generation is a local phenomenon and is sporadic in nature. There is also a gravity wave filtering by the stratospheric wind system which favours the propagation of different gravity waves during different seasons. An eastward stratospheric wind allows the westward propagating gravity waves and *vice versa* (*Baldwin et al.*, 2001; *Fritts et al.*, 2003; *Meriwether and Gerrard*, 2004).

1.1.3 Tides

Atmospheric tides are global-scale periodic oscillations of the atmosphere. The largest-amplitude atmospheric tides are mostly generated in the troposphere and stratosphere when the atmosphere is periodically heated as water vapour and ozone absorb solar radiation during the day. The largest atmospheric tides are the diurnal and the semidiurnal tides of 24 and 12 hour periodicities, respectively. The semidiurnal lunar gravitational tide is next in strength in the upper atmosphere. Diurnal tides can propagate vertically upward only below 30° latitude. At higher latitudes they remain trapped in the atmosphere. With the decreasing importance of the diurnal tide, the semidiurnal tide becomes dominant at latitudes higher than 30°.

Atmospheric tides can be measured as regular fluctuations in wind, temperature, density and pressure and the amplitude of the fluctuations increases with altitude. This amplification is due to the decreasing density of the atmosphere and is a consequence of energy conservation. As tides or gravity waves propagate upwards, they move into regions of lower and lower density. If the tide or wave is not dissipating, then its kinetic energy density must be conserved. Since the density is decreasing, the amplitude of the tide or wave increases correspondingly so that energy is conserved. The amplitude of a wave at a height of z can thus be described by the equation:

$$A = A_0 \exp(\frac{-z}{2H}) \tag{1.8}$$

where A_0 is the initial amplitude of the wave, z is height and H is the scale height of the atmosphere. In accordance with this atmospheric tides have much larger amplitudes in the middle and upper atmosphere than they do at the ground level.

The present work addresses two issues related to the mesosphere and the lower thermosphere. The first one, which is dealt in this thesis, is the neutral turbulence, produced mostly due to breaking of gravity waves. Neutral turbulence is an important heating source in this region. The second issue studied in the present thesis is long term variations in the OI 557.7 nm mesospheric airglow emission.

1.2 Mesospheric Neutral Turbulence

An infinite uniform body of fluid can be characterized by a density ρ and molecular transport coefficients such as viscosity μ. This body of fluid can be set into a variety of motions. It has been observed many times that when kinematic viscosity ν is small, the motions are such that the velocity at any given time and position in the fluid is not found to be same when measured several times under seemingly identical conditions. In these motions velocities take random values which are not determined by the macroscopic or the average properties of the fluid. Fluctuating motion of this kind is called turbulence. And random motion whose average properties are independent of position of the fluid is called homogeneous turbulence.

Mesosphere is a weakly ionized region of the atmosphere. The observed electron density during daytime is of the order of 1000 cm^{-3} at $\sim$ 75 km. The mesosphere is a collision dominated region upto about $\sim$ 90 km and so any turbulence fluctuations seen in this part of the neutral atmosphere are also seen in the electron and the ion densities. *Thrane and Grandal* (1981) have shown that electrons and ions can be used as passive tracers to study neutral turbulence. This assumption implies that the electron and ion concentrations do not change through ion production, recombination or chemical reactions within the characteristic lifetime of an eddy. This assumption is reasonable in the mesosphere, *i.e.,* at heights below 95 km. The lifetime of an eddy is 10 to 100 s in this region whereas the lifetime of an ion against recombination ranges from 200 s at 90 km to 1000 s to 70 km. And hence the use of electrons and ions as tracers of turbulent motion should therefore be permissible in the height region 60-95 km (*Thrane and Grandal*, 1981, and references therein).

1.2.1 Energy Cascade and Kolmogorov's Theory

Consider a fully turbulent flow characterized by a high Reynold's number. Reynold's number is defined as the ratio of inertial forces ($v\rho$) to the viscous forces (μ/l) and consequently it quantifies the relative importance of these two types of forces for given flow conditions.

$$R_e = \frac{\text{Inertial Forces}}{\text{Viscous Forces}} = \frac{u\rho}{\mu/l} = \frac{ul}{\nu} \tag{1.9}$$

where u is the characteristic velocity of the eddy, l is the characteristic length, ρ is the density of the fluid, μ is the dynamic viscosity defined as the coefficient of internal friction developed where fluid regions move adjacent to each other at different velocities and ν is the kinematic viscosity given by μ/ρ, *i.e.,* the ratio of dynamic viscosity to the density of the medium.

The Reynolds number is used to identify laminar or turbulent flow regimes depending upon which force dominates. For fluid flow in a tube, laminar flow occurs at low Reynolds numbers ($R_e < 2100$), where viscous forces are dominant, and is characterized by smooth, constant fluid motion, while on the other hand turbulent flow occurs at high Reynolds numbers ($R_e > 3000$) and is dominated by inertial forces, producing random eddies, vortices and other flow fluctuations. The critical R_e where the flow turns turbulent from laminar however depends on the tube dimensions and other fluid parameters.

Another quantity which indicates formation of turbulence is the Richardson number, defined as

$$R_i = \frac{\omega_B^2}{(du_x/dz)^2} \tag{1.10}$$

where, ω_B is Brunt-Väisala Frequency and du_x/dz is the shear, *i.e.,* the vertical gradient of the horizontal velocity. The critical Richardson number, is about 0.25 (although reported values have ranged from roughly 0.2 to 1.0), and the fluid flow is dynamically unstable and turbulent when $R_i < 0.25$.

The range of spectral scales, for which turbulence exists, is limited by buoyancy forces at the largest scales and by the viscous dissipation at the smaller scales. Turbulence extracts energy from the mean flow at large scales; this energy cascades down to intermediate and then to smaller scales where it is finally lost by viscous dissipation, maintaining the energy balance. This idea of the energy cascade was given by L. F. Richardson in 1922. It was later quantified by A. N. Kolmogorov in 1941. In particular, he identified the smallest scales of turbulence that now bear his name and is known as Kolmogorov microscale.

Turbulence can be thought of as being made up of different Fourier components and $E(k)$ can be regarded as their energy spectrum such that the integration over it gives the total energy in the unit volume.

$$\frac{1}{2}\overline{u}^2 = \int_0^\infty E(k)dk \tag{1.11}$$

where $\overline{u}^2$ is the mean velocity. Eddies of a certain scale size l have some typical velocity u associated with them. The corresponding Reynold's number, $R_e = lu/\nu$, should be large for the larger eddies, *i.e.,* $R_e \gg 1$. The energy cascades down to smaller and smaller eddies, but the eddies cannot be of indefinitely small size. A rough lower limit of these eddies is $l_0 u_0 \approx \nu$, *i.e.,* $R_e \approx 1$.

Energy builds up only at the larger scales and the intermediate eddies merely transmit this energy at a rate of ϵ per unit mass per unit time to the smaller eddies. Kolmogorov postulated that it must be possible to express ϵ in terms of l and u, as the eddies are characterized only by these two parameters. On dimensional grounds

$$\epsilon \approx \frac{u^3}{l}, \tag{1.12}$$

and it must be true for the smallest possible eddy also.

$$\epsilon \approx \frac{u_0^3}{l_0} \tag{1.13}$$

or,

$$u \approx (\epsilon l_0)^{1/3}$$

From Eq. 1.11 one can write on dimensional grounds,

$$E(k)dk \propto u^2$$

or,

$$E(k)k \propto u^2$$
$$E(k)k \propto (\epsilon l)^{2/3}$$
$$E(k)k \propto \{\tfrac{\epsilon}{k}\}^{2/3}$$

or,

$$E(k) \propto \epsilon^{2/3}.k^{-5/3} \tag{1.14}$$

This is the famous $-5/3$ power law. This is not a derivation but a dimensional argument. This region of the spectrum from the buoyancy scale (L_B) to the inner scale (l_0) where the -5/3 law is obeyed is called the Inertial SubRange (ISR). When $R_e \ll 1$, the scale sizes of the eddies are smaller than l_0 and in this region of smaller eddies the energy that has been transmitted from the ISR is lost by viscous dissipation and hence is called the Viscous Dissipation Regime (VDR). The total energy that was transmitted in the ISR should be equal to the energy lost in the VDR. The spectrum here is much steeper and follows a power -7 law (*Heisenberg*, 1949),

$$E(k) \propto k^{-7} \tag{1.15}$$

There are many kinds of turbulent motions encountered in day to day life. Motions in aeronautics, hydraulics are usually more complicated than homogeneous turbulence. First, there is a variation of the mean velocity with position, which normally arises due to the presence of rigid boundaries and secondly there is also a variation in the average properties of the fluctuating velocity with position. Consequently, there will be some kind of interaction between the fluctuating and the mean components of the motion. In other words the rigid boundaries impose steady boundary conditions on the random velocity fields making the problems difficult to handle mathematically. In the mesosphere, where there are no rigid boundaries, the turbulence produced can be assumed to be homogeneous and isotropic. However, the large scale eddies can be anisotropic, affected by the boundary conditions of the flow itself, but as one goes down to smaller scales turbulence becomes homogeneous and isotropic. Hence Kolmogorov's theory can be applied to mesospheric turbulence.

1.2.2 Heisenberg Model

Heisenberg (1948) applied a model, which exhibits the classical $k^{-5/3}$ power law in the inertial subrange and the k^{-7} behavior in the viscous subrange. A smooth transition takes place between these subranges. The frequency spectrum is given by

$$W(\omega) = \left[\frac{\Gamma(5/3)\sin(\pi/3)}{2\pi v_R}\frac{a^2 N_n}{\epsilon^{1/3}} f_\alpha\right] \cdot \left[\frac{(\omega/v_R)^{-5/3}}{\left[1 + \{(\omega/v_R)/k_0\}^{-8/3}\right]^2}\right] \tag{1.16}$$

where Γ is the Gamma function ($\Gamma(5/3) = 0.90167$, which should not be confused with the adiabatic lapse rate), v_R is the rocket velocity. N_n represents the rate at which neutral density fluctuations disappear due to molecular diffusion, ϵ is the energy dissipation rate. The factor f_α (= 1 or 2) takes into account the different normalizations used for N_n (*Lübken*, 1992). The numerical constant a^2 is determined from experiments. Hill (1978) has suggested a^2 = 1.74.

This model assumes that the fluctuations are homogeneous, isotropic, and stationary. These constraints are too strict to be likely in the real atmosphere. The large scales, for example, cannot be isotropic when buoyancy forces are important. However, the present results are mainly based on the inner scale which is of the order of few meters only. The effect of buoyancy forces can therefore be neglected at these scale sizes. But the effects of anisotropy cannot be completely neglected and have to be taken into consideration when discussing the errors involved. According to Kolmogorov's theory the smaller scales eddies are isotropic and hence the inner scales, which are of the order of few tens of meters can be considered isotropic.

1.2.3 Turbulence Parameters

Turbulence parameters can be estimated from the power spectra of electron/ion density fluctuations (*Thrane and Grandal*, 1981; *Thrane et al.*, 1985, 1987; *Chakrabarty et al.*, 1989; *Sinha*, 1992; *Lübken*, 1992; *Lübken et al.*, 1993). Power spectra show a change in the spectral index at the inner scale of turbulence (l_0) which typically is a few tens of meters. Typical values of the inner and outer scales (l_0 and L_B) at mesospheric altitudes are shown in Fig. 1.2 (*Lübken et al.*, 1993). The Kolmogorov microscale η, and the mean free path λ, taken from CIRA-1986 are also shown for comparison. The profiles in Fig. 1.2 are calculated for an energy dissipation rate of $\epsilon = 100$ mW/kg. This is considered a typical order of magnitude value of ϵ in the literature, but it is very different from past measurements (Sec. 1.2.4) and the results of the present work (Chap. 3). As already discussed in the earlier section, for neutral turbulence generated fluctuations, the power spectra shows a spectral index of $-5/3$ in the ISR from inner scale (l_0) to outer scale or the buoyancy scale (L_B) and a spectral index of -7 in the VDR from inner scale to Kolmogorov microscale (η). The innerscale (l_0) can be identified from the best fit of the Heisenberg model to a power spectrum of the electron/ion or neutral density fluctuations. Once l_0 is determined, other turbulence parameters *viz.,* Kolmogorov microscale (η), the

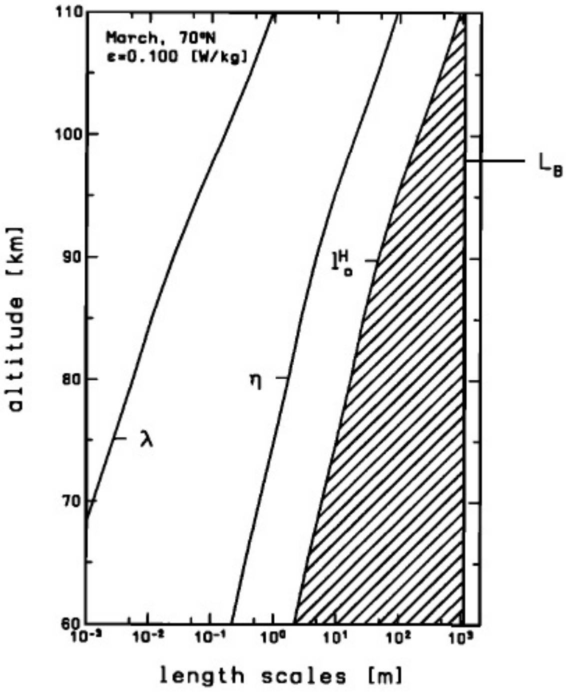

Figure 1.2: *Typical values of turbulence length scales at mesospheric altitudes, calculated for ϵ = 100 mW/kg. The atmospheric background parameters are taken from CIRA-1986 (March, 70°N). The figure is reproduced from Lübken et al. (1993).*

energy dissipation rate (ϵ), the eddy diffusion coefficient (K), vertical turbulent velocity (u_z) and the outer scale (L_B) can been obtained using the following relations. The Kolmogorov microscale, η is computed as (*Hill and Clifford*, 1978; *Sinha*, 1992)

$$\eta = \frac{l_0}{7.4} \tag{1.17}$$

The energy dissipation rate is then given by (*Chen*, 1974; *Weinstock*, 1981a; *Sinha*, 1992)

$$\epsilon = \frac{\nu^3}{\eta^4} \tag{1.18}$$

where ν is the kinematic viscosity and can be obtained from standard atmospheric models. Once ϵ is calculated the heating rate is determined by

$$\frac{\partial T}{\partial t} = \frac{\epsilon}{C_P} = 0.0864\, K/day \tag{1.19}$$

where ϵ is in mW/kg. The Eddy diffusion coefficient K is calculated using the following relation (*Lily et al.*, 1974; *Weinstock*, 1981b; *Sinha*, 1992).

$$K = \frac{0.81\epsilon}{\omega_B^2} \tag{1.20}$$

where, ω_B is the Brunt-Väisala frequency (Eq. 1.7), which is also calculated using the temperature from standard models. The vertical turbulent velocity, u_z, is then computed by the following equation (*Weinstock*, 1981a; *Sinha*, 1992).

$$u_z^2 = \frac{\epsilon}{0.4\omega_B} \tag{1.21}$$

The buoyancy or outer scale of turbulence, L_B, is then given by (*Shur*, 1962; *Lumley*, 1964; *Sinha*, 1992),

$$L_B = \frac{2\pi u_z}{0.9 w_B} \tag{1.22}$$

The percentage amplitude of different scale sizes $A(\lambda)$ can also be computed from power spectral density estimates $P(\lambda)$ using the relation

$$A(\lambda)L = \frac{\{P(\lambda)\}^{\frac{1}{2}}}{N_e} \times 100 \tag{1.23}$$

where N_e is the average electron density in the altitude range considered.

1.2.4 Rocket & Radar Studies of Mesospheric Neutral Turbulence

It is now well established that the Kolmogorov's theory explains the neutral turbulence and the energy cascade process in the mesosphere and the lower thermosphere. What needs to be understood are the morphological characteristics of the turbulence and the impact of turbulence on the energy budget of this region of the atmosphere. A global picture which gives the spatial and the temporal variation of the various turbulence parameters is being investigated by many workers using a number of techniques. Investigation using *in situ* techniques comprising rocket-borne measurements of passive tracers like neutral density fluctuations (*Lübken*, 1992; *Lübken et al.*, 1993; *Rapp et al.*, 2004), ion density fluctuations (*Thrane and Grandal*, 1981; *Thrane et al.*, 1985, 1987; *Blix et al.*, 1990), electron density fluctuations (*Sinha*, 1992; *Goldberg et al.*, 1997; *Lehmacher et al.*, 1997, 2006), wind measurements from chemical release experiments (*Larsen*, 2002) and remote sensing techniques using radars (*Hocking*, 1990; *Hocking and Röttger*, 2001; *Chakravarty et al.*, 2004; *Sheth et al.*, 2006) have been made from various latitudinal zones. Simultaneous measurements using all or some of the above techniques also proved very useful in understanding the mesospheric turbulence in greater detail (*Royrvik and Smith*, 1984; *Croskey et al.*, 2004). The emphasis now is to understand the fine scale structure of the mesospheric turbulence (*Strelnikov et al.*, 2003; *Chakravarty et al.*, 2004; *Sheth et al.*, 2006) using these various techniques.

Thrane and Grandal (1981) observed neutral turbulence from 65 to 95 km with varying intensity from positive ion density measurements by rocket-borne ion probes flown from a high latitude station Andoya (69.3°N, 16°E). *Sinha* (1976) and *Prakash et al.* (1980) detected small-scale electron density irregularities in 60 - 85 km altitude region from rocket-borne Langmuir probe (LP) measurements over the equatorial station Thumba (8.5°N, 77°E) and suggested neutral air turbulence to be the generating mechanism. *Thrane et al.* (1985, 1987) derived the neutral turbulence parameters from ion density measurements from Andoya. *Chakrabarty et al.* (1989) made ion density measurements from Thumba using spherical probe to study the turbulence and also estimated the turbulence parameters. *Sinha* (1992) derived turbulence parameters in 60 - 80 km altitude region from a large number of rocket-borne electron density measurements conducted from Thumba.

One of the most important studies of mesospheric turbulence using rocket-borne measurements was by *Lübken* (1997) over high latitudes, mostly from Andoya (69.3°N, 16°E), using neutral density fluctuations as tracers. A significant and systematic seasonal variation was found where, turbulence is confined to a relatively small height region of 78-97 km during summer but covers the entire mesosphere from 60-100 km during winter. Stronger heating rates of ∼10-20 K/d were observed around the summer mesopause (∼90 km), whereas in winter the turbulent heating rates were comparatively small (typically 0.1 K/d and 1-2 K/d below and above ∼75 km, respectively) in the entire mesosphere and lower thermosphere. *Lübken* (1997) concluded that turbulent heating in the mesosphere is strongest at the coldest part of the atmosphere, namely, at the polar mesopause in summer. The observations imply that turbulent heating is an important contribution to the energy budget of the upper mesosphere in summer, whereas it is presumably negligible in the entire mesosphere in winter. However, during the

MaCWAVE/MIDAS summer campaign conducted from Andoya during July 2002, turbulence was observed below 80 km also (*Rapp et al.*, 2004). This was a result of large gravity wave amplitudes, because of which the waves reach their breaking levels at lower altitudes and produce turbulence at lower altitudes than normal. Near continuous turbulent layers were found from 72 to 90 km altitude during this campaign.

Rocket-borne measurements were made from the equatorial latitudes at Alcantara (2.5°S, 44.4°W) in Brazil (*Goldberg et al.*, 1997; *Lehmacher et al.*, 1997) during the CADRE/MALTED campaign in August 1994. Turbulence was found between 85 and 90 km during the daytime flights. Also for the altitude range of 90 to 110 km, it was observed that the electron density fluctuations were dominated by the equatorial electrojet. Though the turbulence spectra above 90 km showed characteristic slopes of turbulence, the calculated energy dissipation rates were no longer compatible with the neutral turbulence. The presence of the equatorial electrojet during the daytime flights made it difficult to exclude the effect of electrodynamics even in the lower altitudes. It was concluded that it is difficult to decide whether the fluctuations below 90 km also were caused only due to neutral turbulence or by the electrojet or both (*Goldberg et al.*, 1997; *Lehmacher et al.*, 1997). However, the mathematical technique used for computing the power spectra in all these studies was Fourier transform or the Short Time Fourier transform, which required a sufficiently long length of data. The altitude resolution of the turbulence parameters thus estimated was of the order of 1 km and above.

Mesospheric turbulence was also studied using MST radars extensively. The morphological variations of the mesospheric backscattered echoes over Indian and other global stations may be summarized as follows (*Gage and Balsley*, 1980; *Kubo et al.*, 1997; *Kamala et al.*, 2003; *Kumar et al.*, 2007): (a) The radar backscattered signals from the mesosphere are generally intermittent with high spatial variability barring exceptions of Polar Mesosphere Summer Echoes (PMSEs) (b) There are at least 2 narrow height regions in the mesosphere like 72-77 km and 80-85 km which produce relatively strong radar backscatter on a more regular basis. The peak heights of the regions also vary with latitude and season. Over the high latitudes strong PMSEs are obtained from 82-85 km height range but during other seasons significant but weak backscatter echoes are generated from lower height regions (<80 km) also and (c) Over the low latitude stations e.g., Jicamarca (11.95°S, 76.87°W) and Gadanki(13.5°N, 79.2°E, 6.4°Dip), the main scattering layer lies around 75 ± 5 km with another weak region of radar scattering around 80 ± 5 km; the 75 ± 5 km scattering region showing seasonal dependence with the strongest echo seen during June/July months and the weakest during winter. *Sasi and Vijayan* (2001) and *Rao et al.* (2001) studied the seasonal variation of the energy dissipation rate and the eddy diffusion coefficient using the MST radar at Gadanki. These turbulence parameters showed a summer maximum and a winter minimum.

Royrvik and Smith (1984) investigated equatorial mesosphere using simultaneous measurements of the Jicamarca VHF radar and a rocket-borne LP during the CONDOR campaign of February-March 1983. The two sites were separated by about 60 km along N-S. Narrow layer of radar echoes was seen at 79 km (radar resolution of 3 km) 1 hour before the rocket launch but moved to range gates of 79 and 82 km at the time of rocket launch. The Langmuir probe detected irregularities in a narrow altitude region (85.2-86.6 km). It was inferred that the same scattering layer was observed by the two techniques. Simultaneous rocket-borne measurements of electron and ion densities and MST radar observations were also made from Poker Flat (65°N, 147.5°W) during the Middle Atmosphere Program (MAP) (*Goldberg et al.*, 1988; *Blood et al.*, 1988) to study the neutral turbulence.

A high-resolution study of mesospheric fine structure with the Jicamarca MST radar by *Sheth et al.* (2006) showed many interesting features. Spectral widths and backscattered power showed positive correlations at upper mesospheric heights in agreement with earlier findings (*Fukao et al.*, 1980) that upper mesospheric echoes are dominated by isotropic Bragg scatter. In many instances in the upper mesosphere, a weakening of positive correlation away from layer centers (towards top and bottom boundaries) was observed with the aid of improved height resolution.

This finding supports the idea that layer edges are dominated by anisotropic turbulence. *Sheth et al.* (2006) also observed isolated negative correlations at lower mesospheric heights below 70 km. These negative correlations were always associated with thin sheets in SNR maps. Instead of being composed of pure specular reflections, it is more likely that these thin sheets correspond to thin layers of anisotropic scatterers with orientations favorable for strong returns in one beam and weaker returns in others. The layers may even include a mix of isotropic and anisotropic scatterers, with the isotropic scatterers being visible from all viewing directions whereas the anisotropic ones being aspect sensitive.

Using the electron density irregularity data obtained from earlier sounding rocket flights from Sriharikota (14°N, 80°E), and 3 m irregularity data obtained by the MST radar at Gadanki (13.5°N, 79.2°E), which is located about 100 km west of Sriharikota, *Chakravarty et al.* (2004) have shown that the fine structures in the electron density irregularities are often present in the height region of $\sim$75 km over Sriharikota, which match quite well with the radar observed structures of the main scattering layer (70$\pm$5km) over Gadanki. The altitude resolution of the backscattered echoes of the radars is limited by the finite pulse width. With a 16 μs uncoded pulse a resolution of 2.4 km was obtained (*Kumar et al.*, 2007), but the use of smaller pulse widths can give better altitude resolutions. Observations using narrow pulse lengths indicated presence of scattering layers down to $\sim$ 600 m embedded in broad a turbulence field of 4-5 km thickness at 75 $\pm$ 5 km. *Sheth et al.* (2006) obtained a resolution of 150 m using pulses of 1 μs baud length. Using ion density measurements over high latitudes *Blix et al.* (1990) also had showed earlier that the turbulence tends to occur in thin layers ($\Delta z < 1$ km). *Strelnikov et al.* (2003) showed, from *in-situ* neutral density measurements, that thin turbulent layers as small as 100 m are possible in the mesosphere. *Strelnikov et al.* (2003) used a new technique of continuous wavelet transform to obtain the power spectra of neutral density fluctuations. Recent advances in mathematical tools has seen the growth of this mathematical microscope and is described in detail in Chapter 2 of this thesis. Today, the continuous wavelet transform (CWT) has become a more powerful tool to understand the geophysical phenomena in both the frequency and the time (here altitude) domains, simultaneously. This technique has improved the altitude resolution of the turbulence parameters tremendously and has been used since many years for the study of turbulence produced in wind tunnels, near heated walls, in numerical simulations, etc., (*Farge* (1992, and references therein)). It is also used in various other geophysical studies including long term mesospheric airglow variations (*Das and Sinha*, 2008), neutral density measurements in the mesosphere and lower thermosphere (MLT) (*Strelnikov et al.*, 2003; *Rapp et al.*, 2004), diurnal tide winds in the MLT region (*Xue et al.*, 2007), etc. In the present study the wavelet technique will be applied to electron density measurements over Sriharikota to study the fine structure of turbulent layers in the mesosphere. Fourier analysis is not done here as the fact that the results from both techniques are same is clearly established (*Perrier et al.*, 1995; *Torrence and Compo*, 1998; *Strelnikov et al.*, 2003).

Modelling studies also have been performed to understand the dynamics of the mesosphere. *Garcia and Solomon* (1985) used a two dimensional dynamical and chemical model to investigate this aspect in the mesosphere and the lower thermosphere, which includes a gravity wave parameterization. The seasonal variation of the eddy diffusion coefficient was studied using this model and was found to be high during solstices and low during the equinoxes. Other modelling studies include Direct Numerical Simulation (DNS) studies of turbulence arising due to Kelvin-Helmholtz shear instability and gravity-wave breaking, believed to be the two major sources of turbulence generation near the mesopause show some very interesting features (*Fritts et al.*, 2003). Sharp gradients in turbulence quantities at edge regions are present due to very efficient mixing within the turbulent region. Such gradients have not been computed earlier due to the limitation of the analysis techniques of rocket data. Any such sharp gradients would be smeared out in such cases. It is also observed in the simulations that turbulence occurs in layers of stratification and very thin layers of stratification also can be formed.

The present study of mesospheric neutral turbulence aims at understanding the fine structure of the turbulence over low and equatorial latitudes using electron density measurements. The wavelet transform will be applied and the turbulence parameters will be estimated with a better altitude resolution. The results will be discussed and compared with past rocket-borne and radar results. Some of the issues predicted by the numerical simulation techniques like the thin layers of turbulence, gradients in turbulence parameters etc., (*Fritts et al.*, 2003) will be addressed in the present thesis. Some interesting aspects like anisotropic turbulence, possible effects of geomagnetic storm on low latitude mesospheric turbulence, effect of equatorial electrojet instabilities on mesospheric turbulence, *etc.*, will also be discussed.

1.3 Mesospheric Airglow Emissions

Another important issue related to the energetics of the mesosphere and lower thermosphere is the airglow emissions. The atomic oxygen green line nightglow emission OI ($^1D_2$-$^1S_0$) in the mesosphere was the first to be observed among all emissions in the atmosphere. It is one of the most studied emissions till date and is the other topic that is dealt in the present thesis. In 1866, Angstrom discovered it while doing auroral spectroscopy. Two years later in 1868, he found that it was present even in the absence of aurora and concluded that it was a component of nightglow. Later in 1920s, Rayleigh studied variation in brightness of the green 'auroral' line at 557.7 nm and concluded that the terrestrial component of light of the night sky was qualitatively different from aurora. He was the first to express the brightness of airglow in absolute units – the number of atomic transitions per second in a column along the line of sight. Accordingly, the photometric unit used in airglow and auroral observations has been named after him. The green line was identified as the forbidden transition OI($^1D_2$-$^1S_0$) by McLennan and others in the late 1920s while investigating its Zeeman pattern. Later Frerichs confirmed it in 1930 and also predicted the energy of $^1D_2$ and $^1S_0$ on the basis of ultraviolet spectrum of oxygen.

The presently accepted characteristic of the OI 557.7 nm green line profile is an emission that increases rapidly from 90 km to a peak around 97 km and then tails off rather slowly to disappear around 120 km. *McDade* (1998) examined the excitation process of various airglow emissions and summarized the dependence of their volume emission rates. According to *McDade* (1998), the OI 557.7 nm green line emission varies as $[O]^3$ in the lower region below the peak of the emission layer and as $[O]^2[M]$ in the higher region above the peak.

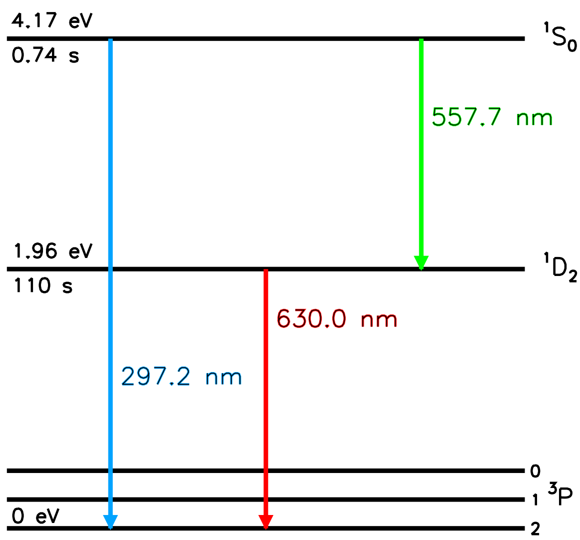

Figure 1.3: *Schematic of the energy levels and the various emissions in atomic oxygen.*

The electronic configuration of a neutral oxygen atom is $1s^2\ 2s^2\ 2p^4$. The four valence electrons being equivalent electrons rule out certain energy levels in the atom and so the first and second excited states are $^1D_2$ and $^1S_0$ at 1.96 and 4.17 eV respectively (Fig. 1.3). The green line emission comes mostly from the mesosphere with a peak at 97 km and the red line emission peaks near the F region peak at 250 km approximately. The lower energy level of green line, $^1D_2$ is the upper energy level of the red line. So one anticipates that the red line emission should be observed at mesospheric altitudes also, which is not the case. The lifetime of the $^1D_2$ level is 110 s and at mesospheric altitudes, where the neutral densities are high, this is sufficient time during which the oxygen atom can lose energy via collisions.

At higher altitudes this quenching does not take place, as the number density of neutral molecules is very less.

1.3.1 Emission Mechanism

For many years it was thought that in the mesosphere and the lower thermosphere, O(^{1}S) was excited directly in the three-body process (1.24) referred to as the Chapman reaction.

$$O(^3P) + O(^3P) + O(^3P) \rightarrow O_2 + O(^1S) \tag{1.24}$$

However, following the laboratory experiments of *Barth and Hildebrandt* (1961), *Barth* (1964) proposed a two-step mechanism represented by the following reactions:

$$O(^3P) + O(^3P) + M \rightarrow O_2^* + M \tag{1.25}$$

$$O_2^* + O(^3P) \rightarrow O_2 + O(^1S) \tag{1.26}$$

where the third body M is O_2 or N_2 or O itself and O_2^* is an excited state of O_2 formed directly in the three body recombination reaction 1.25; βk_1 is the rate of this reaction, ($k_1 = 4.7 \times 10^{-33} \times (300/T)^2$ cm^{6}s^{-1}molec^{-2}; *Campbell and Gray* (1973)) and δk_4^O is the rate of the reaction 1.26, and β and δ are the efficiency of production of O_2^* and O(^{1}S) in the above reactions respectively. The notation of *McDade et al.* (1986) is followed for the rate of reactions, *etc*. Considerable effort has been expended later on, in both laboratory and rocket experiments, to determine which of these two mechanisms dominates in the terrestrial nightglow. It is now well established (*Bates*, 1992) that OI 557.7 nm is emitted by two-stage Barth mechanism, however identification of the proposed O_2^* intermediate state is yet to be established. Possible precursors are the A, A', c and $^5\Pi_g$ states of O_2. However *Bates* (1992) concluded that $O_2(c)$ must be the precursor. But recent studies by *Slanger et al.* (2004), show that $O_2(A)$ state is no less a possibility. Laboratory measurements (*Slanger et al.*, 2004) suggest that the Herzberg states of molecular oxygen are collisionally coupled to a considerable degree, making the identification of the O_2^* species that produces the green line a very uncertain exercise.

McDade et al. (1986) showed good agreement between observed and calculated OI 557.7 nm emission profiles assuming the energy transfer mechanism and proposed quenching parameters for this green line emission. The sequence of reactions involved is as follows:

$$O_2^* + O_2, N_2, O \rightarrow all \;\; products \tag{1.27}$$

$$O(^1S) + O_2, N_2, O \rightarrow quenched \;\; products \tag{1.28}$$

$$O_2^* \rightarrow O_2 + h\nu \tag{1.29}$$

$$O(^1S) \rightarrow O(^1D) + h\nu(557.7nm) \tag{1.30}$$

$$O(^1S) \rightarrow O(^3P) + h\nu \tag{1.31}$$

where $k_4^{O_2,N_2,O}$ are the rate coefficients for quenching of O_2^* in reaction 1.27 and $k_5^{O_2}$ ($4.9 \times 10^{-12} \times (-885/T)$ cm^{3}s^{-1}molec^{-1}), $k_5^{N_2}$ ($\leqslant 5.0 \times 10^{-17}$ cm^{3}s^{-1}molec^{-1}) and k_5^{O} ($\leqslant 2.0 \times 10^{-14}$ cm^{3}s^{-1}molec^{-1}) are the rate coefficients for quenching of O (^{1}S) in reaction 1.28 by O_2, N_2, O respectively (*McDade et al.*, 1986; *Melo et al.*, 1996, and references therein); A_4, A_5 ($= 1.183$ s^{-1}), A_6 ($= 1.35$ s^{-1}) are the Einstein's coefficients of spontaneous emission in reactions 1.29, 1.30 and 1.31, respectively. The reaction rates, production efficiencies and Einstein's Coefficients involving O_2^* are not known as O_2^* is itself unidentified. O(^{1}D) produced in reaction 1.30 can also undergo radiative transition to the ground state O(^{3}P) emitting a photon at λ = 630.0 nm.

$$O(^1D) \rightarrow O(^3P) + h\nu(630.0nm) \tag{1.32}$$

But as already mentioned earlier the lifetime of the O(^{1}D) state is 110 sec, which is very large, and hence before it undergoes radiative transition it loses its energy via collisions. At MLT heights the densities are high enough for collisional removal of O(^{1}D). Therefore the red line is not observed at these heights.

1.3.2 Effect of Dynamics

The lifetime of atomic oxygen is very long above 100 km, so that it may be transported before recombination (Eq. 1.25). And the lifetimes of the excited species, $O(^1S)$ and O_2^* are of the order of seconds and so the transport of excited species is not significant. Hence airglow perturbations arise due to the transport of O by winds and also due to density perturbations caused by tides, gravity waves and other disturbances.

As the atomic oxygen layer descends into an altitude of larger densities (of M), the emission rate increases through reactions 1.25 and 1.26. However, at still lower altitudes the losses begin to dominate over the production rate and recombination also becomes rapid. This exhausts the supply of atomic oxygen and hence decreases the airglow emission.

The bulk of the 557.7 nm emission comes from the mesosphere and the contributions from the thermosphere is location-dependent and is significant for equatorial and equatorial anomaly regions but not for mid latitudes (*Shepherd et al.*, 1997). For equatorial regions the thermospheric contribution can exceed the mesospheric component during post mid-night periods of high solar activity, especially in the post-midnight hours (*Rajesh et al.*, 2007).

1.3.3 The Long Term and the Short Term Variations

Both long and short term variations of the green line emission, starting from quasi-biennial oscillations to diurnal variations, have been reported in the literature (*Brenton and Silverman*, 1970; *Fukuyama*, 1976, 1977; *Cogger et al.*, 1981; *Shepherd et al.*, 1995; *Yee et al.*, 1997; *Shepherd et al.*, 2005; *Deutsch and Hernandez*, 2003; *Reid and Woithe*, 2007). *Fukuyama* (1976) examined the diurnal and semi-diurnal variation of 557.7 emission along with Na and OH airglow emissions for a number of stations lying between latitudes of Davao ($7°05'N$) and Rapid City ($44°02'N$) and found a strong semi-diurnal variation over mid latitudes and attributed it to the semi-diurnal tide. WINDII observations, which showed a profound local time dependence over the equator, were also attributed to strong tidal dynamics (*Shepherd et al.*, 1995). Model results by *Ward* (1999) reinforce the role of tidal dynamics in the diurnal variation. The latitudinal variation of the diurnal variation study of *Brenton and Silverman* (1970) shows that (a) for latitudes between 19°N and 34°S, the minimum occurs during the night, (b) for latitudes between 22°N and 44°N, the maximum occurs during the night and (c) for latitudes higher that 44°N, there is very little variation throughout the night.

Fukuyama (1977) examined the same data of *Fukuyama* (1976) for seasonal and other long term variations using the Maximum Entropy Method. The amplitude of the annual component was in the range of 10% to 30%, with smaller amplitudes at low latitudes. The amplitude of the semi-annual oscillation also showed a latitudinal variation, with a decrease with increasing latitude from 37% at low latitudes to about 10% at mid latitudes. For mid latitudes, the seasonal variation of 557.7 nm showed maxima during summer and fall, in addition to a much smaller peak during winter/early spring. *Deutsch and Hernandez* (2003) studied the long term behavior and climatology of the green line using nightly averaged data of geomagnetically quiet times from (a) nine stations having long term observations covering both northern and southern hemispheres and (b) short term observations from 20 other stations. The longest data series available was that of Kiso (35.79°N, 137.63°E), Japan from 1979-1990. Periodogram analysis of Kiso data by *Deutsch and Hernandez* (2003) showed statistically significant annual and semi-annual components, with the annual component beginning as a not so significant component but at the end of 12 years, it appeared as the most significant feature of the spectrum (Fig. 1.4). *Deutsch and Hernandez* (2003) concluded that the amplitude of the annual component increases with increasing latitude and that of the semi-annual component decreases with increasing latitude. The variation of the annual component was attributed to the yearly revolution of the earth and the variation of semi-annual component was attributed to the semi-annual oscillation in the diurnal tide (*Fukuyama*, 1977). Using the same ground based photometric data of 557.7

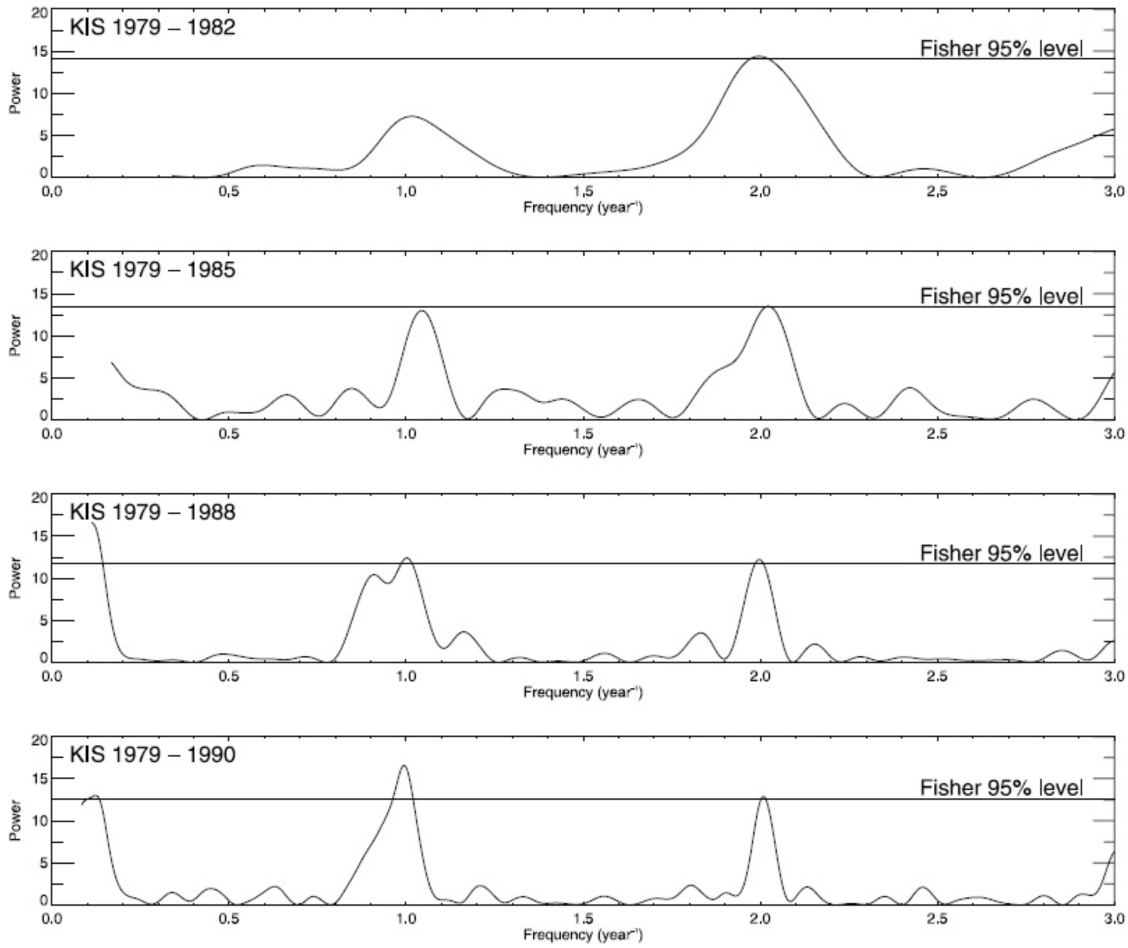

Figure 1.4: *Periodogram analysis of Kiso data, for increasing lengths of time. The figure is reproduced from Deutsch and Hernandez (2003).*

nm over Kiso, including nightly averages from 1991-1994 thus making the data series 16 years long, *Shiokawa and Kiyama* (2000) showed the presence of two seasonal peaks, one in June and other in October. However, these two peaks do not correspond to the semi-annual peaks during equinoxes observed by the model but can be seen, though not very clearly, in the satellite data (*Shepherd et al.*, 2005). *Reid and Woithe* (2007) studied the long term variations of the green line at a geographically conjugate station, Buckland Park (34.9°S, 138.6°E) near Adelaide, Australia. They analyzed 11 year long data set during the epoch 1995 to 2006. Significant annual and semi-annual oscillations were observed with amplitudes between 17($\pm$5)%

and 14($\pm$5)% of the mean intensity, respectively. The annual oscillation was observed to peak in summer while the semi-annual oscillation showed maxima near equinoxes. A solar cycle dependence was also found in the data similar to what was seen by *Deutsch and Hernandez* (2003).

Using OGO satellite data *Donahue et al.* (1973) observed a strong semi-annual component over mid latitudes in the green line emission with the largest mean emission rates in April and October. *Cogger et al.* (1981) also observed a strong semi-annual component over mid latitudes (35°N) with maxima during April and October from the ISIS-2 satellite data of 1971 and 1972. The semi-annual variation in the 557.7 nm emission in the tropical region was observed in the WINDII satellite measurements, ground based photometer measurements and also in the TIME-GCM model (*Shepherd et al.*, 2005). However, for the mid latitude regions, a semi-annual component was seen by *Shepherd et al.* (2005) in the satellite data only at 96 km at 2000 hrs LT, which weakened as the night progressed and was almost absent by 0200 hrs LT (Fig. 1.5). This aspect of the semi-annual component has not been detected so far, in the ground based photometric measurements averaged over local time for any of the mid latitude stations.

In addition to the annual and the semi-annual variation in the 557.7 nm emission, *Fukuyama* (1977) reported the presence of a strong quasi-biennial component as well. The amplitude of this component exhibited clear cut latitudinal variation with a value of 20-30 % in the tropical region. It decreases drastically at 35°N, being only about 10% north of that latitude. However, the OH and Na nightglow emissions showed a quasi-triennial oscillation instead of the quasi-biennial oscillation. The quasi-biennial component in the 557.7 nm airglow emission has been explained in terms of the stratospheric quasi-biennial oscillation (QBO), where zonal winds in the tropical stratosphere change direction every 28-29 months, due to the interaction between upward propagating gravity, equatorial and planetary waves and the mean flow. During the easterlies the intensities of all three emissions showed increased intensities and during the westerlies, decreased intensities. Prolonged easterly phases in the lower altitudes could have produced the

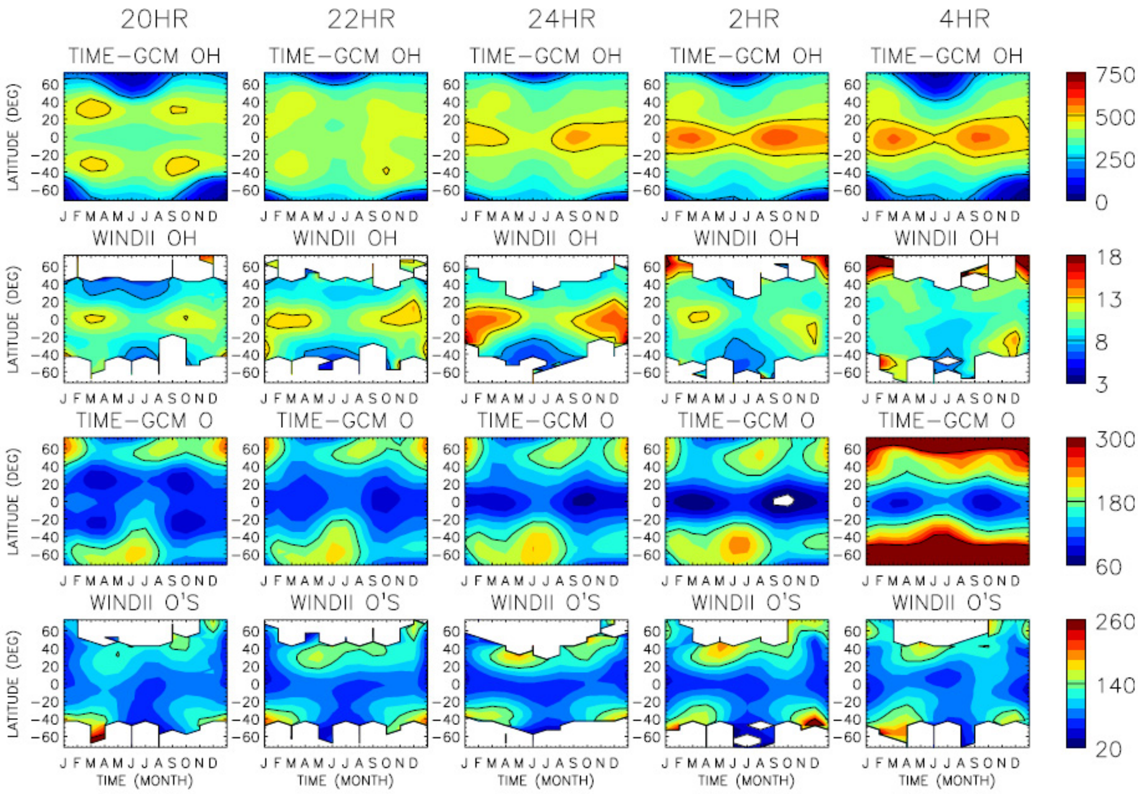

Figure 1.5: *The seasonal variation of OH and green line emissions observed by WINDII and also the TIME-GCM predictions. The figure is reproduced from Shepherd et al. (2005).*

quasi-triennial oscillations that were observed in the OH and the Na nightglow (*Fukuyama*, 1977). The QBO which is produced in the stratosphere propagates up to mesosphere and alter dynamics and the atomic oxygen concentration and hence the 557.7 nm emission. At the mesospheric and lower thermospheric altitudes, the QBO can influence upto mid latitudes also. *Reid and Woithe* (2007) also observed a quasi-biennial oscillation over Buckland Park, Australia, with a smaller amplitude of about $5(\pm1)\%$ of the mean intensity. It is important to note that the periodogram analysis by *Deutsch and Hernandez* (2003) using ground based photometric observations at Kiso did not detect the quasi-biennial component (Fig. 1.4). However, over tropical and equatorial latitudes WINDII measurements show a distinct semi-annual variation and an apparent modulation by the stratospheric quasi-biennial oscillation (*Shepherd et al.*, 2006).

The airglow emissions and the green line emission in particular are an important feature of the mesosphere and the lower thermosphere which can be used as a proxy to the dynamics in that region. *Garcia and Solomon* (1985), used a two dimensional dynamical/chemical model to study the mesosphere and the lower thermosphere which consisted of parameterization of gravity wave drag and diffusion to study the influence of gravity wave breaking in the 60-110 km region. The model was used to calculate the green line emission intensities to study the influence of breaking gravity waves on the seasonal and latitudinal variations of this emission. These model results were compared with the satellite observations of *Cogger et al.* (1981). Over mid-latitudes the satellite observations showed a strong semi-annual oscillation, which was attributed to the semi- annual variation of the vertical eddy diffusivity. Model results of *Garcia and Solomon* (1985) showed that during the solstices, the vertical eddy diffusivity was high, and hence the oxygen rich air in the lower thermosphere could be transported to lower altitudes where it could be lost by recombination. During equinoxes, the vertical diffusivity was low and the oxygen rich air cannot be transported to lower altitudes which will result in more oxygen densities near 100 km and hence higher green line emission intensities. A climatological study of the vertical eddy diffusivity at mid-latitudes during 1986-1992 using the MU radar at Shigaraki (35°N, 136°E), which is very close to Kiso also shows a similar variation (*Kurosaki et al.*, 1996; *Fukao et al.*, 1994). A semi-annual variation with solstice maxima and a weaker annual oscillation with summer maximum were observed. In addition, a quasi-biennial oscillation was also observed in the upper mesosphere during this period.

In the present study of mesospheric airglow emissions the Continuous Wavelet Transform is applied to the long term (16 years) data set of oxygen green line nightglow intensities observed over Kiso, Japan, during 1979-1994. The new mathematical tool with a time-frequency localization has enabled a better understanding of epochs during which semi-annual, annual and quasi-biennial oscillations are present in the observed data set.

CHAPTER 2

Instrumentation, Data and Analysis

2.1 Instrumentation - Langmuir Probe

In the mesosphere, the ion-neutral and electron-neutral collision frequencies are much higher than ion and electron gyro-frequencies, respectively and hence any perturbations produced in neutral density by any source such as turbulence will also be transmitted to ions and electrons as well (*Thrane and Grandal*, 1981). This aspect is utilized in rocket-borne electron and ion density measurements as well as in the MST radar technique to study turbulence and to derive neutral turbulence parameters in this region. In the present study Langmuir probes have been employed to measure the electron density fluctuations and thereby study the neutral turbulence in the equatorial and low latitude mesosphere and the lower thermosphere.

The Langmuir probe technique was employed for ionospheric studies for the first time in 1946 by Spencer and his colleagues in the USA. A modified version of the basic technique was developed at Physical Research Laboratory, Ahmedabad (Prakash and Subbaraya, 1967) and was flown on board different types of rockets from the Thumba Equatorial Rocket Launching Station (TERLS), Thumba (8.5°N, 76.9°E) and Satish Dhawan Space Centre (SDSC), Sriharikota (14°N, 80°E).

2.1.1 Theory of Langmuir Probe

The Langmuir probe experiment consists of exposing a metallic sensor to the medium under study and measuring the current collected as a function of the bias voltage applied to it, which is varied from a convenient negative value, through zero to a positive value. The resulting current - voltage (I-V) curve, shown in Fig. 2.1, called the probe characteristics is used to determine various plasma parameters such as ion density, electron density, electron temperatures, etc. A Langmuir

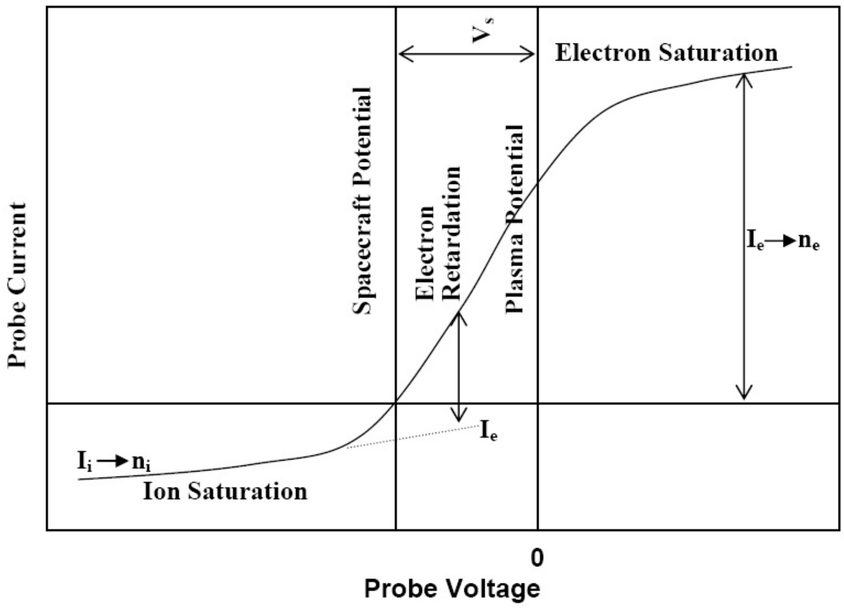

Figure 2.1: *Current voltage (I-V) characteristics of Langmuir probe.*

probe system consists of a probing electrode, generally referred to as the 'sensor' and an electrically insulated reference electrode which in most cases is the rocket body (for rocket borne experiments). A guard electrode is used to give a definite geometry to the electric field of the sensor and reduce the leakage current from the sensor to the reference electrode thereby improving the performance of the probe.

The current collected by the sensor from the surrounding plasma is converted into a voltage suitable for telemetry by an amplifier and telemetered to the ground. With appropriate biasing of the LP with a fixed positive voltage, the collected current is used to determine fluctuations of electron density at different scales, which typically range between a few km to about a meter.

Probe at Plasma Potential

When a probe is at the same potential as the ambient plasma, it receives both electrons and positive ions that strike its surface during their random motion in the medium. The net current drawn by the probe is therefore,

$$J = J_e + J_i \tag{2.1}$$

where J_e is the random electron current reaching its surface and J_i is the random positive ion current.

$$J_e = Aj_e = \frac{A.n_e e v_e}{4} \tag{2.2}$$

where, j_e is the random electron current per unit area, A is the effective surface area of the probe, n_e is the ambient electron number density, e is the electron charge and v_e is the electron thermal velocity

$$v_e = \sqrt{\frac{8kT_e}{\pi m_e}} = 6.21 \times 10^5 \sqrt{T_e} \tag{2.3}$$

and m_e is the electron mass, T_e is the electron temperature, k is the Boltzmann constant

Similarly,

$$J_i = Aj_i = \frac{A.n_i e v_i}{4} \tag{2.4}$$

where, v_i is the ion thermal velocity

$$v_i = \sqrt{\frac{8kT_i}{\pi M_i}} \tag{2.5}$$

M_i is the ion mass and T_i is the ion temperature.

And since $M_i \gg m_e$, it results in $v_i \ll v_e$ and hence $j_i \ll j_e$. So the net current to the probe at plasma potential can be considered to be purely the electron current.

$$J \cong A.j_e = A.\frac{n_e e v_e}{4} = A.n_e.e.\left\{\frac{kT_E}{2\pi m_e}\right\}^{\frac{1}{2}} \tag{2.6}$$

This property can be used to determine the electron density in the medium if the electron temperature is known and vice versa.

The Plasma Sheath and Floating Potential

As the typical thermal velocity of electrons in the E-region of the ionosphere is about 200 km/s and that of ions is 1 km/s, a metallic probe immersed in plasma is very soon surrounded by an excess electron cloud as $v_e \gg v_i$. The accumulation of the electrons around the probe continues until the electron cloud presents to the surrounding medium a negative potential strong enough to retard the electrons and make the electron flux to the outer surface of this electron cloud equal to the random positive ion flux in the medium and there by maintaining equilibrium. The intermediate medium separating the probe from the ambient plasma is called the plasma sheath. The thickness of plasma sheath varies with the probe potential, but its scale is usually expressed in terms of a plasma parameter known as Debye shielding length, λ_D, which is given by

$$\lambda_D = \sqrt{\frac{kT_e}{4\pi n_e e^2}} \tag{2.7}$$

Typical value of Debye shielding length in the E-region ranges between a few cm to a few tens of cm. The probe thus acquires a negative potential due to the plasma sheath, *vis-à-vis* the space or plasma potential, and is called the floating or wall potential. And at the floating potential, the net current to the probe is zero. The floating potential V_f given by

$$V_f = -\frac{kTe}{e}\ ln\frac{J_e}{J_i} \tag{2.8}$$

where, T_e is the electron temperature, e is electronic charge, $J_e(J_i)$ is the electron (positive ion) random current density. Although the exact floating potential is a function of electron temperature, electron and ion mean velocities, around 100 km altitude its typical value is about $-0.5V$ relative to the plasma or space potential.

Probe at a Negative Potential

When the probe is at a large negative potential with respect to the plasma potential, it attracts positive ions and electrons are repelled and the total current collected by the probe is a net positive ion current. This is called the ion saturation region (Fig. 2.1). As the probe potential becomes less negative the ion current starts reducing and electron current starts increasing, due to energetic electrons that can overcome the negative potential of the probe. Thus for measurement of ion densities, the probe must be operated in the ion saturation region.

Retarding Potential Analysis

As the probe potential is decreased further, the electron current to the probe increases rapidly (Fig. 2.1). This is called the 'retarding potential regime' in which the positive ion current is very small in magnitude compared to the electron current and the electron current consists of those electrons which could overcome the negative (retarding) potential in the probe. For a Maxwellian distribution of electrons, the electron current, J_V, at a retarding potential V is given by

$$J_V = J_e \exp\left\{\frac{eV}{kT_e}\right\} \tag{2.9}$$

$$\log J_V = \log J_e + \frac{eV}{kT_e} \tag{2.10}$$

Thus, if measurements of probe current are made at a number of retarding potentials, a semilog plot of the probe current versus probe potential will be a straight line of slope e/kT_e. This property is used to determine the electron temperature of the medium.

Probe at a Positive Potential

Even a small positive potential is sufficient to make the positive ion current negligible when compared to the electron component and the net current can be considered to be purely an electron current. The electron current to a positive probe depends in a complex manner both on size and shape of the probe. For a sufficiently small probe, whose dimensions are comparable to the Debye length and mean free path of the medium, Langmuir and Mott Smith (1926) have obtained the following expressions for spherical, planar and cylindrical geometries.

i. *A small sphere*: For a sphere of radius smaller than Debye length, the current is given by,

$$J = J_e \left\{ 1 + \frac{eV}{kT_e} \right\} \tag{2.11}$$

ii. *A large plane*: For a large plane whose thickness is comparable to the sheath thickness, the current is given by

$$J = J_e \tag{2.12}$$

iii. *A long thin cylinder*: For a long cylinder whose radius is comparable to the Debye length, the current is given by

$$J = J_e \left\{ \frac{2}{\sqrt{\pi}} \frac{eV}{kT_e} + \exp \frac{eV}{kT_e} P \left(\frac{eV}{kT_e}^{\frac{1}{2}} \right) \right\} \tag{2.13}$$

where P is the error function

$$P(x) = \frac{2}{\sqrt{\pi}} \int_0^x e^{-y^2} dy \tag{2.14}$$

2.1.2 Proportionality between Probe Current & Electron Density

Assuming that there are no large variations of electron temperature in regions of measurement, the probe current can be considered to be proportional to the electron density. Thus a conversion factor can be used to get the electron density from the probe current. The factor can be evaluated by comparison with the electron density obtained by ionosonde (*Smith*, 1969) or some other experiments which can give electron density. If the Langmuir probe is flown along with a radio frequency resonance probe, the conversion factor can be evaluated by comparison with the densities obtained by these measurements, as the resonance probe gives absolute value of electron density. Based on the experimental observations, it is widely accepted that the proportionality factor remains fairly constant above 85 km up to approximately 180 km. In the region below 85 km also a constant factor is used to estimate the electron density, as no independent measurement of electron density was available. However, due to the above considerations, the measurements in this region are used to study the fluctuations of electron density and not the absolute electron densities. In the present study the conversion factor was obtained by normalizing the probe current at the E-region peak with the electron density obtained by an ionosonde located in the neighbourhood of rocket station. The conversion factor used in the present work is 2.4×10^4 cm$^{-3}\mu$ A^{-1}.

2.1.3 Limitations of LP onboard Rockets

Effects of Negative Ions

In the classical Langmuir theory, described in section 2.1.1, the system consists only of positive ions and electrons. In the ionosphere this assumption is true only above about 70 km as negative ions are also present below this altitude. Hence the current collected by the Langmuir probe below this altitude consists of electron as well as negative ion current. Hence in the strict sense the LP theory is applicable only for altitudes greater than 70 km.

The Reference Potential

The positive and negative potentials on the LP sensor, referred to in the LP theory, are with respect to the plasma or space potential. As it is not possible to realize plasma potential, the next best thing is to realize the floating potential, which as mentioned in Sec. 2.1.1, is approximately $0.5V$ lower than the plasma potential in the E-region. As the rocket body also comes to the floating potential it is used as a reference potential to ensure that the LP sensor is biased well above the plasma potential. For working in the electron saturation regime, a voltage of $+4V$ is usually applied to the LP sensor with respect to the rocket body.

Size of Sensor

The current collected by a probe in space returns to the ionosphere through the surface of the vehicle, so that the impedance of this surface with respect to the plasma is actually an element in the probe circuit. The collected current therefore should not significantly change the reference potential. This implies that the ratio of the area of the rocket body to the area of the sensor should be greater than the ratio of the electron and ion saturation currents (J_e/J_i) that can be collected by the vehicle. In the ionosphere, this ratio of the electron and ion saturation currents is of the order of 150 to 200. For an RH-300 MK II rocket (height = 100 cm (after combustion), diameter = 30 cm) used in the present experiment (Ref: Sec. 2.1.4), the surface area of the rocket body is approximately 9000 cm^2. The diameter of the hemispherical sensor used is 4 cm, which results in the above ratio to be greater than 350. This ensures that the current collected by the probe does not disturb the rocket payload.

Effects of Rocket Velocity

Most probe theories are developed for a probe at rest but by its very nature, a rocket borne probe does not meet this criterion. However typical rocket velocities of the order of a kilometer per second to a few hundred meters per second are much smaller than electron thermal velocities in the ionosphere which are of the order of 100 km s^{-1}. Hence the probe can be considered to be at rest with respect to the electrons.

Wake Effects

When a rocket or a satellite is travelling with a velocity greater than the mean ion velocity in the medium, positive ions can not penetrate into the rear of the vehicle although electrons can. Hence the absence of the positive ions creates a negative potential in the wake of the vehicle. This potential affects the charge particle collection by the probe and therefore should be avoided. The best solution is to place the probe at the nose tip of the rocket or far into the medium using booms. However, a probe at the nose tip does enter the wake during descent of the rocket. Errors arising due to the wake effects have thus to be considered during descent.

Effects of Geomagnetic Field and Attitude Variations

The attitude of the rocket borne sensor changes during the rocket flight due to rocket spin, precession as well as changes in the inclination of the rocket axis during its trajectory. In the presence of the Earth's magnetic field this variation in attitude has an effect on the probe current collected since charged particles can travel more easily along the magnetic lines than across it due to much higher electrical conductivity along the field lines. The effective mean free path for a charged particle is the Larmor radius, $\rho = mv_{\perp}/eB$, where m is the mass of the charged particle , B is the magnetic flux density and $v_{\perp}$ is the velocity of the particle in a direction perpendicular to the magnetic field. In the lower ionosphere the Larmor radius for an electron is of the order of one cm and for an ion it is of the order of a meter. Therefore, any probe of practical dimensions will be larger than the mean free path of the electrons. Since motion along the field lines is uninhibited, the probe collects electrons from distant regions along the field lines and since motion across is inhibited, the probe collects electrons not far away across the field lines. The effect of rocket spin and precision can thus clearly be seen as a modulation in the electron probe current. The extent to which this perturbation occurs depends on various factors like shape of the sensor, position of the sensor with respect to

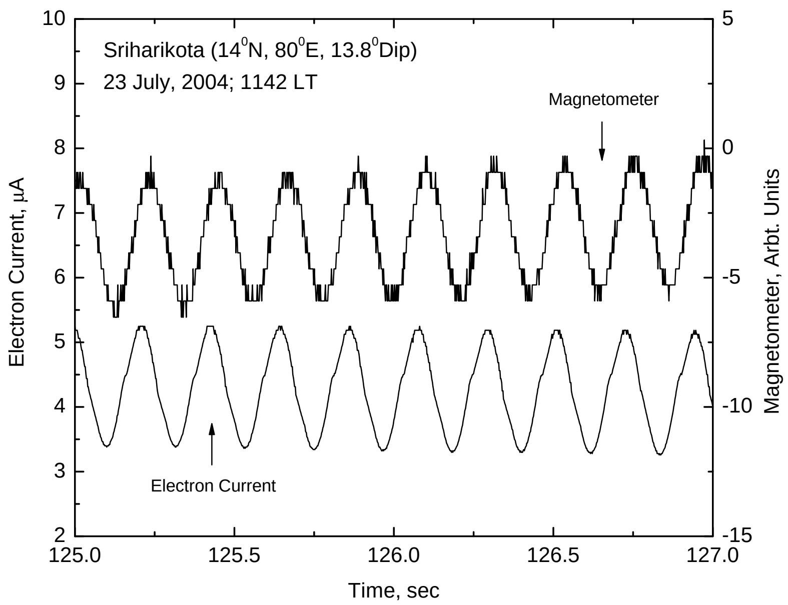

Figure 2.2: *Two second data of Langmuir probe current from main channel in comparison to magnetometer data.*

the rocket spin axis, asymmetries on the body of the rocket, since it is used as the reference electrode, as well as the potential at which the sensor is being operated.

Very large spin modulation was observed in Flights 1 and 2 (Sec. 2.1.4) when the Langmuir probe was placed away from the rocket spin axis. Fig: 2.2 shows two second data of July 2004 flight along with the magnetometer data. The effect of rocket spin on the electron current is clearly observed.

2.1.4 Langmuir Probe Flights

Three RH-300 MK II rockets, each carrying a Langmuir probe, were launched during daytime to study the equatorial and low latitude mesosphere and lower thermosphere. Two of these flights were launched from Sriharikota (14°N, 80°E, 13.8°Dip) on 23 July 2004 at 1142 hrs LT (UT+05:30 hrs) and on 08 April 2005 at 1125 hrs LT (hereafter called Flight 1 and Flight 2, respectively) and the third flight was

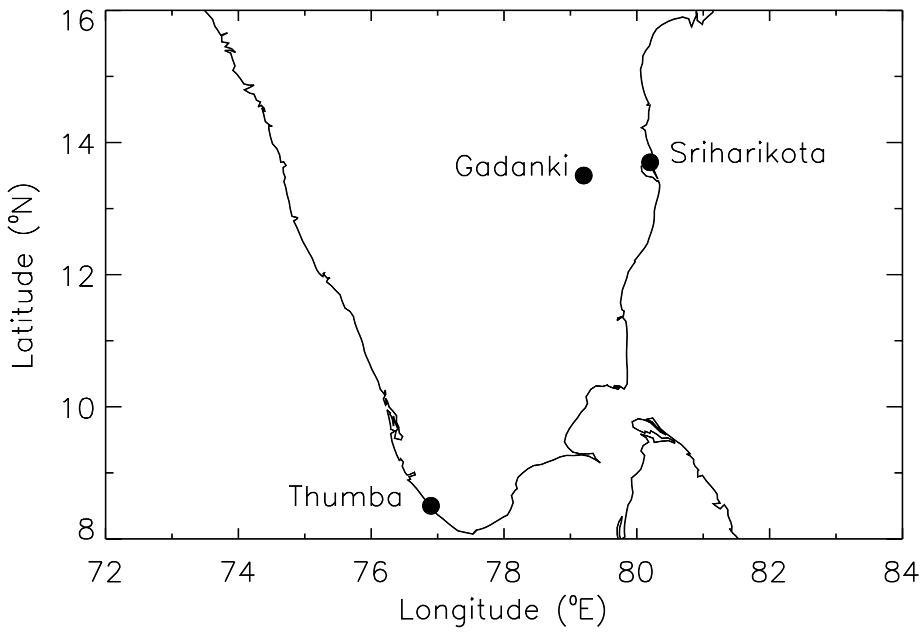

Figure 2.3: *The geographic locations of the launch sites and MST radar.*

launched from Thumba (8.5°N, 76.9°E, 0.4°Dip) on 27 November 2005 at 1123 hrs LT (hereafter called Flight 3). The first two flights were conducted in coordination with the Indian MST radar at National Atmospheric Research Laboratory (NARL), Gadanki (13.5°N, 79.2°E, 6.4°Dip). Both these flights were launched when the MST radar observed strong echoes at mesospheric altitudes. A pre-campaign was conducted to understand the morphology of the mesospheric echoes over Gadanki using the MST radar during May to July 2003 *(Harish Chandra, Personal Communication)*. For Flight 1 the month of July was chosen as the occurrence and the strength of echoes were found to be highest during June-July and for Flight 2 the month of April was chosen to study the relatively weaker echoes and understand the seasonal variation. *Kamala et al.* (2003) discussed this seasonal variation of the mesospheric echoes over Gadanki in detail. Fig. 2.3 gives the geographic location of the two rocket launching sites, Sriharikota and Thumba, and the location of the Indian MST radar at Gadanki.

Fixed bias Langmuir probes were used to measure electron density fluctuations in all the three flights. The configurations explained below were almost similar in all three flights. For the Flights 1 and 2, the LP sensor was a split sphere of 50 mm diameter, whose upper hemisphere was biased at +4 V and was used to collect the electron current, and the lower hemisphere was used as a guard electrode. For Flight 3, the LP sensor was of ogive shape and was biased at +4 V. For Flights 1 and 2, the LP sensor was mounted on the top deck with the help of a 200 mm long boom while for Flight 3 the sensor was mounted of the rocket rocket nose tip. The electrical connection to the signal conditioning electronics was provided by means of a coaxial cable. The electronics was accommodated in a package mounted on one of the instrument decks. To cover the large dynamical range arising from the change in current due to variation in the electron density an automatic gain amplifier was used to measure the current in the range of 1 nA to about 3μA. For studying the electron density fluctuations in different scale sizes the current collected by the LP sensor was processed on board in three channels with different gains having frequency response of 0-100 Hz, 30-150 Hz and 70-1000 Hz. These channels are named as LP Main, LP MF and LP HF and were sampled at 520 Hz, 1040 Hz and 5200 Hz, respectively.

2.1.5 Other Complementary Experiments

RH-200 Rockets with Chaff Payloads

The first RH-200 rocket with chaff payload was launched at 1215 hrs LT on 23 July 2004, *i.e.,* 33 minutes after the launch of Flight 1 and the second one was launched at 1158 hrs LT on 08 April 2005, *i.e.,* 33 minutes after the launch of Flight 2 to measure the neutral winds in the atmosphere. The metallic chaffs were tracked by radars, which provided zonal and meridional wind profiles in the height ranges of 20-76 km and 20-60 km, respectively.

Table 2.1: *Specifications of the MST Radar Operating Parameters*

Parameter	Specifications
Location	Gadanki (13.5°N, 79.2°E)
Frequency	53 MHz
Peak Power Aperture Product	3×10^{10} Wm^2
Peak Power	2.5 MW
Maximum Duty Ratio	2.5%
Number of Yagi Antennas	1024
Beam Width (3 dB full width)	3°
Beam Angle	zenith and 10° off zenith
Number of Beams used	East, West, Zenith, North, South
Pulse Width	3 μs uncoded (450 m)
Inter Pulse Period	0.9 ms
Maximum number of range bins	125
Number of Coherent integrations	40
Maximum number of FFT points	256

Indian MST Radar

The MST radar of the National Atmospheric Research Laboratory (NARL) is located at Gadanki and operates at 53 MHz (*Rao et al.*, 1995). On 23 July 2004 and 08 April 2005 the MST radar was operated during 0830-1600 LT. Details of the experimental parameters used for the radar operation are presented in Table 2.1. Uncoded 3 μs pulses were used to provide a height resolution of 450 m during the rocket launch period. Five radar beam directions (North-10°, South-10°, East-10°, West-10° and Zenith) were used to get the return echoes from 60 km to 120 km. The angles refer to zenith angles used for the experiments.

2.2 Data

2.2.1 Langmuir Probe Data

The current collected by the Langmuir probe sensors in all the flights was processed on board through three separate channels, to accurately detect the large range of amplitudes associated with scale sizes ranging from a few kilometers down to less than a meter. The main channel had a frequency response of DC-100 Hz and was sampled at 520 Hz. The rocket vertical velocity in the lower altitudes at ∼70 km was ∼850 m/s and hence the altitude resolution of electron density measurements was ∼2 m. The smallest scale that could be studied using the main channel data was therefore ∼4 m. At ∼90 km, the velocity was ∼600 m/s and the altitude resolution was higher and ∼1 m. The smallest scale that could be studied was ∼2 m.

The other two channels were AC channels of medium and high frequencies with frequency responses of 30-150 Hz and 70-1000 Hz and were sampled at 1040 and 5200 Hz, respectively. Using the data from these channels, the smallest scale sizes that could be studied were smaller by a factor two and ten, respectively. After combining the data from the three channels, information regarding various scale sizes ranging from a kilometer to less than a meter was obtained.

2.2.2 Photometer Data

One of the longest series of ground based photometric observations of the oxygen green line (OI 557.7 nm), from 1979 to 1994 at Kiso (35.8°N, 137.6°E), Japan was used in the present study for detecting the long term variations. Ground based measurements of integrated zenith intensities of the OI 557.7 nm emission taken at one minute interval for twelve years (1979-1990) and hourly averages for four years (1991-1994) were taken from the World Data Center (WDC) C2 for Airglow, Tokyo, Japan. One-minute values were not available at the WDC for the period 1991-1994. These measurements were made on moon-less clear nights.

2.3 Analysis

2.3.1 Basic Mathematics and Fourier Transform

Let $L^p(\Re)$ denote the collection of all measurable functions f defined on $\Re$ such that the integral, called the Lebesgue integral,

$$\int_{-\infty}^{\infty} |f(t)|^p \, dt \tag{2.15}$$

is finite for each p, where $1 \leq p < \infty$.

Let $x(t)$ be an integrable function (*i.e.*, $x(t) \in L^1(\Re)$). The Fourier transform of such a function is given by,

$$\hat{x}(\omega) = \frac{1}{\sqrt{2\pi}} \int_{-\infty}^{\infty} x(t) e^{-i\omega t} dt \tag{2.16}$$

If a particular frequency exists in the given signal, the above integral will result in a large value at ω and if it does not exist then the integral will give a minimum value or zero, thus producing a frequency spectrum. $\hat{x}(\omega)$ satisfies the following:

i. $\hat{x} \in L^\infty(\Re)$ with $||\hat{x}||_\infty \leq ||\hat{x}||_1$,

   where $||x||_p$ is the norm of the function x and is defined as

$$\|x\|_p = \begin{cases} \left\{ \int_{-\infty}^{\infty} |x(t)|^p \, dt \right\}^{\frac{1}{p}} & \text{for} \quad 1 \leq p < \infty \\ \text{ess sup } |x(t)| \, ; \, (\infty < t < \infty) & \text{for} \quad p = \infty \end{cases} \tag{2.17}$$

ii. $\hat{x}$ is uniformly continuous on $\Re$,

iii. if the derivative x' of x also exists and is in $L^1(\Re)$, then $\hat{x}'(\omega) = i\omega\hat{x}(\omega)$, and

iv. $\hat{x}(\omega) \to 0$, as $\omega \to \pm\infty$

Inspite of the last property of $\hat{x}$, for every $x \in L^1(\Re)$, it is not necessary that $\hat{x}$ is also in $L^1(\Re)$. Only when $\hat{x} \in L^1(\Re)$ can the signal $x(t)$ be recovered back by the use of the Inverse Fourier Transform (IFT), which is defined as,

$$x(t) = \frac{1}{\sqrt{2\pi}} \int_{-\infty}^{\infty} \hat{x}(\omega) e^{i\omega t} d\omega \tag{2.18}$$

The Fourier transform is capable of finding the different frequencies present in the signal, but it does not show the time information. However, time information is not completely lost but is hidden in the phases. If it were lost, it would not be possible to reconstruct the signal by IFT (Eq. 2.18). Noise like features are also observed in the Fourier spectrum of non-stationary signals (signals that do not contain a set of frequencies at all times) that arise due to abrupt changes in the frequencies. Such noise is not observed in case of stationary signals (signals that contain a set of frequencies at all times). Hence Fourier transform best suits stationary signals and can also be used for non stationary signals when time information is not required.

To overcome the difficulty faced by the Fourier transform, the Short Time Fourier Transform (STFT), also called as the Window Fourier Transform (WFT), was developed. In this technique, the given signal is split up into number of segments in small intervals of time where it is assumed that in each interval the signal remains stationary. A non trivial function $g(t) \in L^2(\Re)$ can be used as a window function if it satisfies the condition,

$$t.g(t) \in L^2(\Re) \tag{2.19}$$

The center t^* and radius Δ_g of a window function $g(t)$ are defined as

$$t^* = \frac{1}{\|g\|_2^2} \int_{-\infty}^{\infty} t \left| g(t) \right|^2 dt \tag{2.20}$$

and

$$\Delta_g = \frac{1}{\|g\|_2^2} \left\{ \int_{-\infty}^{\infty} (t - t^*) \left| g(t) \right|^2 dt \right\}^{1/2}, \tag{2.21}$$

respectively; and the width of the window fucntion $g(t)$ is defined by $2\Delta_g$.

Such a window function, $g(t)$, whose width is equal to the width of the segment in the signal is taken. It is first placed at the beginning of the signal and then

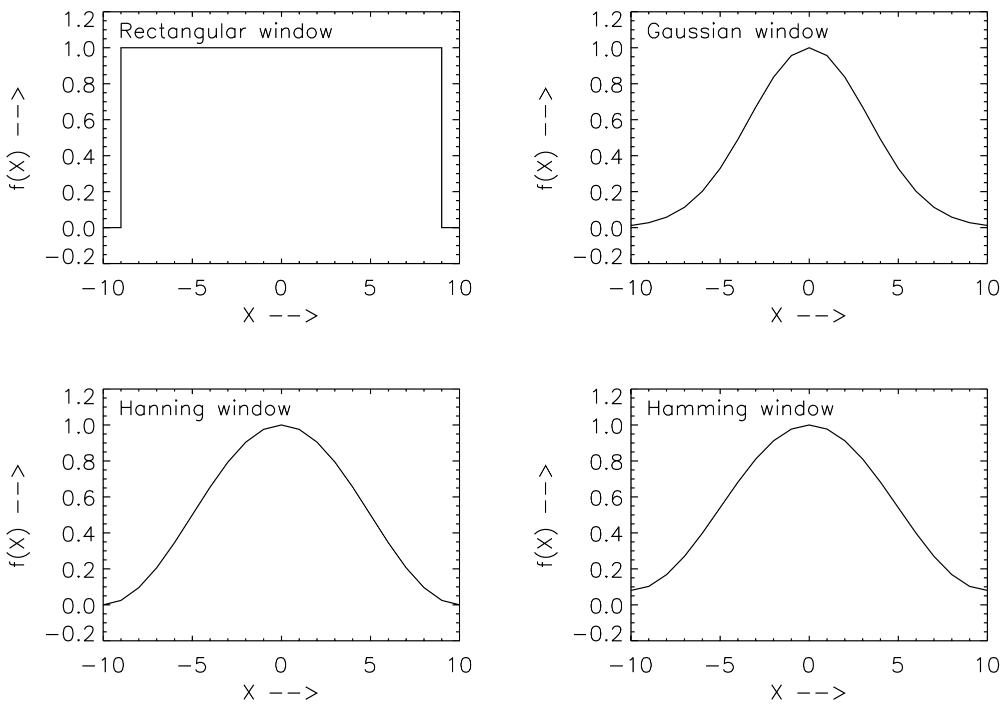

Figure 2.4: *A few examples of window functions.*

multiplied with the signal with an appropriate weightage of the window. This is taken as the new signal and the Fourier transform is used to find frequency spectrum for that part of the signal. The window is then translated along the signal and the process is repeated. Few examples of window functions are the Rectangular window, Gaussian window, Hamming window, Hanning Window, etc., (Fig. 2.4). By using a rectangular window function, the data is broken into parts and the data is not modified at all. The problem of leakage appears due to this as the phase at the beginning of the signal and the end of the signal might not be same. This causes a broadening of the frequency components that are picked up by the FT or the STFT. By using other window functions like the Hanning or the Hamming windows, which start at zero at $t = 0$, increase smoothly to 1 at $t = T/2$ and then decrease smoothly again to zero at $T = 0$, the leakage problem can be reduced. The Hanning window, $H(t)$ is generated from a cosine function and for

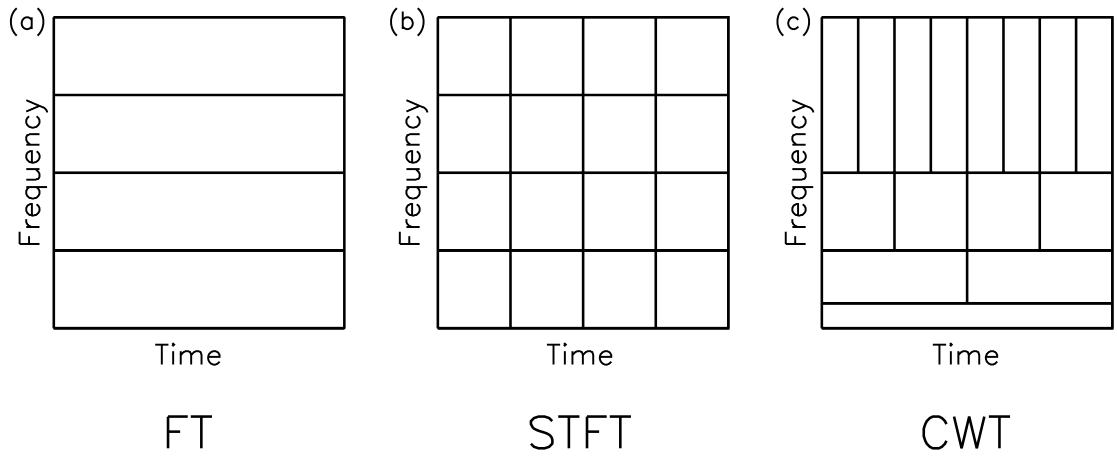

Figure 2.5: *The time frequency plane for (a) Fourier Transform (FT), (b) Short Time Fourier Transform (STFT) and (c) Continuous Wavelet Transform (CWT).*

$0 \leq t \leq T, H(t)$ is given as

$$H(t) = \frac{1}{2}\left[1 - cos\left(\frac{2\pi t}{T}\right)\right] \tag{2.22}$$

The STFT of a function $x(t)$ is given by,

$$STFT(\omega, t') = \int_t [x(t) * g(t - t')] * e^{-i\omega t} dt \tag{2.23}$$

The transformed signal is a function of two parameters, frequency and time. Thus information of various frequencies in the signal at different times can be obtained. The efficiency of this method depends to some extent upon the assumption that the signal segment is stationary. This method has a constant resolution in the time domain as well as in the frequency domain. This can be represented in the time frequency plane as a box whose width gives the time resolution and the height gives the frequency resolution (Fig. 2.5). If the signal w non-stationary in one of the segments considered, then the time information corresponding to that time interval would be lost. To have a higher resolution in time, the width of the window function can be further shortened and hence the length of the signal to be Fourier analyzed. But as the signal becomes shorter, the frequency resolution becomes coarser because any number of frequencies can be expected in such a short signal. Thus, a narrow window will give a good time resolution but a poor frequency resolution while a wide window will give a poor time resolution but a good frequency resolution. In the time frequency plane, good frequency (time) resolution means long rectangles with the longer side along the time (frequency) axis. This also means a low time (frequency) resolution. There is thus, a trade off between the frequency resolution and the time resolution. This is the disadvantage of this technique. Hence STFT is not suitable for signals with both very high and very low frequencies. In addition, several window lengths must be employed to determine the appropriate choice. For a definite window, the time and frequency resolutions will be the same throughout, *i.e.,* the boxes in the time frequency plane are of constant width and height. The resolution in both domains is limited by the the Heisenberg's uncertainty principle to $1/4\pi$. This results in a finite area of the box in the time frequency plane (Fig. 2.5), *i.e.,* it cannot be said that a particular frequency existed at a point of time. Rather, it can be said that a particular band of frequencies existed in an interval of time. A Gaussian window gives the best possible resolution in time and frequency simultaneously, with the smallest time frequency window, with an area of $1/4\pi$.

2.3.2 Continuous Wavelet Transform

The wavelet transform, relative to some basic wavelet (defined below), provides a flexible time frequency window which automatically narrows when observing high frequency components and widens when observing low frequency components. The technique of using wavelets to identify localized power events in time series is now being used and applied in various studies starting from stock market fluctuations to geophysical phenomena.

If the function $\psi \in L^2(\Re)$ satisfies the "admissibility" condition:

$$C_\psi := \int_{-\infty}^{\infty} \frac{\left|\hat{\psi}(\omega)\right|^2}{|\omega|} d\omega < \infty \tag{2.24}$$

then ψ is called a wavelet. The window function ψ is called a *mother wavelet*. If, in addition, both ψ and $\hat{\psi}$ satisfy Eq. 2.19, then the basic wavelet provides a time frequency window with finite area given by $4\Delta_{\psi} \cdot \Delta_{\hat{\psi}}$. Under this condition it follows that $\hat{\psi}$ is a continuous function, so that the finiteness of C_{ψ} in Eq. 2.24 implies $\hat{\psi} = 0$, or equivalently,

$$\int_{-\infty}^{\infty} \psi(t)dt = 0 \tag{2.25}$$

A Gaussian window does not possess this property and hence cannot be used as a wavelet. In addition, the wavelet should also be well localized in physical and Fourier spaces. To study the M^{th} derivative of a function $x(t)$, the wavelet should have cancellations upto order M, so that it does not react to lower-order variations of $x(t)$. Hence for all $m \leq M$,

$$\int_{-\infty}^{\infty} \psi(t)t^m dt = 0 \tag{2.26}$$

In other words, to be admissible as a wavelet, a function must have zero mean and be localized in both time and frequency space (*Farge*, 1992). This is the reason why ψ is called a "wavelet".

Relative to every basic wavelet ψ, the continuous wavelet transform (CWT), $W_x^{\psi}(s,\tau)$, of a function $x(t) \in L^2(\Re)$ is defined as,

$$W_x^{\psi}(s,\tau) = \frac{1}{\sqrt{|s|}} \int_t x(t) * \psi^*(\frac{t-\tau}{s})dt \tag{2.27}$$

The transformed signal, $W_x^{\psi}(s,\tau)$, is a function of two variables, τ and s, *i.e.,* translation and scale. These two parameters correspond to time and frequency respectively. $\psi(\frac{t-\tau}{s})$ is called the mother wavelet and $\psi^*(\frac{t-\tau}{s})$ is its conjugate. It is so called because all the wavelets to be used in the analysis are derived from this function. The factor $\frac{1}{\sqrt{|s|}}$ is for energy normalisation.

Assume that both ψ and $\hat{\psi}$ are window functions satisfying Eq. 2.19. The center and radius of the function $\psi(s,\tau)$ are given by $\tau + st^*$ and $s\Delta_{\psi}$, respectively and those of its Fourier transform, $\hat{\psi}(s\omega)$, are given by ω^*/s and Δ_{ψ}/s, respectively.

So the wavelet transform $W_x^{\psi}(s,\tau)$ gives local information of an analog signal $f(t)$ with a time frequency window,

$$[\tau + st^* - s\Delta_\psi, \tau + st^* - s\Delta_\psi, \frac{\omega^*}{s} - \frac{\Delta_\psi}{s}, \frac{\omega^*}{s} + \frac{\Delta_\psi}{s}] \tag{2.28}$$

For small values of s, this window is thin and tall and for large values it is wider and short (Fig. 2.5). Scale is inversely proportional to frequency, *i.e.,* high scale implies low frequency and *vice versa*. For a particular s, a different wavelet is derived from the mother wavelet. When scaling is done, the mother wavelet is dilated, *i.e.,* it is either stretched or compressed. Larger scales corresponding to lower frequencies are stretched versions of the mother wavelet and smaller scales corresponding to high frequencies are compressed versions of the mother wavelet. As the transform is computed for every single frequency or scale, the width of the window changes and hence the resolution, as is evident from the Eq. 2.28. Hence, different resolutions are obtained at different frequencies. At lower frequencies there is a good resolution in frequency and poor resolution in time, and at high frequencies it is vice versa. Here also Uncertainty Principle comes into the picture and so the boxes always have some finite area. As the wavelet is translated through the signal, the frequency spectrum at different times is obtained. The process is same as shifting of the window function through the signal in STFT. For every value of s and τ, one point in the time frequency plane is computed.

Some basic properties of the continuous wavelet transform are as follows.

Linearity: The wavelet transform is linear because it is an inner product between the signal $x(t)$ and the wavelet ψ. Let $x(t) = x_1(t) + x_2(t)$, then

$$W_x^{\psi}(s,\tau) = W_{x_1}^{\psi}(s,\tau) + W_{x_2}^{\psi}(s,\tau) \tag{2.29}$$

Let $x(t) = kx_3(t)$, then

$$W_x^{\psi}(s,\tau) = k \cdot W_{x_3}^{\psi}(s,\tau) \tag{2.30}$$

Covariance by Translation: The continuous wavelet transform is covariant under any translation t_0. Let $x_0(t) = x(t - t_0)$, then

$$W_{x_0}^{\psi}(s,\tau) = W_x^{\psi}(s,\tau - t_0) \tag{2.31}$$

Covariance by Dilation: The continuous wavelet transform is covariant under dilation also. Let $x_a(t) = x(at)$, then

$$W^{\psi}_{x_a}(s,\tau) = \frac{1}{\sqrt{a}} W^{\psi}_{x}(as, a\tau) \tag{2.32}$$

Continuous Wavelet Transform of Discrete Data

For a discrete equally spaced time series x_n, where $n = 0, 1, \ldots, N-1$ is the index in time, the convolution of x_n with a scaled and translated version of ψ gives the continuous wavelet transform (*Torrence and Compo*, 1998):

$$W_n(s) = \sum_{n'=0}^{N-1} x_{n'} \psi^* \left[\frac{(n'-n)\delta t}{s} \right] \tag{2.33}$$

where the (*) indicates the complex conjugate and no subscript indicates that the wavelet function is normalized (Eq: 2.38). By varying the wavelet scale s and translating along the localized time index n, the wavelet coefficients can be computed. Although it is possible to calculate the wavelet transform using Eq. 2.33, it can be done considerably faster in the Fourier space. Using Eq. 2.33, the convolution should be done N times for each scale. Whereas in the Fourier space the Convolution theorem allows us to do all N convolutions simultaneously using a discrete Fourier transform. According to the theorem, the wavelet transform will be the inverse Fourier transform of the product of the Fourier transforms of the signal ($\hat{x}_k$), and the conjugate of the mother wavelet.

$$W_n(s) = \sum_{k=0}^{N-1} \hat{x}_k \hat{\psi}^*(s\omega_k) e^{i\omega_k n\delta t} \tag{2.34}$$

where the Fourier transform of the signal is given by,

$$\hat{x}_k = \frac{1}{N} \sum_{n=0}^{N-1} x_n e^{-2\pi i k n/N} \tag{2.35}$$

In the continuous limit, the Fourier transform of the function $\psi(t/s)$ is given by $\hat{\psi}^*(s\omega_k)$. The angular frequency ω_k is defined as,

$$\omega_k = \begin{cases} \frac{2\pi k}{N\delta t} & : \; k \leq \frac{N}{2} \\ -\frac{2\pi k}{N\delta t} & : \; k > \frac{N}{2} \end{cases} \tag{2.36}$$

The wavelet function at each scale s is normalized to have unit energy such that the wavelet transforms are directly comparable to each other and to transforms of other series.

$$\int_{-\infty}^{\infty} \left|\hat{\psi}_0(\omega')\right|^2 d\omega' = 1 \tag{2.37}$$

$$\hat{\psi}(s\omega_k) = \left(\frac{2\pi s}{\delta t}\right)^{1/2} \hat{\psi}_0(s\omega_k) \tag{2.38}$$

Using these normalisations, one has at each scale s

$$\sum_{k=0}^{N-1} \left|\hat{\psi}(s\omega_k)\right|^2 = N, \tag{2.39}$$

where N is the number of points.

The wavelet transform $W_n(s)$ is real $(R\{W_n(s)\})$ or complex $(R\{W_n(s)\}) + (I\{W_n(s)\})$ depending on whether the wavelet function $\psi(\eta)$ is real or complex, respectively. The wavelet power spectrum can thus be defined as $|W_n(s)^2|$. The analysis in the present thesis is done by the latter method to determine the wavelet power spectra (*Torrence and Compo*, 1998) [1].

Wavelet Functions

A few examples of wavelet functions are the Morlet wave, Paul and Mexican Hat. In the present study a Morlet wave has been used, which consists of a plane wave modulated by Gaussian (Fig. 2.6).

$$\psi_0(\eta) = \pi^{-1/4} e^{i\omega_0\eta} e^{-\eta^2/2} \tag{2.40}$$

where η is a dimensionless time parameter and ω_0 is the frequency, here taken to be 6 to satisfy the admissibility condition.

For nonorthogonal wavelet analysis, one can use an arbitrary set of scales to build up a more complete picture. It is convenient to write the scales as fractional powers of two and so the set of scales to compute the wavelet transform in Eq. 2.33 are chosen as follows:

$$s_j = s_0 2^{j\delta j}, j = 0, 1, ..., J \tag{2.41}$$

[1]Software is available at URL: http://paos.colorado.edu/research/wavelets/

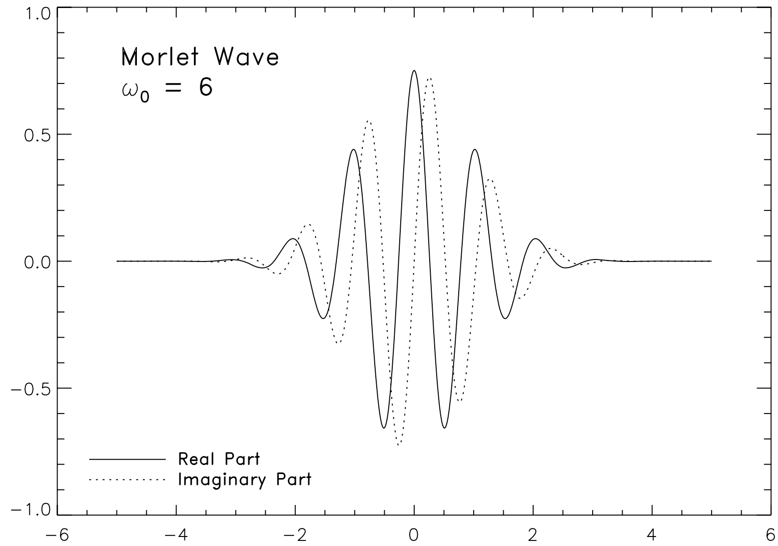

Figure 2.6: *The Morlet wavelet of frequency, $\omega_0 = 6$.*

$$J = \delta j^{-1} \log_2 (N\delta t/s_0) \tag{2.42}$$

where s_0 is the smallest resolvable scale and J determines the largest scale. s_0 is chosen such that the equivalent Fourier period is approximately $2\delta t$. The choice of a sufficiently small δj depends on the width in spectral space of the wavelet function. For the Morlet wavelet, a δj of about 0.5 is the largest value that still gives adequate sampling in scale, while for the other wavelet functions, a larger value can be used. Smaller values of δj give finer resolution.

Cone of Influence

Since the data set is finite, errors are introduced into the spectrum at the beginning and end of the spectrum. This happens because the Fourier transform assumes the data to be cyclic. When this condition is not satisfied the data set is padded with zeroes to make the data length N equal to the next highest power of two to speed up the Fourier transform. Errors due to such padding are called edge errors and the *Cone of Influence* (COI) is the region where these errors are important. It is defined as the e-folding time for the autocorrelation of wavelet power at each scale. For a Morlet wavelet, the *e*-folding time, τ_s is,

$$\tau_s = \sqrt{2}s \tag{2.43}$$

Note that it is independent of the frequency of the wavelet (ω_0). The mexican hat wavelet has a much narrower COI. τ_s is large at larger scales (smaller frequencies) and forms the vertex of the cone and at smaller scales (larger frequencies), τ_s is small and forms the base of the cone. The size of the COI at each scale also gives a measure of the decorrelation time for a single spike in the time series. By comparing the width of a peak in the wavelet power spectrum with this decorrelation time, one can distinguish between a spike in the data (possibly due to random noise) and a harmonic component at the equivalent Fourier frequency.

Wavelet scale and Fourier frequency

The relationship between the equivalent Fourier period and the wavelet scale can be derived analytically for a particular wavelet function by substituting a cosine wave of a known frequency into Eq. 2.34 and computing the scale s at which the wavelet power spectrum reaches its maximum. The wavelet scale (s) and the Fourier period (T, inverse of the Fourier frequency) for a Morlet wave with $\omega_0 = 6$, are related as $T = 1.03\ s$. They are almost equal. But this need not be the case for all wavelet functions (*Torrence and Compo*, 1998).

Time-averaged Power Spectrum

Slicing of the wavelet plot gives the local power spectrum and a time-averaged wavelet spectrum over a certain period is

$$W_n^2(s) = \frac{1}{n_a} \sum_{n=n_1}^{n_2} |W_n(s)|^2 \tag{2.44}$$

where the new index n is arbitrarily assigned to the midpoint of n_1 and n_2, and $n_a = n_2 - n_1 + 1$ is the number of points averaged over. The extreme case is when the average is over all the local wavelet spectra, which gives the *global wavelet spectrum* (Eq. 2.45).

$$W^2(s) = \frac{1}{N}\sum_{n=0}^{N-1}|W_n(s)|^2 \tag{2.45}$$

The global wavelet spectrum provides an unbiased and consistent estimation of the true power spectrum of a time series (*Torrence and Compo*, 1998). Further the global wavelet spectrum can be used as a background against which the peaks in the local wavelet spectrum can be identified.

Confidence levels

An appropriate background spectrum is chosen to determine the significance levels of the wavelet power spectrum. For many geophysical phenomena, an appropriate background spectrum is either white noise (with a flat Fourier spectrum) or red noise (increasing power with decreasing frequency) against which the actual wavelet power spectrum is compared. If a peak in the wavelet power spectrum is above this background, then it can be assumed to be a true feature with a certain percentage of confidence. And to determine for e.g., the 95% confidence level (significant at 5%), the background spectrum is multiplied by the 95^{th} percentile value for χ_2^2, where χ_ν^2 is the chi-square distribution with ν degrees of freedom (*Torrence and Compo*, 1998, and references therein).

2.3.3 Analysis of Langmuir Probe Data

The current collected by the Langmuir Probe sensor was processed on board three channels, *viz.,* the Main, MF and HF channels . The current obtained in the LP main channel was converted to electron density using a conversion factor of 2.4×10^4 cm^{-3}. μ A^{-1}, as explained earlier in Sec. 2.1.2. The factor was obtained by normalizing the probe current at the E-region peak during the July 2004 flight with the electron density obtained by the ionosonde located at Sriharikota at 1142 hrs LT, on 23 July 2004, *i.e.,* at the time of the July 2004 rocket flight.

The Wavelet Spectra

The continuous wavelet transform using the Morlet wavelet (Ref. Section 2.3.2) was used to find the power spectra in all the three channels. The smallest scale, s_0, taken was $2\delta t$. The δt was different for the three channels and was 0.00192, 0.00096 and 0.000192 sec for the Main, MF and the HF channels, respectively. It is the inverse of their sampling frequency. The δj was taken to be 0.125, to give sufficient scale resolution. The confidence levels were not determined in this study as the interest was in the shape of the power spectrum but not in the peaks of the spectrum.

The complete profile of the electron density was taken to compute the spectra of the Main channel. Time-averaged power spectra corresponding to an altitude region of 100 m were computed using Eq: 2.45. These spectra will be referred to as the altitude-averaged power spectra hereafter. The altitude-averaged power spectra calculated from the MF and the HF channel data in the same altitude regions were then normalized to the main channel altitude-averaged power spectra to obtain the final composite altitude-averaged power spectra ranging from DC to 1000 Hz, for every 100 m. A range of 100 m was chosen to make sure that the breakpoints observed in the spectra, are indeed present in the data set. Secondly, averaging the spectra over 100 m assures that consecutive spectra contain independent information on the relevant spatial scales between 10 and 100 m. Finally, the other reason for this choice is to ensure numerical stability of the fitting algorithm (*Strelnikov et al.*, 2003). The percentage amplitudes were also calculated from all the spectra using the Eq. 1.23.

Heisenberg Model and Turbulence Parameters

All altitude-averaged power spectra were examined to find if the Heisenberg theoretical spectral model (Sec. 1.2.2) could be fitted. If the observed power spectrum contained the two characteristic slopes of $-5/3$ and -7, of the ISR and the VDR, respectively, then the model was fitted by varying the parameter $k_0 = 2/l_0$. The best fit identifies the break in the slope and hence the inner scale, l_0. For those spectra where the inner scale was identified unambiguously, other turbulence parameters were estimated as discussed in Sec. 1.2.3. The temperature values required for the calculations were taken from MSISE-90 model (*Hedin*, 1991) and the kinematic viscosity and Brunt-Väisala frequency were also calculated using the temperatures and densities from the same model.

2.3.4 Analysis of Photometer Data

The hourly averages of integrated emission of the oxygen green line emission over Kiso were computed for the period 1979–1990 and concatenated with the hourly averages of 1991–1994. Monthly averages at each hour of the night from 1800 hrs Japan Standard Time (JST; UT+09:00 hrs) to 0500 hrs JST were then calculated to form twelve time series of 16 years each. In addition, a nightly averaged series was also computed by taking averages of emissions at each hour from 2000 hrs to 0300 hrs JST. In view of very few data points around 1800, 1900, 0400 and 0500 hrs JST, these were not used in the present analysis.

The continuous wavelet transform (Ref. Section 2.3.2) was applied to the eight data series of monthly averages at each hour of the night from 2000 to 0300 hrs JST, as well as to the nightly average for each month. The software written in IDL, provided by *Torrence and Compo* (1998), was used for the present analysis also. The Morlet wavelet was used as the mother wavelet. Since the code requires equally spaced data, about 20 points were interpolated in each of the series from 2000 to 0300 hrs JST, each of which is a series of 192 points. The least square quadratic fit was used for the interpolation. A number of other interpolation techniques were also tried but the results were very similar. The 90% and 95% confidence levels were also computed using a white noise fourier spectrum to determine the statistically significant oscillations, which are the semi-annual, annual and the quasi-biennial oscillations, and also their period of occurrence. The percentage amplitudes of these components were computed using the 12-point, 24-point and 56-point running averages of the data, respectively.

CHAPTER 3

Results from Mesospheric Turbulence Study

This chapter presents the results on mesospheric turbulence obtained (a) from the rocket borne electron density measurements from the three flights launched on 23 July 2004, 08 April 2005 and 27 November 2005 flight, which will hence forth be referred to as Flight 1, Flight 2 and Flight 3, respectively and (b) from other complementary rocket, radar and ground based experiments. The flight details and the solar and geophysical parameters on the days of flight are given in Table 3.1.

The trajectories of all the three rockets are given in Fig. 3.1. All three flights, *viz.,* Flights 1 to 3, were conducted at almost the same hour of the day around 1130 hrs LT and reached an apogee of 109, 116 and 109 km, respectively. However, due to differences in rocket elevation angles, the horizontal ranges travelled by the rockets differed significantly and were 95, 150 and 125 km, respectively. The rocket spin rates were 4.6, 6.15 and 8.5 s^{-1}, respectively. Vertical velocities of all the three rockets during ascent are given in Fig. 3.2. Flight 2 had a slightly higher velocity, which resulted in a slightly higher apogee of 116 km.

Table 3.1: *Details of rocket flights and solar and geophysical data*

Flight Details	Flight 1	Flight 2	Flight 3
Vehicle used	RH-300 MkII	RH-300 MkII	RH-300 MkII
Launch Site	Sriharikota*	Sriharikota*	Thumba†
Date	July 23, 2004	April 8, 2005	November 27, 2005
Time (LT)	1142	1125	1123
Apogee (km)	109	116	109
Horizontal Range‡ (km)	96	150	125
Spin Frequency (s^{-1})	4.6	6.15	8.5
Ap Index	52	3	3
Σ Kp Index	38	6	5+
F 10.7 cm Solar flux	170.4	87.9	77.9

*Satish Dhawan Space Center (SDSC), Sriharikota (14°N, 80°0E)

†Thumba Equatorial Rocket Launching Station (TERLS), Thumba (8.5°N, 76.9°E)

‡ Based on extrapolated values.

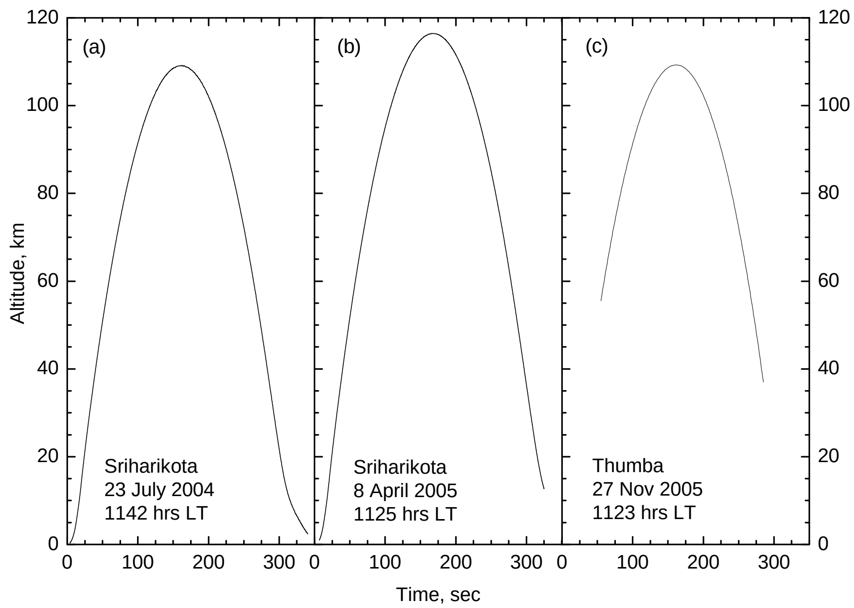

Figure 3.1: *Trajectories of the RH 300 MK II rockets during the three flights launched from (a) Sriharikota on 23 July 2004, (b) Sriharikota on 08 April 2005 and (c) Thumba on 27 November 2005.*

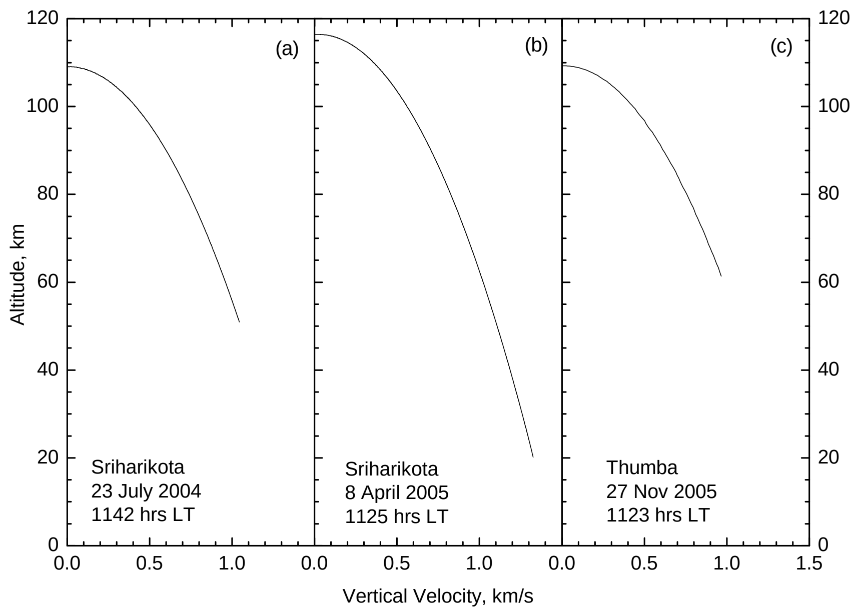

Figure 3.2: *Vertical velocity of the RH 300 MK II rockets during ascent of the three flights.*

3.1 Electron Density and Gradients

Fig. 3.3 shows the electron density (n_e) profiles during ascent and descent of the rocket for Flights 1 and 3 and only during ascent for Flight 2. As there was a telemetry failure beyond 85 km in case of Flight 2, only ascent data up to 85 km could be obtained. Electron density profiles obtained from all the three fights were largely similar in shape and number densities. Electron densities during the descent were lower than the ascent values above 88 km altitude for Flight 1 and during the entire vertical extent for Flight 3. This could be due to the presence of horizontal gradients of electron density. Also the sensor could be in the wake during descent and hence there could be errors in the measurement of the electron densities. Due to this, results pertaining only to ascent data will be discussed hereafter.

The electron densities built up very fast at the base of the ionosphere during all three flights. As shown in Fig. 3.3a, during Flight 1, the electron density changed by nearly two orders of magnitude from 20 to 1000 cm^{-3} in a vertical extent of

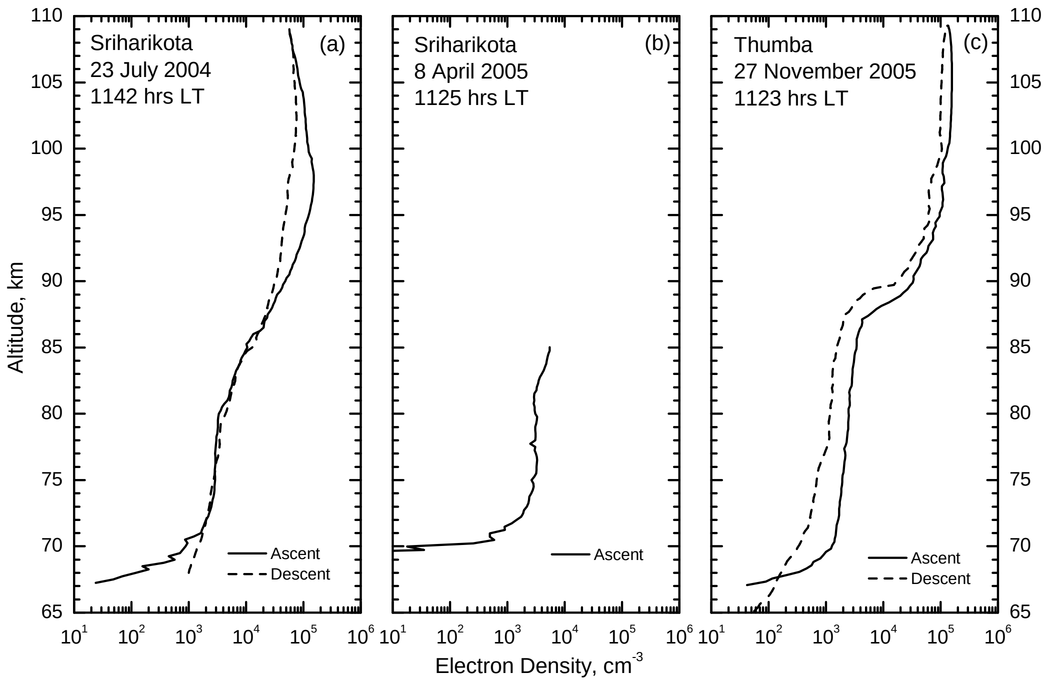

Figure 3.3: *Ascent and descent electron density profiles from the main channel of the Langmuir probes flown on RH-300 MK II rockets during the three flights.*

only 3 km from 67-70 km. Above 70 km, the density increased very slowly up to 80 km and beyond 80 km, the density once again increased rapidly up to the peak of the profile at 95 km. The peak density at this altitude was 1.5×10^5 cm^{-3}. After 95 km, the density started reducing slowly and attained a value of 5×10^4 cm^{-3} at 109 km.

Similarly, during Flight 2 there was a very rapid increase at the base of the ionosphere (Fig. 3.3b). The density changed by two orders of magnitude from 10 to 1000 cm^{-3} in a vertical extent of 3 km from 69-72 km. Above 72 km, the density increased slowly up to 82 km. Above 82 km, the density started increasing more rapidly up to 85 km, beyond which there is no data. It is interesting to note that these features in Flight 1 and Flight 2 match very well with in a vertical range of 2 km.

Flight 3 was conducted from Thumba, an equatorial station. During this flight also, the electron densities built up very fast at the base of the ionosphere. The electron density changed by two orders of magnitude from 10 to 1000 cm^{-3} in a 3 km vertical extent from 67 - 70 km (Fig. 3.3c). Above 70 km, the electron density increased very slowly up to 87 km. From 87 to 90 km, there was a rapid increase and above 90 km, it increased slowly up to 100 km. From 100 to 110 km, the density was more or less constant and $\sim 1.5 \times 10^5$ cm^{-3}. The E-region ledge, which is typical of equatorial lower ionosphere, is seen from 87 to 90 km in this flight.

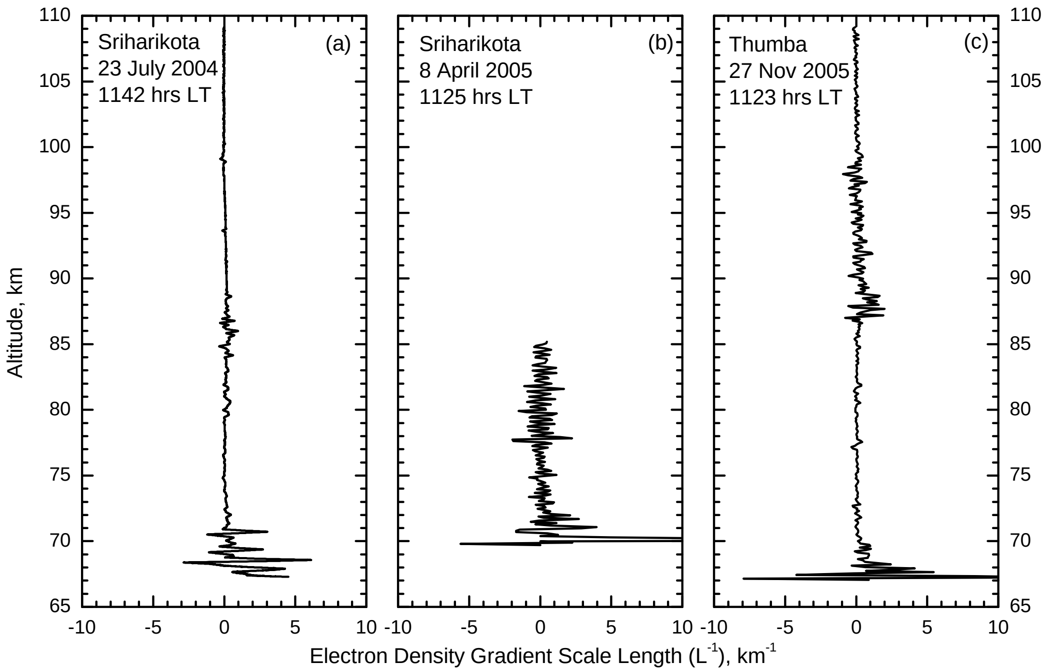

Figure 3.4: *Electron density gradient scale length, L^{-1} over 200 m during the ascent of the three flights.*

Very strong positive and negative electron density gradients were present in vertical extents ranging between 2 to 12 km in all the three flights as shown in Fig. 3.4. The gradients were very strong at the base of the ionosphere in the altitude region 67–72 km, where the electron densities were building up. Typical values of the electron density gradient scale length (L^{-1}) in this altitude region ranged from -5 to 5 km^{-1}. In the higher altitudes the values were much smaller and ranged from -1.0 to 1.0 km^{-1}. During Flight 1 strong gradients with L^{-1} ranging from -3 to 6 km^{-1} were present in 67–70 km region and moderate gradients with L^{-1} ranging from -1 to 1 km^{-1} were present in 79–89 km region. During Flight 2, the gradients were very strong from 69–72 km with L^{-1} ranging from -5 to 10 km^{-1}, from 72–77 km, there were small gradients with L^{-1} ranging from -1 to 1 km^{-1} and from 77–85 km, the gradients were slightly larger with L^{-1} ranging from -2 to 2 km^{-1}. And during Flight 3, strong gradients were once again seen in the lower altitudes from 67–70 km with L^{-1} ranging from -8 to 10 km^{-1} and moderate gradients from 87–99 km with L^{-1} ranging from -1 to 2 km^{-1}.

3.2 Geophysical Conditions

Fig. 3.5 shows the ΔH variation during the period 22-24 July 2004 observed by the ground-based magnetometers at Tirunelveli (8.7°N, 77.8°E) and Alibag (18.6°N, 72.9°E) in the top and the middle panels, respectively. The bottom panel shows the difference between the ΔH variation at both these stations. By taking the difference, the global geomagnetic variation that is seen at both latitudes is removed and the variation in ΔH due to the equatorial electrojet over Tirunelveli is observed. As seen by these ground-based magnetometers located at Tirunelveli and Alibag, the day of launch of Flight 1 was magnetically disturbed as there was a geomagnetic storm during 22-24 July 2004. According to the National Geophysical Data Center (NGDC), NOAA, this storm was observed by many Indian stations, *viz.,* Nagpur, Hyderabad and Pondichery, in addition to Alibag and Tirunelveli. There was a sudden commencement at 1600 hrs LT on 22 July 2004 and the storm lasted upto 0230 hrs LT on 24 July 2004. Another storm also commenced in the afternoon of 24 July 2004 as can be seen in Fig. 3.5, but the discussion on this second storm is out of the scope of the present work. The figure also shows that the current system was counter electrojet during the morning hours on the day of launch of Flight 1, indicating strong perturbations in the wind system.

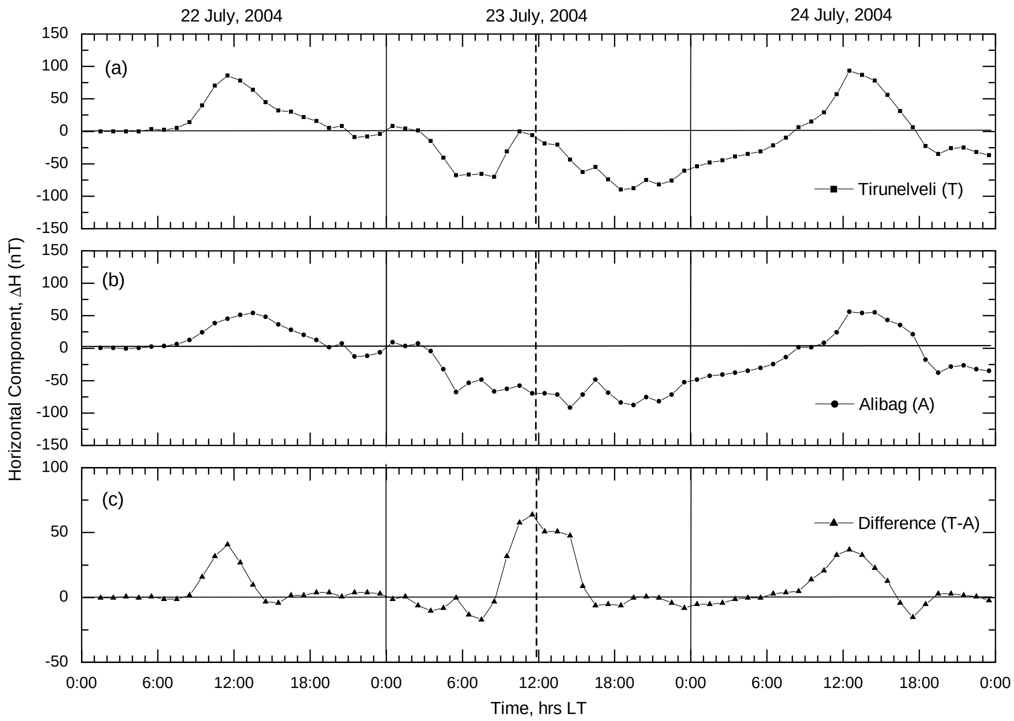

Figure 3.5: *ΔH variation over (a) Tirunelveli (8.7°N, 77.8°E) (b) Alibag (18.6°N, 72.9°E) and (c) Difference in ΔH variation between Tirunelveli and Alibag*

The Ap index on 23 July 2004 was 52, the equivalent ΣKp index was 38 and the F10.7 cm flux on that day was 170.4 sfu. The 3-hourly ap index on the day of the flight and on a day before and after the day of flight, *i.e.,* during the period 22-24 July, 2004 is given in Fig. 3.6a. The figure also shows the launch time of the rocket at 1142 hrs LT on 23 July 2004 with an arrow. An ap index greater than 30 indicates geomagnetic storm conditions. The figure shows that the ap index started to increase at around 1600 hrs LT on 22 July 2004, *i.e.,* at the time of the sudden commencement of the storm. It increased to 132 by 0400 hrs LT on 23 July 2004 and

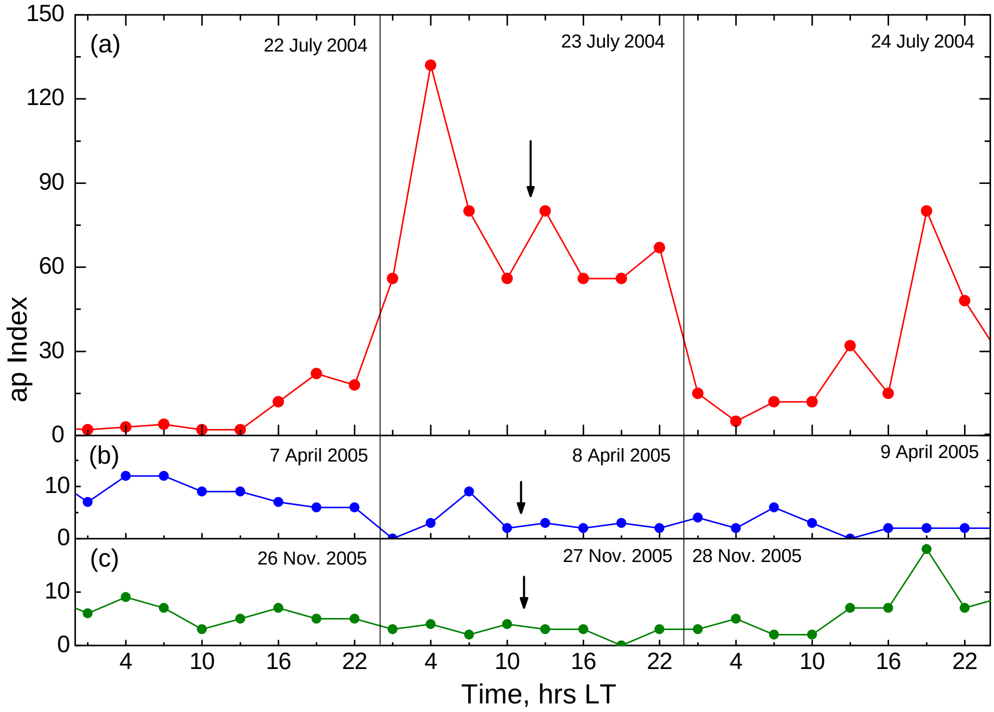

Figure 3.6: *The 3-hourly ap index from (a) 22 to 24 July 2004, (b) 7 to 9 April 2005 and (c) 26 to 28 November 2005. The arrow indicates the time of rocket launch during the three flights.*

continued to remain above 30 until midnight. Hence, the electron density measurements by the Langmuir probe on 23 July 2004 flight were conducted during a geomagnetic storm.

The days on which the other two flights were conducted, *viz.,* 8 April 2005 and 27 November 2005, were magnetically quiet days. Figs. 3.6b and 3.6c show the 3-hourly ap index for the period 7 to 9 April 2005 and 26 to 28 November 2005. The value of this index during both these periods was much below 30 and Ap index was 3 on both days. The equivalent ΣKp indices were 6 and 5+ and the F10.7 cm flux was 88 and 81 sfu on the two flight days, respectively. Hence these two flights measured the electron densities under geomagnetically quiet conditions over Sriharikota and Thumba.

3.3 Wavelet Plots/Spectrograms

For constructing the spectra of fluctuations between a scale size range of about a kilometer down to about a meter, LP data from all the three channels, *viz.,* main, MF and HF channels was used. The continuous wavelet transform was applied on the data from these three channels separately. First the LP main channel data of the electron density was used to compute the wavelet coefficients using the continuous wavelet transform. The wavelet plots for the Flights 1, 2 and 3 are presented in Figs. 3.7, 3.8 and 3.9, respectively. The left hand panel in each of the plots gives the electron density data used to compute the wavelet coefficients and the contour diagram gives the wavelet power associated with different frequencies, with the color code on the right. The thick black line shown in the wavelet plots is the cone of influence (COI). Outside the COI the spectra is subjected to edge effects and hence cannot be completely relied upon. Errors due to edge effects are introduced as the wavelet assumes that the data is cyclic. In the present data set, the electron density data at the higher altitudes is more or less following the same pattern and is cyclic. Hence the region outside the COI at this edge is very small. However, in the lower altitudes, where the electron density has started to build up, the electron density increases by two orders of magnitude in just 3 km. Hence the region outside COI is larger in the lower altitudes. The white long dashed lines indicate the power at various scalesizes, which are marked at the top of the dashed lines. As the rocket velocity decreases with altitude, the frequency of these scalesizes decreases accordingly, and hence the shape of these curves.

The vertical black dash lines in Figs. 3.7 and 3.8 are the fundamental and the second harmonic of the rocket spin frequency. The spin frequency at 4.6 s^{-1} and its second harmonic at 9.2 s^{-1} are very prominent in Flight 1 (Fig. 3.7) and are seen as bands with large power associated with these frequencies. In Flight 2 also (Fig. 3.8) the spin frequency at 6.15 s^{-1} and its second harmonic at 12.3 s^{-1} are very prominent. The spin is clearly visible in these wavelet plots as the sensor was placed away from the spin axis of the rocket. However, during Flight 3 (Fig. 3.9)

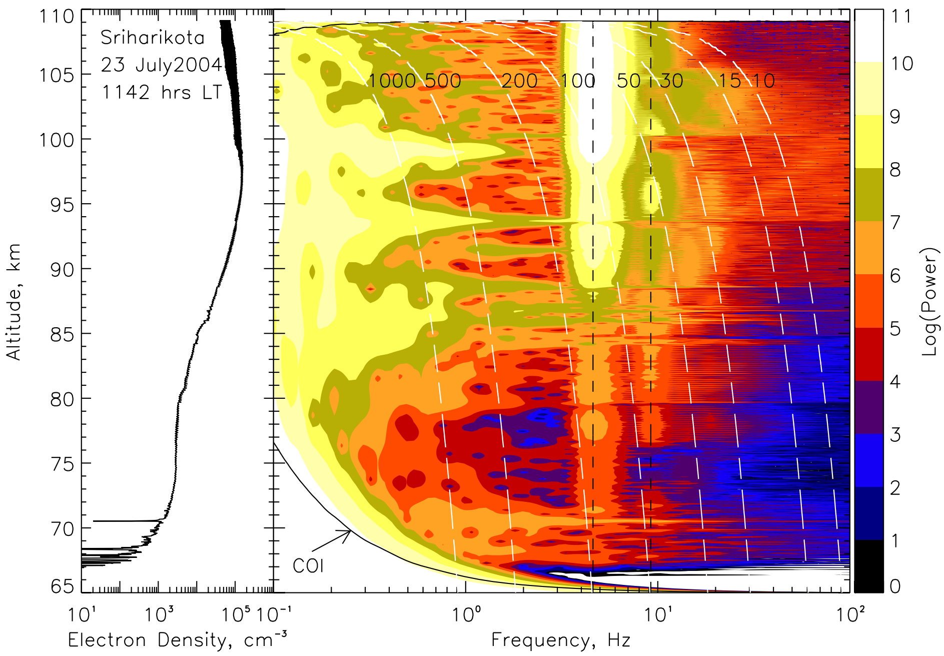

Figure 3.7: *The wavelet power spectrum computed for Flight 1. The left panel shows the electron density data from the LP main channel that was used for the computation of the wavelet coefficients. The thick black line is the cone of influence. See text for further description of the wavelet plot.*

the sensor was placed along the spin axis of the rocket and hence the effect of spin was very small. A single black dash line in Fig. 3.9 shows the spin fundamental frequency at 8.5 s^{-1} and the spin effect is seen only above 100 km, when the rocket was approaching the apogee.

Next the MF and the HF channel power spectra (not shown here) were also computed similarly, taking the complete data set for all the three flights. The complete altitude-averaged power spectra were then computed following the procedure given in Section 2.3.3.

3.4 Altitude-Averaged Power Spectra

All the altitude-averaged power spectra were examined to find if they were characteristic turbulence spectra or not by fitting the Heisenberg model, which gives

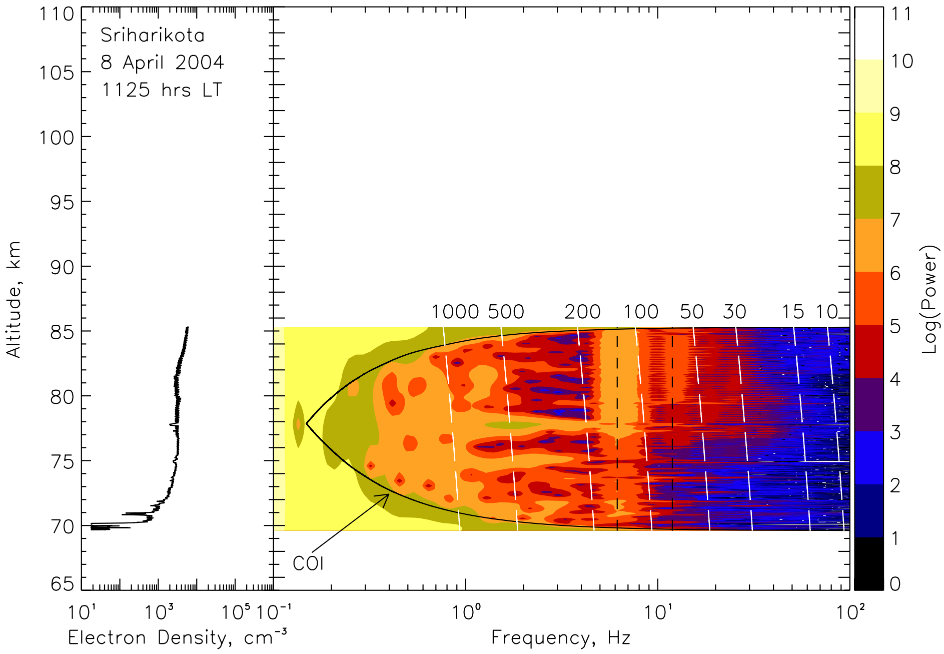

Figure 3.8: *Same as Fig. 3.7 for Flight 2*

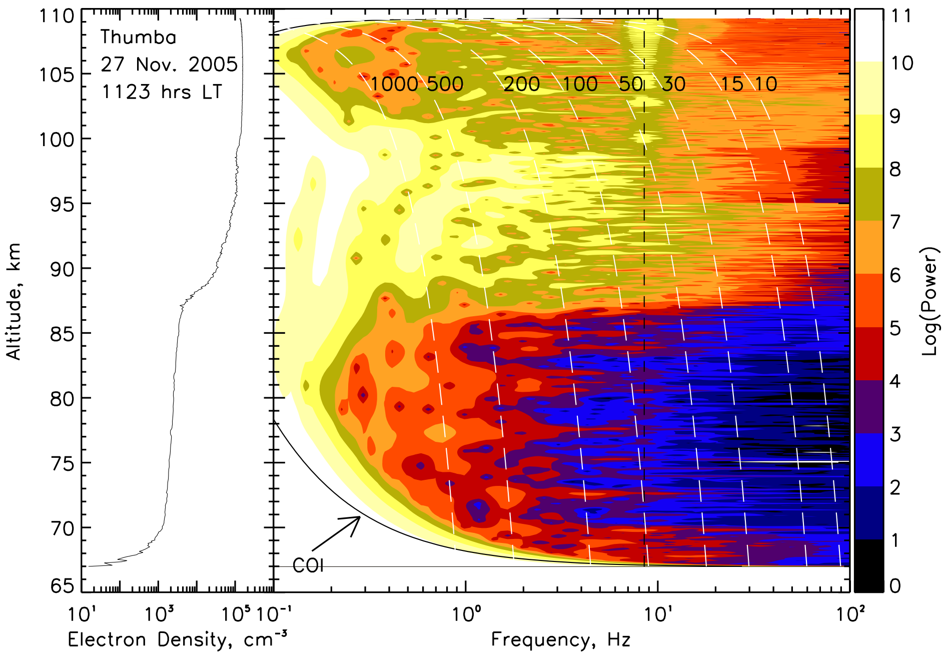

Figure 3.9: *Same as Fig. 3.7 for Flight 3*

Table 3.2: *Number of Turbulent layers*

Flight	Total Number of Altitude-Averaged Power Spectra	Number of spectra to which Heisenberg model could be fitted
23 July 2004	405	102
08 April 2005	152	80
27 November 2005	423	24

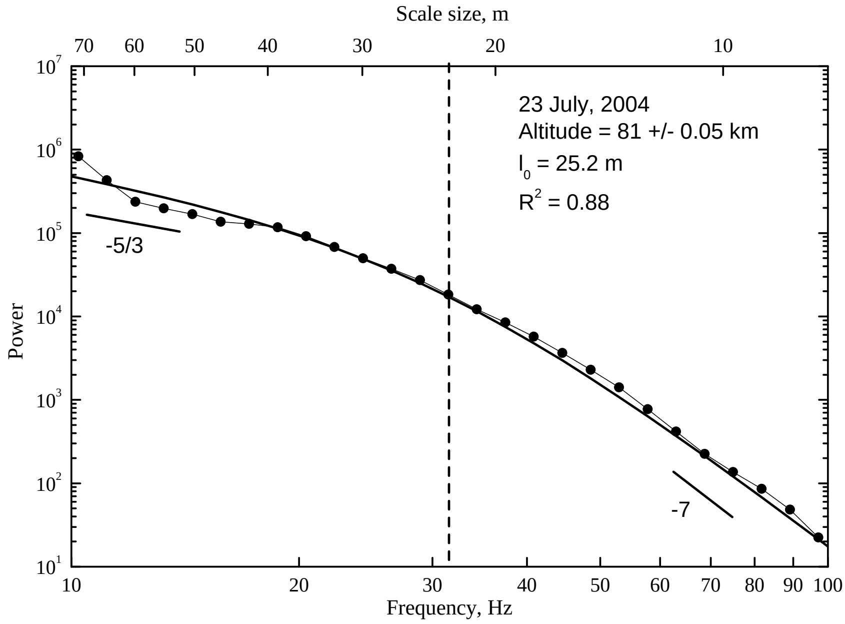

Figure 3.10: *Altitude-averaged power spectra in a 100 m bin around 81 km during Flight 1. The thick solid line is the best fit of the Heisenberg model and the dashed line is the model derived inner scale of turbulence (l_0) and has a value of 25.2 m.*

a smooth transition from the inertial subrange ($n = -5/3$) to the viscous dissipation regime ($n = -7$). The number of spectra to which this model could be fitted, and thus showing the presence of turbulence, are given in Table 3.2. For Flight 1, 102 spectra out of the 405 altitude-averaged power spectra were fitted with the Heisenberg model in the altitude region of 75–89 km and for Flight 2, 80 out of 152 spectra could be fitted with the Heisenberg model in the altitude region of 75–85 km. Examples of few spectra for Flight 1 where Heisenberg model could be fitted are given in Figs. 3.10 and 3.11 at 81 and 86 km, respectively. The solid circles are the altitude-averaged powers at different frequencies and a secondary x-axis

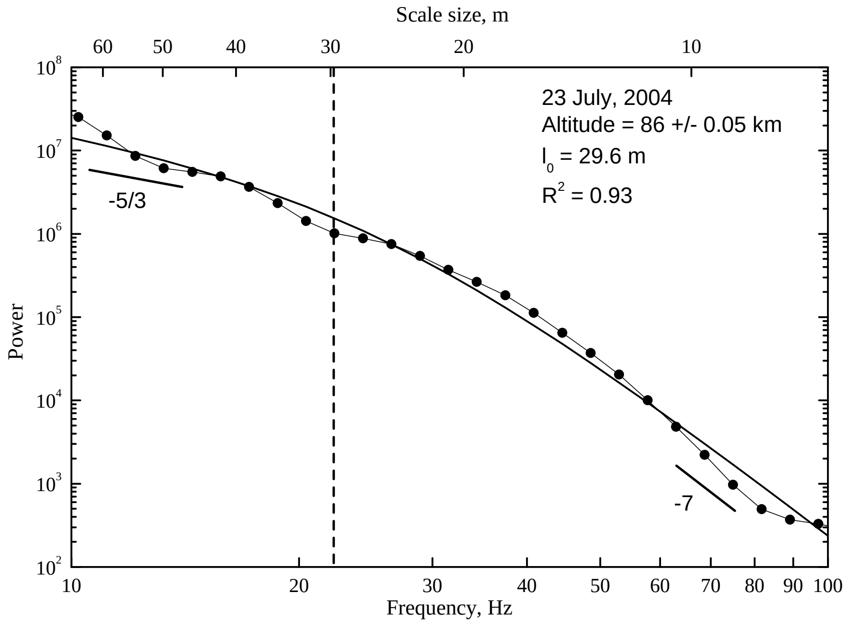

Figure 3.11: *Same as Fig. 3.10 at 86 km and* $l_0 = 29.6m$.

on the top shows the corresponding scalesizes. The thick solid line is the best fit of the Heisenberg model, which identifies the inner scale unambiguously and is shown by the vertical dashed line. At 81 km the inner scale is identified at 25.2 m and at 86 km it is 29.6 m. Similarly, the altitude-averaged power spectra of the other two flights also were verified.

3.5 Layers of Turbulence

As mentioned above, not all spectra showed the characteristic slopes of turbulence indicating that turbulence was not present in all altitude ranges. The altitude-averaged power spectra showed the presence of turbulent layers in 67–89 km region during Flight 1 and in 70–85 km during Flight 2, for which the data was available only upto 85 km. Most of these layers of turbulence had thickness in the range of 1 to 3 km, but some of the layers, it was found, had thickness as small as 100 m. The thick layers observed were sandwiched between the thin layers and

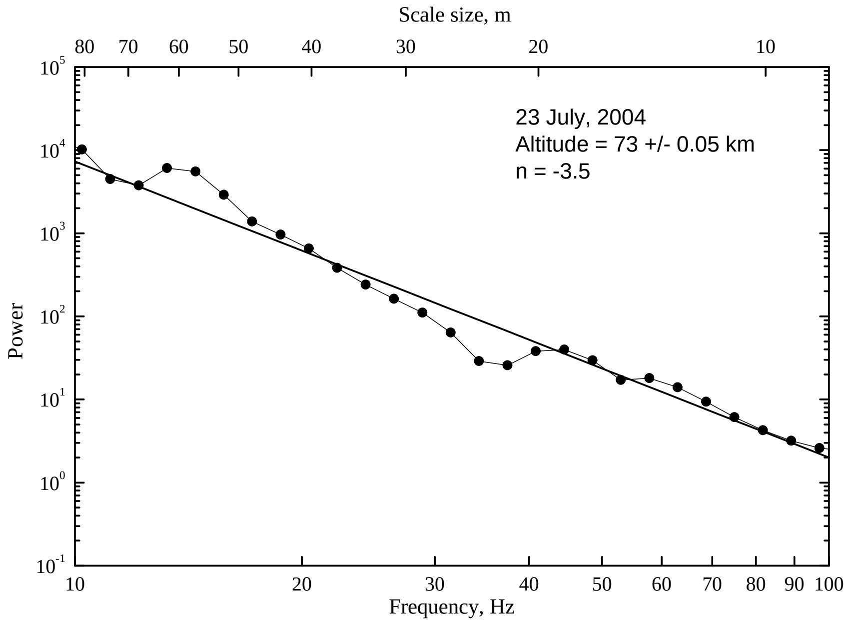

Figure 3.12: *Altitude-averaged power spectra in a 100 m bin around 73 km during Flight 1. The slope of the spectra is -3.5.*

were also interspersed between regions of stability, *i.e.,* no turbulence. Also, these thin layers were present mostly at the edge regions of turbulence. During Flight 1 the thin layers were concentrated at 75–76 and 85–89 km, where as during Flight 2 they were concentrated at 75–76 and 84–85 km. These regions are the edge regions of the main turbulence region in Flights 1 and 2, respectively. Regions where there is no turbulence do not show the characteristic slopes of $-5/3$ and -7. An example of such a spectrum in the region of stability, where no turbulence was observed, is given in Fig. 3.12 for Flight 1 at 73 km.

In the wavelet spectra for the region 67–71 km in these two flights (Flights 1 and 2), spectral indices whose values are very close to $-5/3$ were observed which is an indicator of the inertial subrange, but the viscous dissipation regime, where the slope is expected to be around -7, could not be observed. This was because the inner scale values in this altitude region would have been very small and hence beyond the range of the instrument used. Because of this the Heisenberg model could not be fitted in this altitude region and the turbulence parameters could not

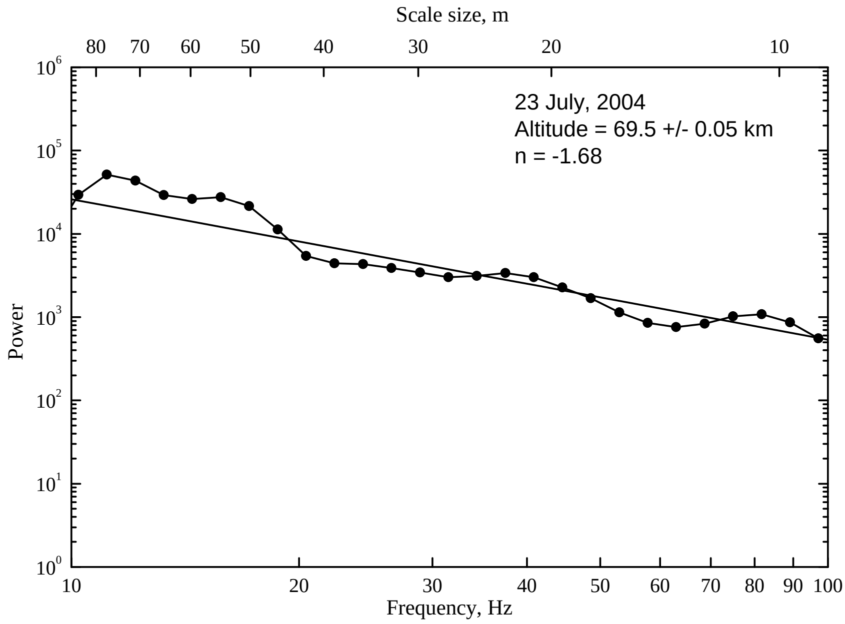

Figure 3.13: *Altitude-averaged power spectra in a 100 m bin around 69.5 km during Flight 1. The slope of the spectra is* -1.68.

be calculated. An example of such a spectrum at 69.5 km for Flight 1 is given in Fig. 3.13. The slope of this spectrum is -1.68, which is the spectral index of ISR indicating that turbulence was present at this altitude also.

For Flight 3 only 24 out of the 423 altitude-averaged spectra could be fitted with the Heisenberg model in the altitude region from 70 to 87 km. Above 87 km, though the altitude-averaged power spectra showed the characteristic slopes of $-5/3$ and -7 and the Heisenberg model could be fitted with correlation coefficient exceeding 0.9, the inner scales identified by the model fit were, however, very small. An example of such a spectra is given in Fig. 3.14 where l_0 is found to be 15.2 m. Such small inner scales result in unrealistic energy dissipation rates and such spectra have not been included in the present study of mesospheric turbulence.

The most important result which came out from the present study is the presence of thin layers of turbulence having thickness in the range of 100-200 m. A statistics of these thin layers as well as the thick layers of turbulence for all the layers is given in Figs. 3.15, 3.16 and 3.17 for the three flights, respectively. During

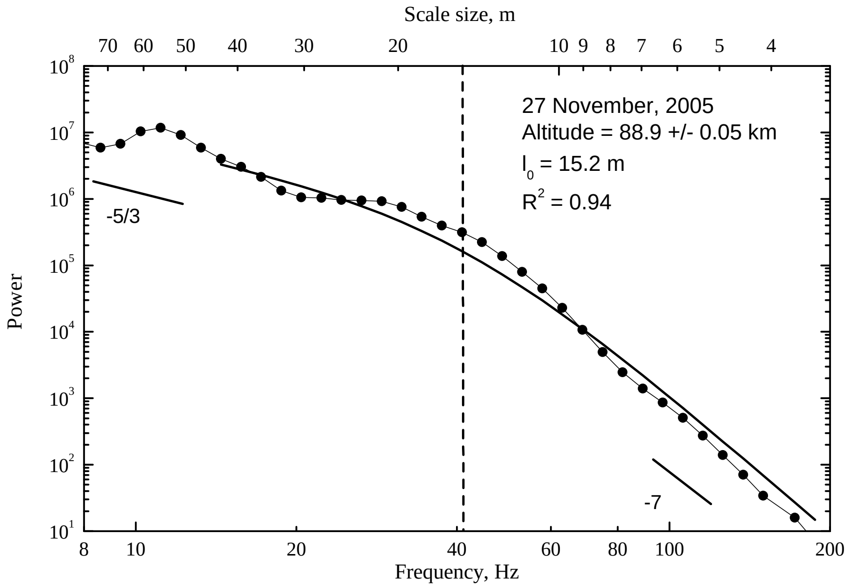

Figure 3.14: *Altitude-averaged power spectra in a 100 m bin around 88.9 km during Flight 3. The thick solid line is the best fit of the Heisenberg model and the dashed line is the model derived inner scale of turbulence (l_0) and has a value of 15.2 m.*

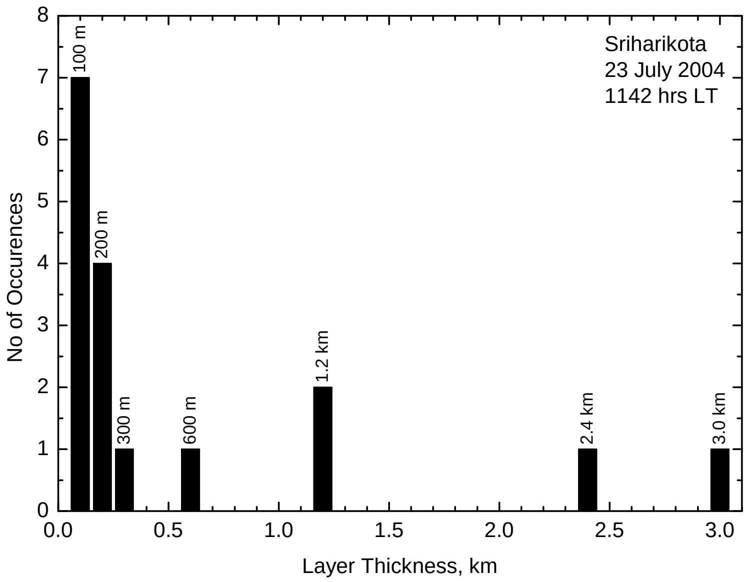

Figure 3.15: *Statistics of layer thickness during Flight 1.*

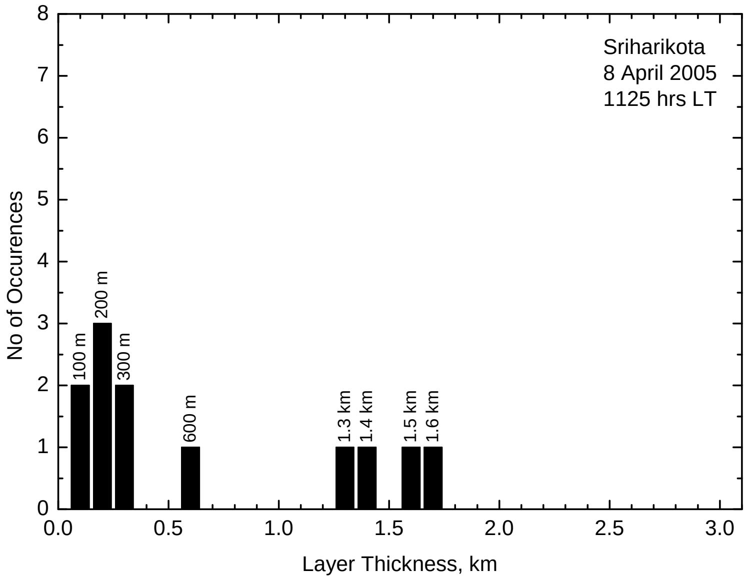

Figure 3.16: *Statistics of layer thickness during Flight 2.*

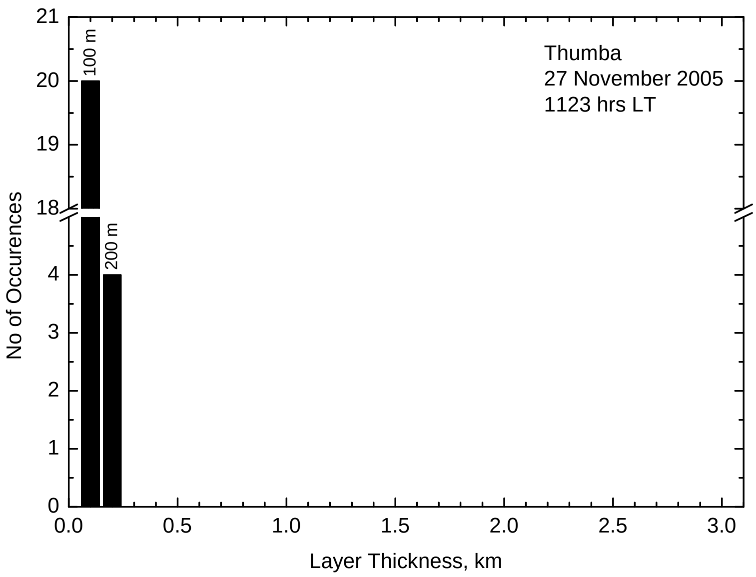

Figure 3.17: *Statistics of layer thickness during Flight 3.*

Flight 1, seven 100 m thick and four 200 m thick layers were observed and during Flight 2, two 100 m thick and three 200 m thick layers were observed, which were concentrated a the edges of the main turbulence regions in both the flights. Layers of 300 m thickness were also observed in both these flights. During Flight 3, twenty 100 m thick and four 200 m thick layers only were observed. These layers were highly scattered and isolated in the 70 to 87 km region.

3.6 Percentage Amplitudes

Percentage amplitude of scale sizes ranging from 1 km down to 10 m were computed from the altitude-averaged power spectra for all the three flights. Fig. 3.18 gives the percentage amplitudes during Flight 1 for different scalesizes, *viz.,* 300, 500 and 1000 m (left panel), 10, 20 and 50 m (right panel). During this flight all

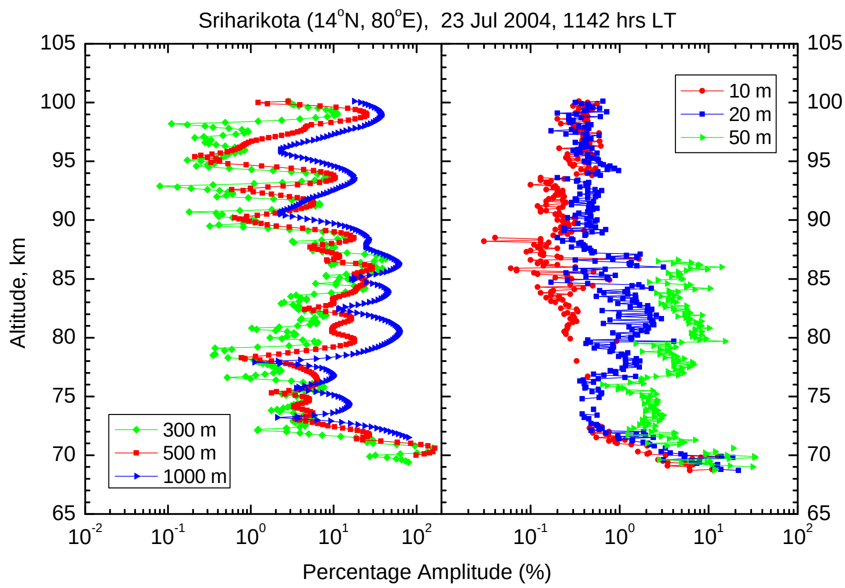

Figure 3.18: *Percentage amplitude of electron density fluctuations of various scalesizes during Flight 1. For the 10 m scalesize, the variation in the 70–80 km region is below the detection limit of the instrument and the 50 m scale size is contaminated by the rocket spin above 87 km and hence are not shown in the figure.*

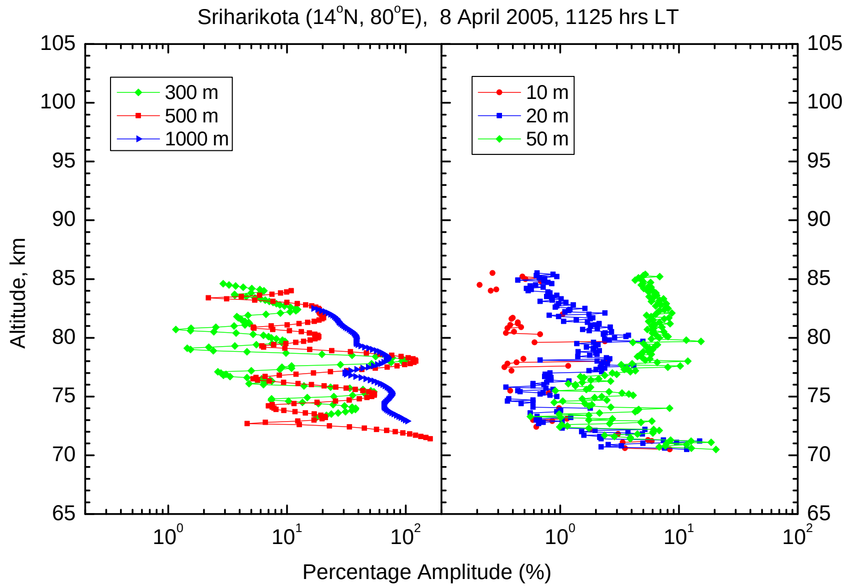

Figure 3.19: *Percentage amplitude of electron density fluctuations of various scalesizes during Flight 2. The 10 m scalesize is above the detection limit at a few altitudes only.*

scalesizes showed large amplitudes below 71 km. This is the region where large electron density gradients were present. The amplitudes are in the range of 10-100% for the large scalesizes from 300 m to 1 km, in the range of 10-20% for the smaller scales. At 70.5 km, the percentage amplitude at 500 m is almost 200%. The altitude region from 78 to 89 km, where moderate electron density gradients were present, also showed high amplitudes of 5 to 50% and 0.1 to 5% for large and small scalesizes, respectively. Also, the amplitudes of the small scalesizes decrease very rapidly with scalesize, which shows the steep -7 slope of the VDR in the altitude region from 75 to 89 km.

Similarly, Fig. 3.19 gives the percentage amplitudes during Flight 2 for the same scale sizes as in Fig. 3.18. The amplitudes of the large scalesizes (300 to 1000 m) are $\sim$ 100% at 70 km, which reduces to $\sim$ 10% at 85 km. All other scales show large amplitudes below 72 km, where large electron density gradients were present as well as above 77 km, where moderate electron density gradients were present.

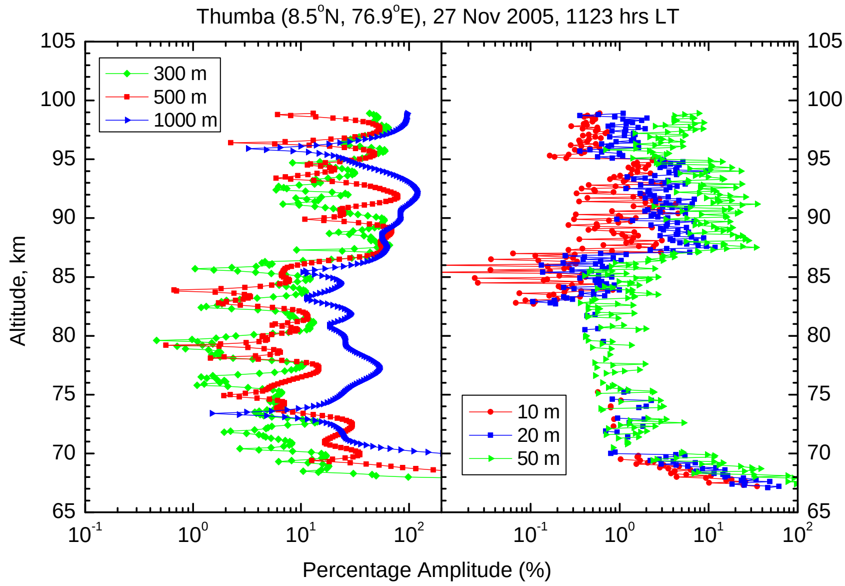

Figure 3.20: *Percentage amplitude of electron density fluctuations of various scalesizes during Flight 3. The 10 and 20 m scalesizes are mostly below the detection limit in the 70–83 km region.*

Below 72 km, the amplitude ranges from 1 to 10% for the small scalesizes. Above 77 km high amplitudes are seen with a peak at around 80 km. The amplitudes for the small scale sizes in this altitude region range from 0.5 to 10%. During this flight also, the amplitudes of the small scalesizes are decreasing very rapidly with scalesize which again shows the steep -7 slope of the VDR in the altitude region from 75 to 85 km.

And for Flight 3, the percentage amplitudes are shown in Fig. 3.20. Large amplitudes are seen in the altitudes region of large electron density gradients from 67 to 71 km and from 87 to 95 km, where moderate gradients were present. The amplitudes of the large scalesizes range from 10 to 100% and those of the small scalesizes range from 0.1 to 100%. Percentage amplitudes in 87 to 95 km region are also high, ranging from 10 to 100% for large scalesizes and from 1 to 10% for the small scalesizes.

3.7 Horizontal Winds from Chaff Release

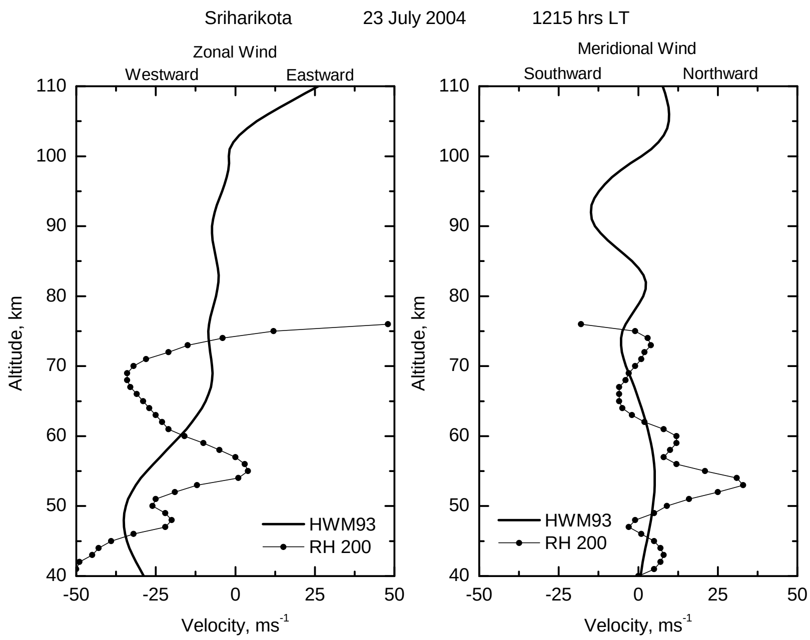

Figure 3.21: *Zonal and meridional wind profiles obtained from radar tracking of metallic chaff released from a RH 200 rocket launched from Sriharikota on 23 July 2004 at 1215 hrs LT. The thick solid line gives the estimate from the HWM93 model.*

Fig. 3.21 shows the zonal and meridional components of the neutral wind derived from radar tracking of metallic chaff released by the RH-200 rocket launched at 1215 hrs LT on 23 July 2004. Zonal component of the wind was predominantly westwards for the entire height range except that it became eastwards above about 74 km. Strong shears in zonal winds were present between 73 and 76 km. As shown in Fig. 3.21, moderate shears in the meridional component of the wind were also present in 70–76 km altitude range, establishing that the horizontal wind in the height range of 70–76 km had shears of about $20ms^{-1}km^{-1}$. Because of inherent limitation of this rocket-chaff technique, it was not possible to measure wind velocities beyond the height range of 75–76 km (*Chakravarty et al.*, 1992). Estimated winds from the HWM93 model (*Hedin et al.*, 1996) are also given in Fig. 3.21, which

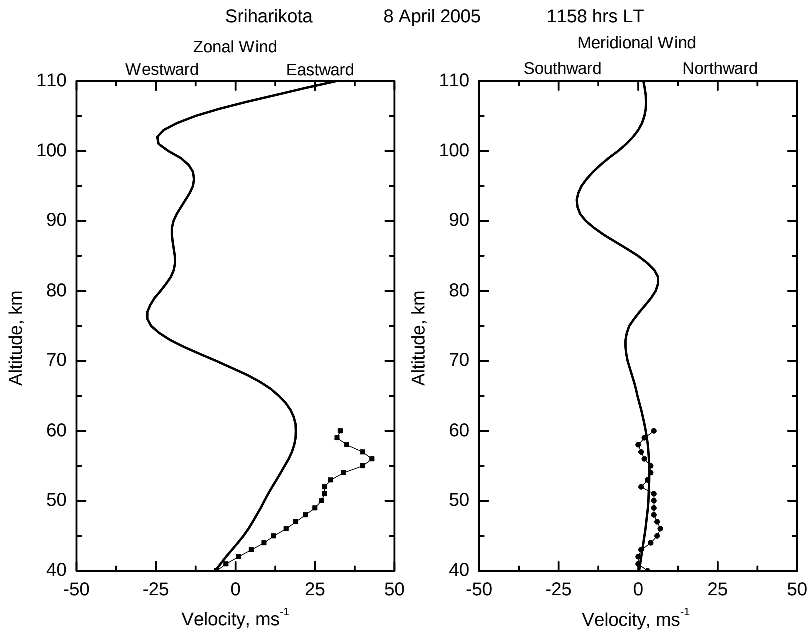

Figure 3.22: *Same as Fig. 3.21 for Flight 2.*

do not show such large shears. It is therefore concluded that there was intense dynamic activity on the day of the flight.

Fig. 3.22 shows the zonal and meridional components of the neutral wind derived from radar tracking of metallic chaff released by the RH-200 rocket launched at 1158 hrs LT on 08 April 2005. The wind velocities were measured up to an altitude of 60 km only. Zonal component of the wind was eastward for the entire height region from 40–60 km with no shears. The meridional component was predominantly northward. The figure also contains the estimated winds from the HWM93 model (*Hedin et al.,* 1996). The chaff observed winds and the winds from the model are comparable below 60 km.

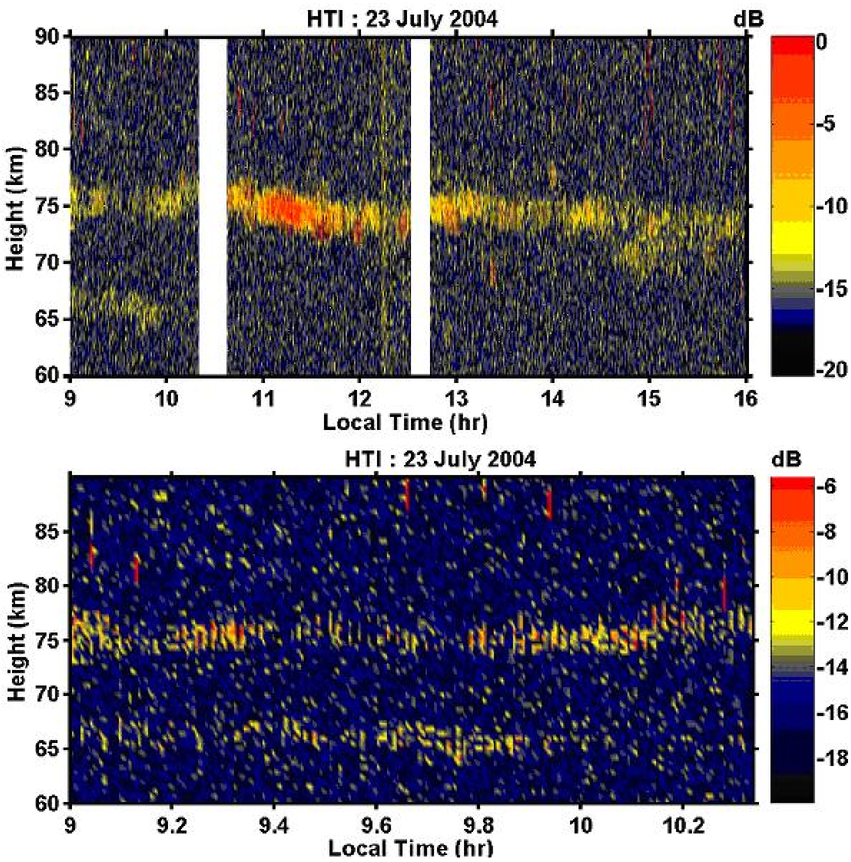

Figure 3.23: Height Time Intensity (HTI) diagram constructed from MST radar echoes at Gadanki on 23 July 2004, with 450 m altitude resolution. The top panel shows the strength of radar echoes during 0900 - 1600 LT and the bottom panel shows the amplified view of echoes during 0900 - 1030 LT. Scales on the right shows the echo SNR.

3.8 Radar Observations

3.8.1 Mesospheric echoes and variabilities

Fig. 3.23 shows height-time intensity (HTI) diagram of mesospheric echoes observed on 23 July 2004 for all scans taken together at different beam positions. Top panel shows the HTI diagram during 0900 - 1600 LT and the bottom panel shows the amplified view of the same diagram during 0900 - 1030 LT to show the presence of the layer in 65-67 km region. Echo SNR is represented in logarithmic scale and the computation was done with noise power reckoned over the coherent integration filter bandwidth of 27.7 Hz. Since the signal bandwidth is typically 2 Hz for the mesospheric echoes observed by VHF radar and also the echoes are weak due

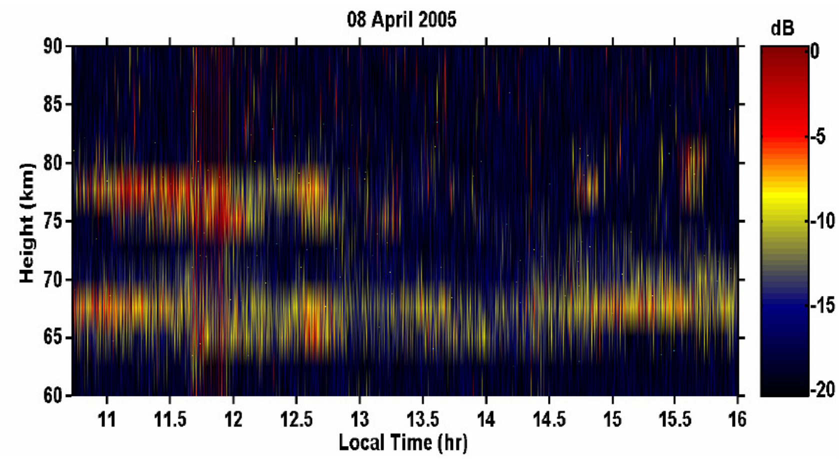

Figure 3.24: *Height Time Intensity (HTI) diagram constructed from MST radar echoes at Gadanki on 8 April 2005, with 450 m altitude resolution. Scale on the right shows the echo SNR.*

to weak refractive index fluctuations/gradients, SNR generally is found to be less than 1. In the present observational scheme, mean noise floor in terms of SNR is -18 dB and SNR of random noisy peak (which has no time and height continuity) is about -12 dB. Thus any signal stronger than -12 dB should be considered as reliable mesospheric echoes. Maximum SNR is found to be 6 dB, which means the mesospheric echoes had a dynamic range of 18 dB (-12 dB to 6 dB). The vertical distribution of radar backscattered signals showed the presence of a strong scattering layer in 73.5–77.5 km region during 1045 and 1315 LT, a scattering layer in 68–70 km region around 1325 hrs and another scattering layer around 65–67 km region during 0900 - 1030 LT.

Similarly, Fig. 3.24 shows height-time intensity (HTI) diagram of mesospheric echoes observed on 8 April 2005 for all scans taken together at different beam positions from 1030 to 1600 hrs LT. There are two strong scattering layers in the 65–71 km and 73–80 kM altitude region. The lower layer was present through out the day from 1030 to 1600 hrs, however, it was weak from 1300 hrs to 1430 hrs LT. The upper layer was present only from 1030 to 1245 hrs LT.

To present the height time variabilities of the echoes in different beam directions, SNRs observed on 23 July 2004 in different beams are shown separately in Fig. 3.25 for the period 1040-1230 hrs LT. As evident from these figures, echoes

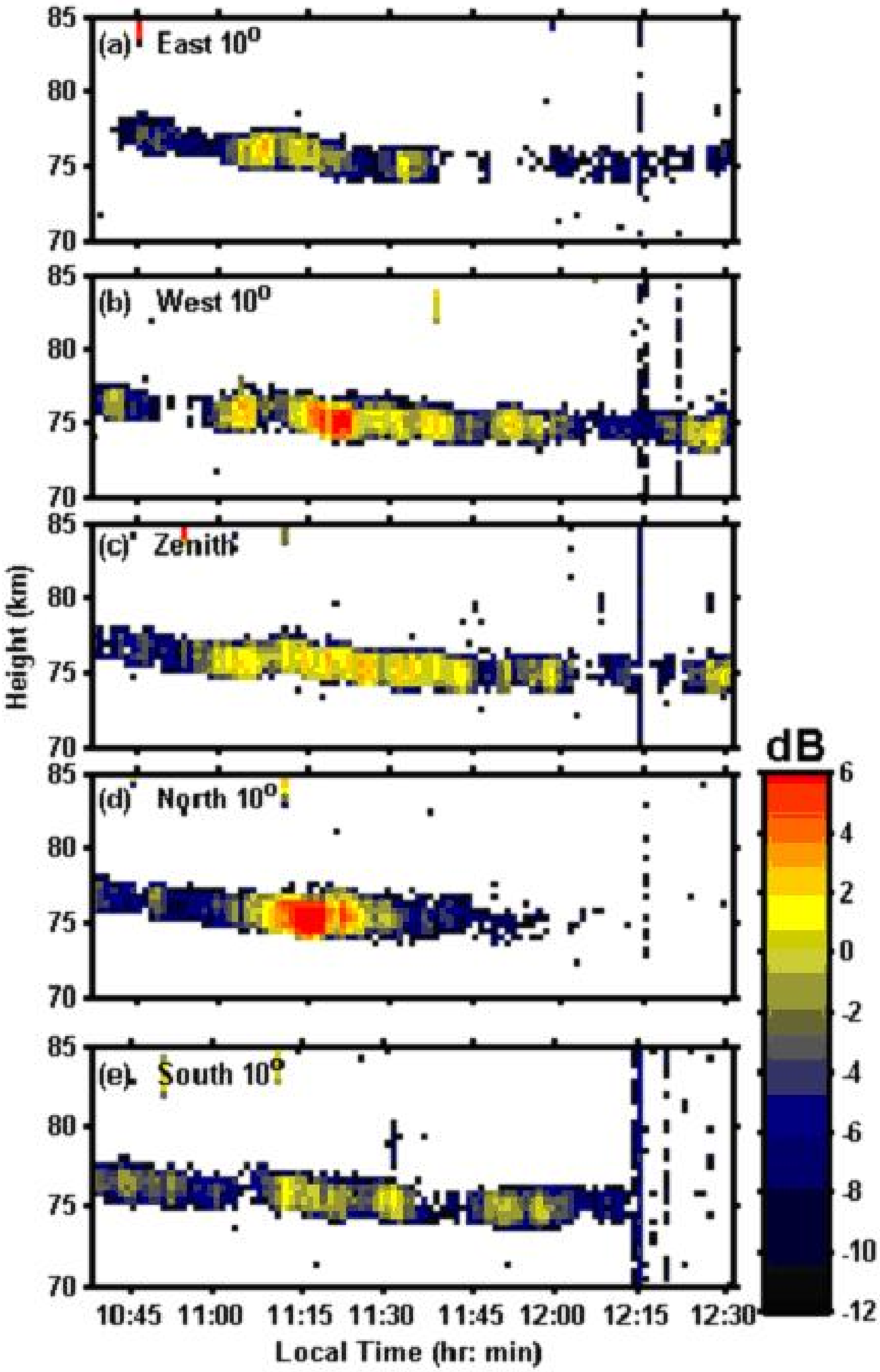

Figure 3.25: *Signal plots of the radar echoes along the five beams on 23 July 2004.*

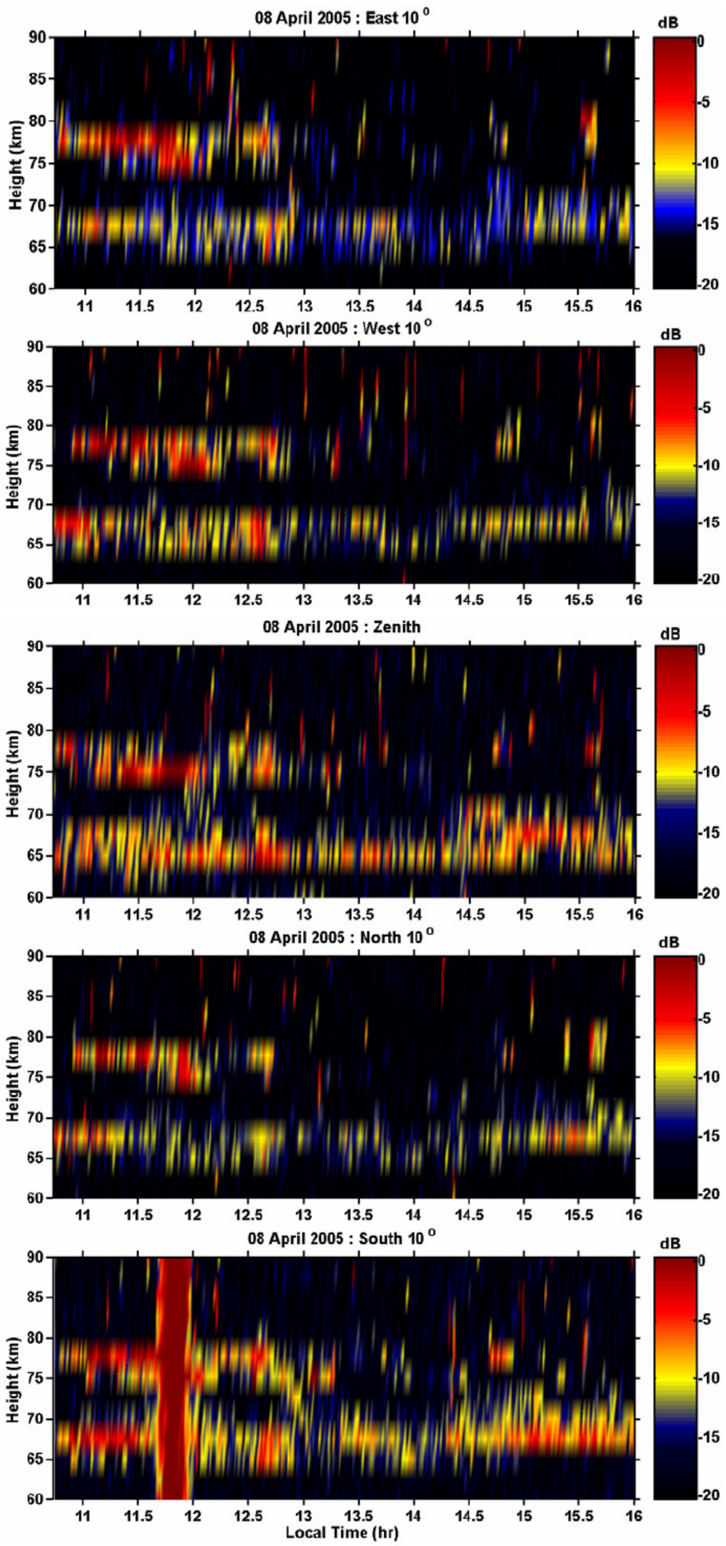

Figure 3.26: *Signal plots of the radar echoes along the five beams on 8 April 2005.*

were observed more times in East, West and zenith beams as compared to North and South beams. It may also be noted that in general echoes are weaker in the East and South beam as compared to West, zenith and South beams. Similarly, SNRs observed on 8 April 2005 in different beams are shown separately in Fig. 3.26 for the period 1030-1600 hrs LT. The zenith and South beams showed slightly stronger echoes in the lower layer but there is no appreciably difference in the strength of the echoes in the upper layer in different beams. The red vertical band of echo observed in the South beam from 1140-1200 hrs LT is due to interference.

3.8.2 Horizontal winds derived using MST radar observations

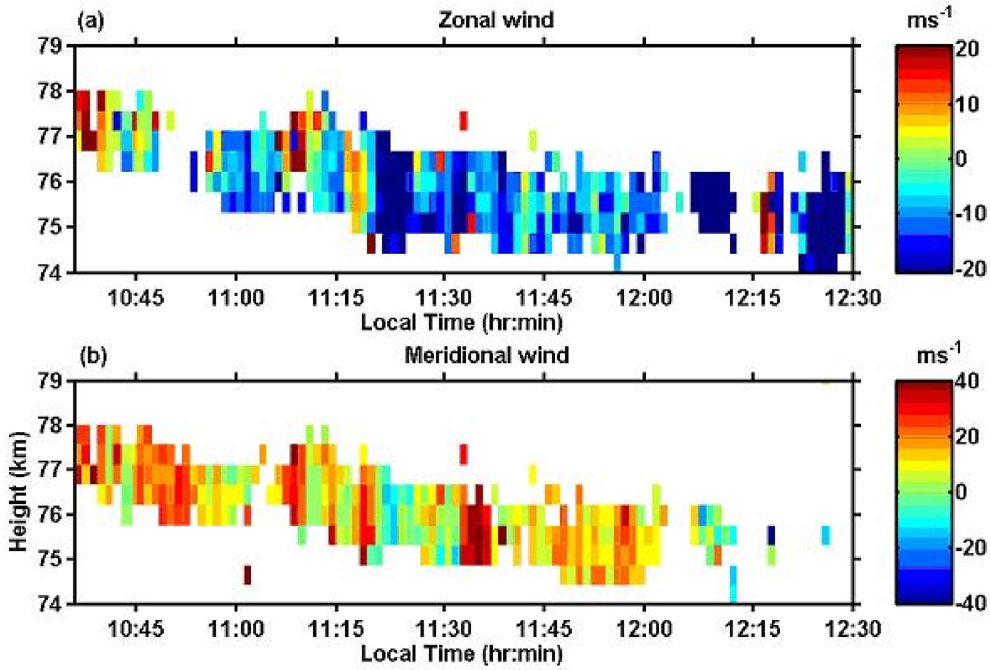

Figure 3.27: *Range-time-velocity maps showing (a) the zonal and (b) meridional wind components over Gadanki on 23 July 2004.*

Fig. 3.27a and 3.27b show zonal and meridional components of the winds derived using the MST radar observations shown in Fig. 3.25. Positive (negative) velocity represents eastward/northward (westward/southward) winds. It can be seen that both zonal and meridional winds are mostly within 20 ms^{-1} and are in

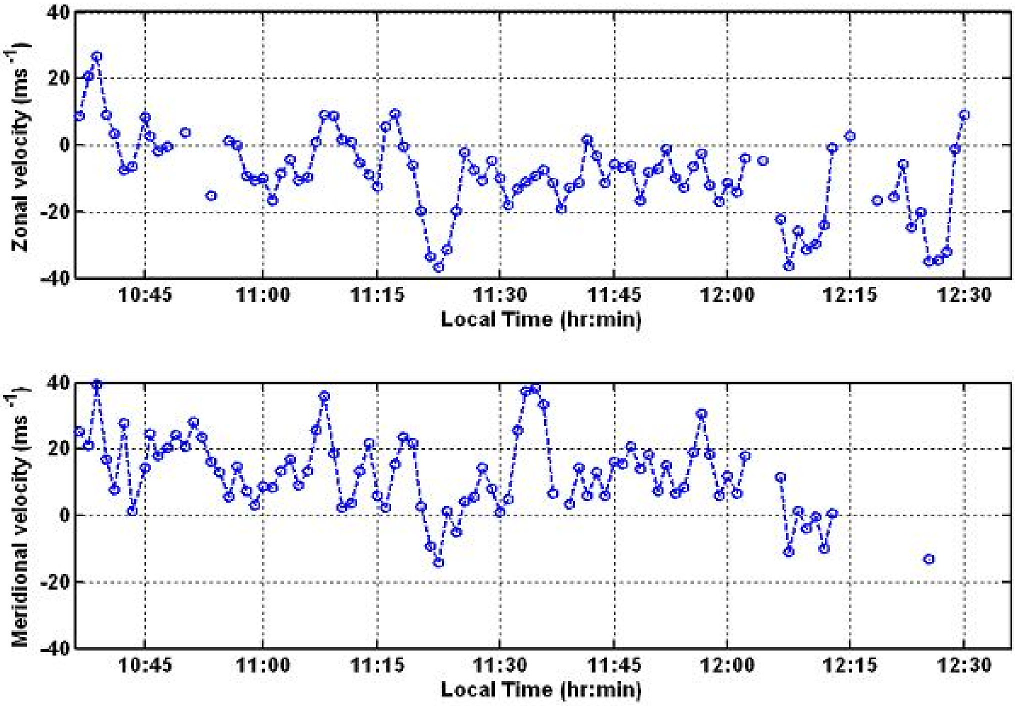

Figure 3.28: *Time variation of the zonal and meridional components of wind averaged over 75-77 km over Gadanki on 23 July 2004.*

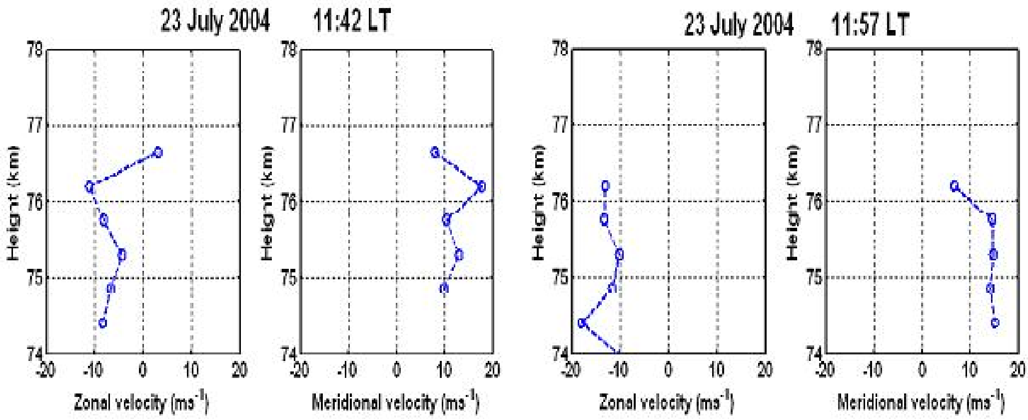

Figure 3.29: *Altitude variation of the zonal and meridional winds over Gadanki at the time of RH 300 rocket launch (1142 hrs LT) and at 1157 hrs LT, which is close to the time of RH-200 rocket launch on 23 July 2004.*

good agreement with those observed by the rocket-borne chaff experiment (Fig. 3.21). The time variation of the zonal and meridional wind components averaged within the altitude region of the scattering layer (75 - 77 km) is shown in Fig. 3.28. The magnitude of the zonal winds, which are mostly westward, varies between -40 ms^{-1} to a few ms^{-1} with most of the points between -20 and 0 ms^{-1}. A periodicity close to 10 min can be seen clearly in both the wind components. The meridional winds are mostly northward and their magnitude varies between 0 and 40 ms^{-1} again with most of the points between 0 and 20 ms^{-1}. To see the altitude variation of zonal and meridional winds, average winds for 7 min duration for an altitude range of 74 - 77 km for 1142 LT and 1157 LT are shown in Fig. 3.29. The first time corresponds to the RH-300 rocket launch time and the other just 15 min after that. It would have been good to compute these wind components around 1215 LT, which was the launch time of Chaff flight but the radar did not observe echoes in all the beams and hence the wind components could not be estimated correctly at 1215 LT. At 1142 LT the zonal velocity was in the range of -10 to 5 ms^{-1} and the meridional component in the range of 10 to 15 ms^{-1}. At 1157 hrs LT, the zonal component was westward with values in the range of -10 to -15 ms^{-1} and the meridional component was close to 15 ms^{-1} with one value at the top echoing region being about 5 ms^{-1}. The two sets of profiles are quite consistent. Comparing with the chaff derived velocities over SHAR, the basic pattern of winds appears similar in nature both in magnitude and direction. The periodicity of 10 min seen both in zonal and meridional components in 75–77 km region points towards the possibility of the presence of gravity waves and hence the turbulence.

3.8.3 Doppler spectral width

Spectral widths observed in different beam directions are shown in Fig. 3.30. These represent mean and standard deviations of spectral widths observed in different directions. Spectral widths presented in zonal (meridional) direction were obtained by combining observations made in East and West (North and South)

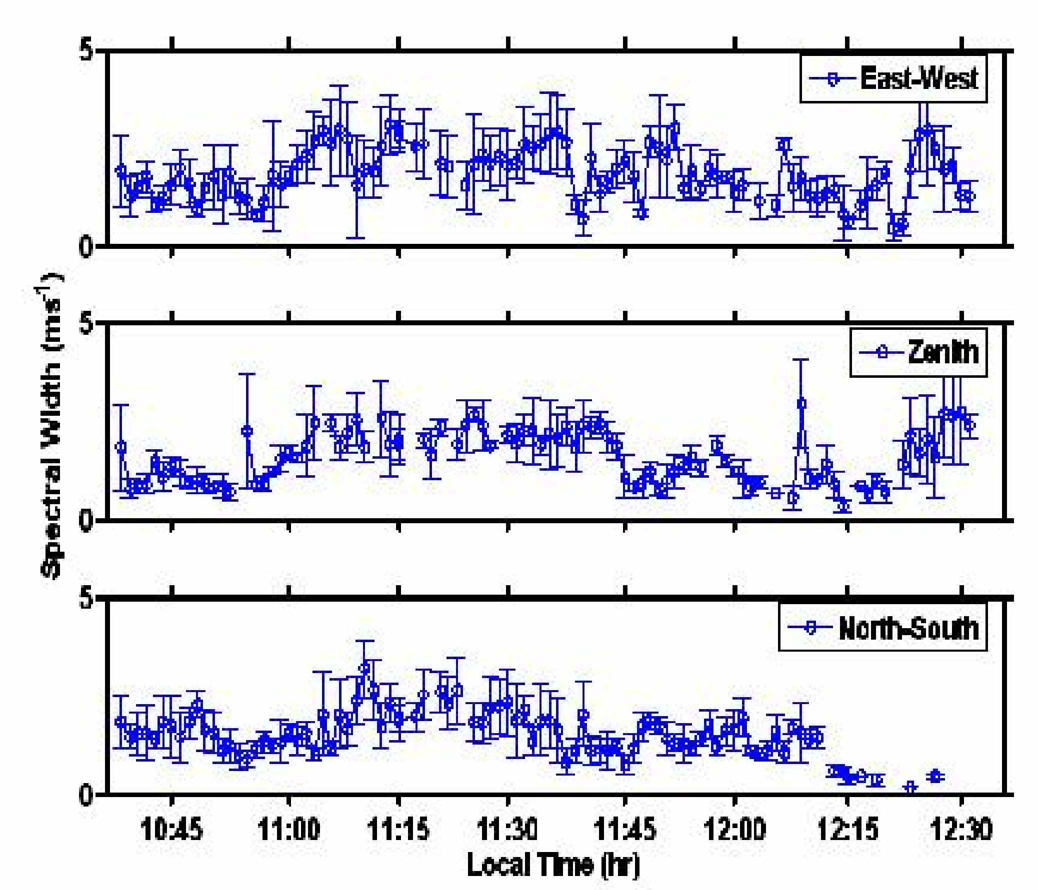

Figure 3.30: *Mean spectral widths along the East-West, Zenith and North-South beams on 23 July 2004.*

beams. In these figures, spectral width represents square root of variance. In general the spectral widths vary between 1 and 3 ms^{-1} with most values between 2-3 ms^{-1}. The values are found to be somewhat more in the East-West beams as compared to North-South beams as well as zenith

3.9 Turbulence Parameters

3.9.1 Turbulence Parameters derived using Rocket Observations

Turbulence parameters were computed for those altitude-averaged power spectra, for which the Heisenberg model fit yielded the inner scale unambiguously, according to the procedures described in Section 1.2.3.

Flight 1

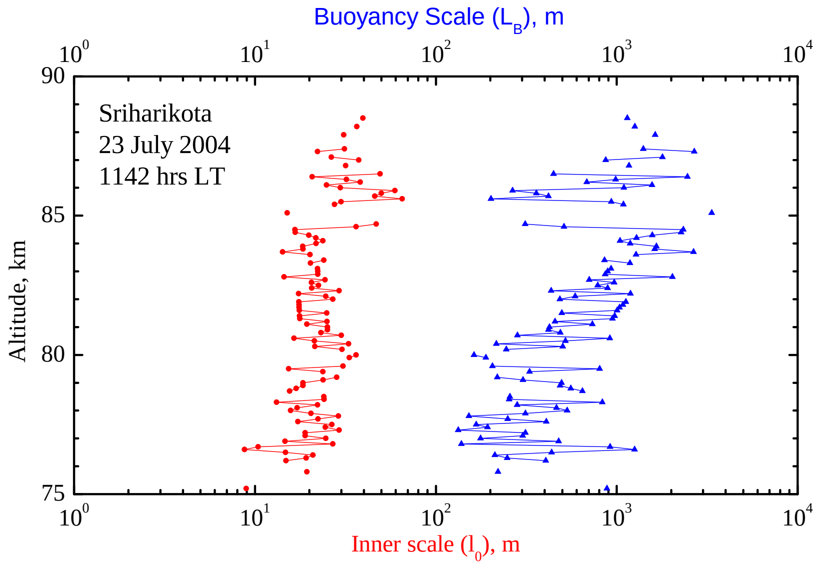

Figure 3.31: *Altitude variation of inner scale (red circles) and buoyancy scale (blue triangles) during Flight 1.*

Fig. 3.31 shows the altitude variation of the inner scale and buoyancy scale during Flight 1. The inner scale (l_0) is shown as red circles and the buyancy scale as blue triangles. The inner scale increased with altitude from 76 to 89 km, with small variations on a finer scale. From 76 to 80 km, l_0 varied over a wide range from 10 to 30 m with a slightly increasing trend and from 80 to 84.5 km, l_0 showed a more prominent decreasing trend from 30 to 15 m. From 84.5 to 89 km, l_0 showed a large variation from 20 to 50 m with an increasing trend. The buoyancy scale, L_B, varied from 120 to 1000 m in the lower region from 76 to 80 km and above 80 km it increased from 200 m to 3 km at 84.5 km. And in the region from 84.5 to 89 km, it varied in the range 200 m to 3 km.

Fig. 3.32 shows the energy dissipation rate (left panel) and eddy diffusion coefficient (right panel) during Flight 1. The energy dissipation rate is inversely proportional to the fourth power of the inner scale, but is also directly proportional

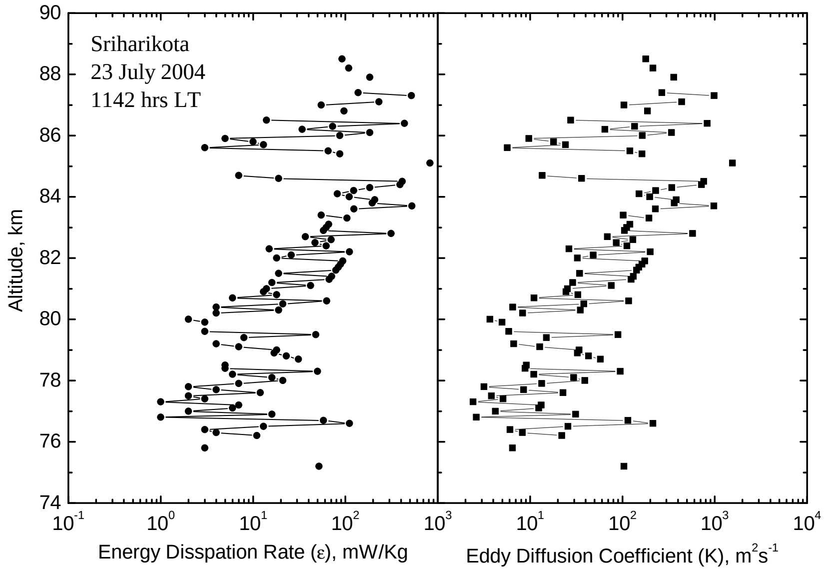

Figure 3.32: *Altitude variation of energy dissipation rate (ϵ) and eddy diffusion coefficient (K) during Flight 1.*

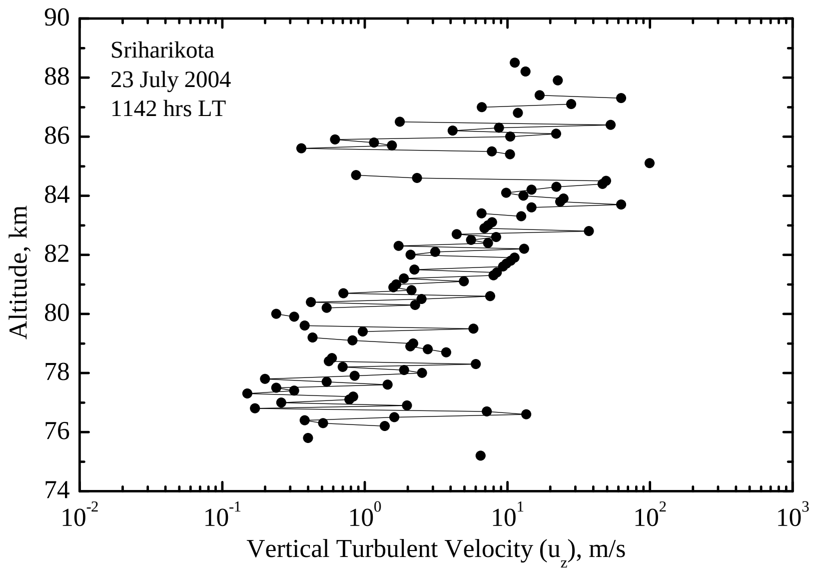

Figure 3.33: *Altitude variation of vertical turbulent velocity (u_z) during Flight 1.*

to third power of the kinematic viscosity, which in turn is exponentially increasing with altitude. Hence the energy dissipation rates also showed an increasing trend with altitude but was opposite in phase to the inner scale. From 76 to 80 km, ϵ varied in the range of 1 to 50 mW/kg with a slightly increasing trend and above 80 km, an increase from 2-3 mW/kg started and reached 500 mW/kg by 84.5 km. In the region from 84.5 to 89 km the variation was very large and was in the range of 5 to 500 mW/kg. The eddy diffusion coefficient also showed a variation similar to the energy dissipation rate. In the 76 to 80 km region eddy diffusion coefficient, K, varied in the range 3 to 100 m^2s^{-1} above which, from 80 to 84.5 km it increased from 5 to 1000 m^2s^{-1} and from 84.5 to 89 km, a large variation in the range from 5 to 1000 m^2s^{-1} is observed. Fig. 3.33 shows the altitude variation of the vertical turbulent velocity during Flight 1. It varied from 0.2 to 6 ms^{-1} in the region from 76 to 80 km, and from 80 to 84.5 km it increased from 0.3 to 60 ms^{-1} and above 84.5 km showed a large variation in the range from 0.3 to 60 ms^{-1} up to 89 km. All turbulent parameters showed high variation and comparatively large values from 80 to 89 km. This is the region where electron density gradients were present during this flight.

Flight 2

Fig. 3.34 shows the altitude variation of inner scale and buoyancy scale during Flight 2. There are no large variations in the scales during this flight as observed in Flight 1. The inner scale showed a steady increase from 15 to 40 m in the altitude region from 75 to 85 km and the buoyancy scale increased from 100 to 600 m. Fig. 3.35 shows the energy dissipation rate (left panel) and eddy diffusion coefficient (right panel) during Flight 2 . The energy dissipation rates increased from 1 to 30 mW/kg and the eddy diffusion coefficient also increased from 2 to 60 m^2s^{-1} from 75 to 85 km. And the vertical diffusion coefficient, shown in Fig. 3.36, was 0.3 ms^{-1} at 75 km and increased to 2 ms^{-1} at 85 km.

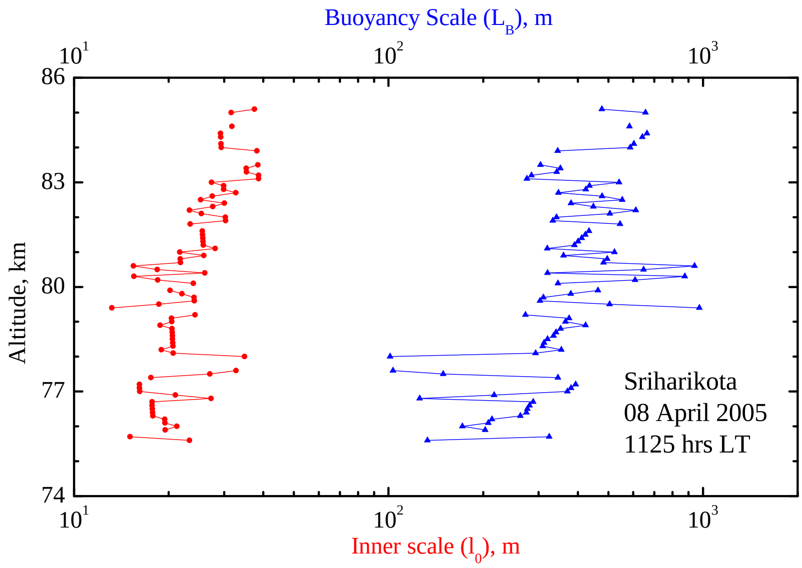

Figure 3.34: *Altitude variation of inner scale (red circles) and buoyancy scale (blue triangles) during Flight 2.*

Flight 3

Fig. 3.37 shows the altitude variation of inner scale and buoyancy scale during Flight 3 . Only isolated layers of turbulence were observed during this flight. Thin layers of turbulence of thickness 100 m were observed from 70 to 78 km, where the inner scales were showed a large variation from 10 to 40 m and the corresponding buoyancy scales were all less than 400 m. The energy dissipation rates in this altitude region were very small and were less then 10 mW/kg and the the eddy diffusion coefficient was less than 20 m^2s^{-1} (Fig. 3.38). The vertical turbulent velocities in this region were less than 1 ms^{-1} (Fig. 3.39). At 80.5 km a thin layer of turbulence of 200 m thickness was observed where the inner scale was ∼20 m and the corresponding buoyancy scale was 700 m. The energy dissipation rate at this altitude was 20 mW/kg and the eddy diffusion coefficient was 50 m^2s^{-1}. The vertical turbulent velocity was 2 ms^{-1}.

Seven isolated turbulent layers of 100 m thickness were observed in the altitude

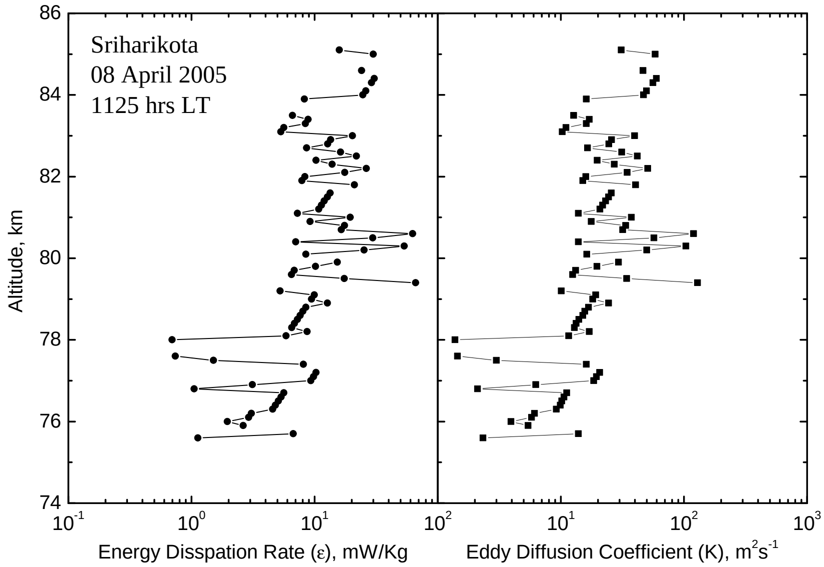

Figure 3.35: *Altitude variation of energy dissipation rate (ϵ) and eddy diffusion coefficient (K) during Flight 2.*

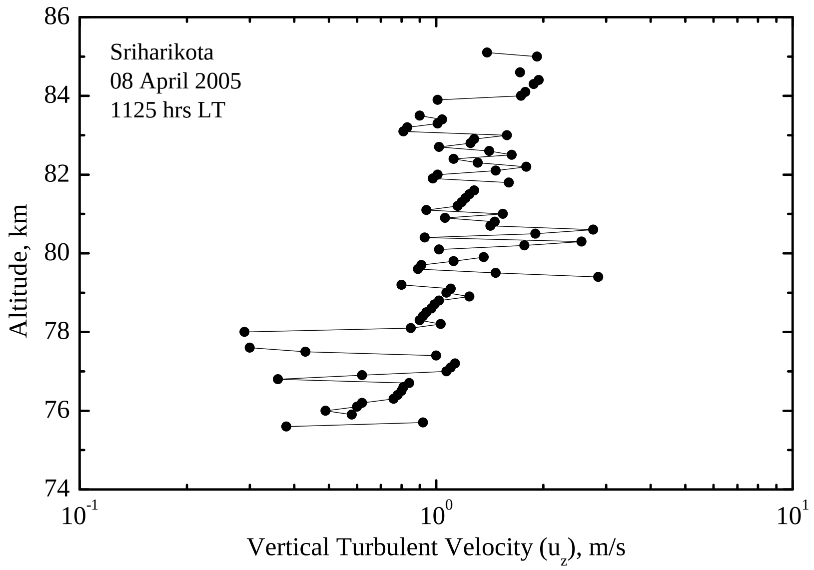

Figure 3.36: *Altitude variation of vertical turbulent velocity (u_z) during Flight 2.*

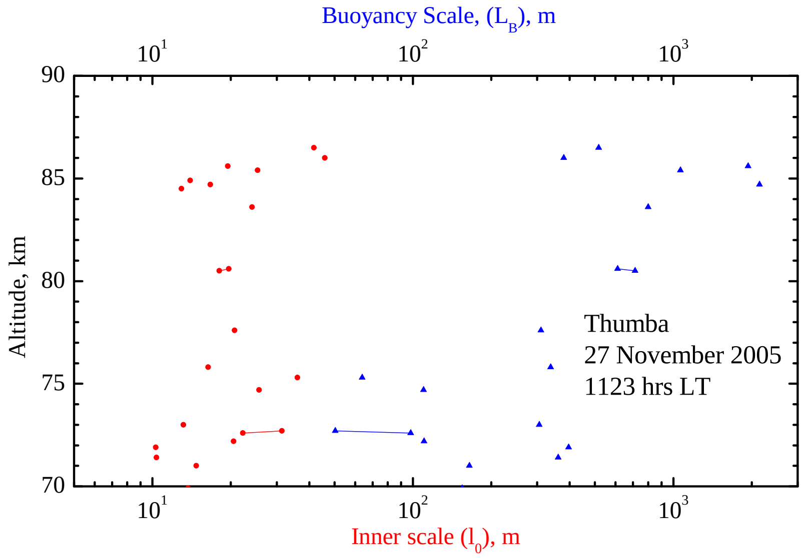

Figure 3.37: *Altitude variation of inner scale (red circles) and buoyancy scale (blue triangles) during Flight 3.*

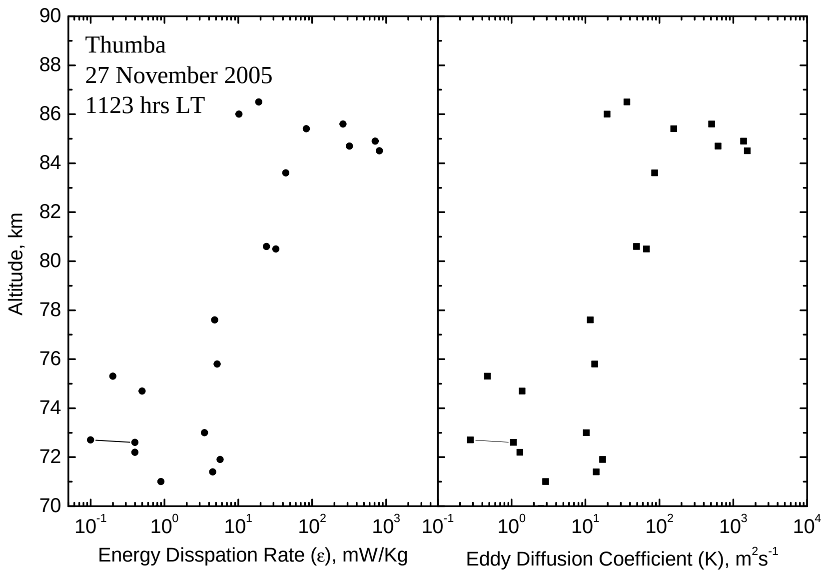

Figure 3.38: *Altitude variation of energy dissipation rate (ϵ) and eddy diffusion coefficient (K) during Flight 3.*

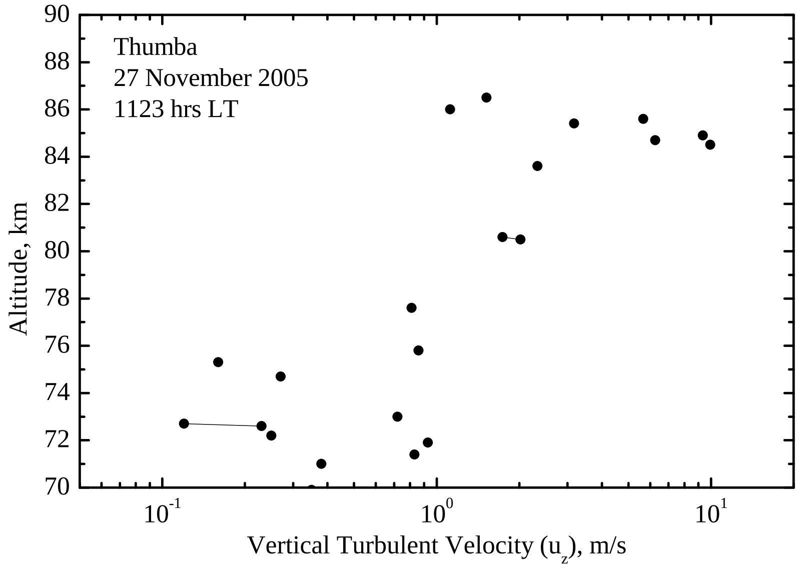

Figure 3.39: *Altitude variation of vertical turbulent velocity (u_z) during Flight 3.*

region of 84 to 87 km. The inner scales ranged from 12 to 40 m, and the corresponding buoyancy scales varied from 400 m to 3 km (Fig.3.37). The energy dissipation rates ranged from 10 to 1000 mW/kg and the eddy diffusion coefficient was in the range of 20 to 2000 m^2s^{-1} (Fig. 3.38). The vertical turbulent velocity was in the range of 1 to 10 ms^{-1} (Fig. 3.39). There are no significant electron density gradients present in this altitude region, however the estimated turbulent parameters were large and varied over a wide range. Also this altitude region is just below the E-region ledge, which is typical of the equatorial lower ionosphere.

In and above the E-region ledge from 87 km and above, where there were strong gradients in the electron density, many altitude-averaged power spectra could be fitted with the Heisenberg model. However the inner scales obtained from the model fits were very small which resulted in very high energy dissipation rates as high as 500 W/kg! Such high ϵ values are not physically possible. This indicates that some mechanism other than neutral turbulence might be responsible for these measurements.

3.9.2 Turbulence Parameters derived using Radar Observations

Most of the values of spectral width observed by the MST radar during Flight 1 were 2 ms^{-1} and hence this value was taken to estimate the energy dissipation rate using the following relation (*Hocking*, 1982).

$$\epsilon \sim 2.9u^2 f_B \tag{3.1}$$

where, f_B is the Brunt-Väisala frequency in Hertz and u is the horizontal rms velocity. The effects of beam broadening and shear broadening have been neglected. *Hocking* (1982) assumed that the rms velocities are equal along vertical and horizontal directions. With this assumption, for the 73.5-77.5 km region, where the radar observed a strong scattering layer on 23 July 2004, the energy dissipation rate is estimated to be 23 mW/kg for an assumed Brunt-Väisala frequency of 20 mHz.

3.10 Discussion and Conclusions

In situ measurements of electron density in the 67 to 90 km region over low and equatorial latitudes showed the presence of strong irregularities. Large percentage amplitudes of these electron density fluctuations can be a result of various processes operating in the mesosphere and lower thermosphere. At altitudes below about 90 km, the only known process which could produce such irregularities in the electron density is the neutral turbulence. There have been very few daytime flights from Sriharikota in the past to study the electron density irregularities in the low latitude mesosphere (*Sinha and Prakash*, 1995; *Chakravarty et al.*, 2004, and references therein). These flights were primarily intended to study the E and F region of the ionosphere. The present flights, viz., Flights 1 and 2, from Sriharikota thus provide valuable measurements to study the electron density irregularities in the mesosphere over low latitudes. This region is observed more closely from 67 km and above and 69 km and above during Flights 1 and 2, respectively. The electron density irregularities observed in the low latitude mesosphere due to neutral turbulence are discussed below.

During the Flight 1, large amplitudes of the larger scalesizes were observed in 78 to 89 km and of smaller scales in 75 to 89 km region (Fig. 3.18). This was also the region of moderate electron density gradients (Fig. 3.4). Fig. 3.31 shows that the turbulent layers were also seen in the same altitude region from 75 to 89 km. In view of this and the fact that this region is highly collisional, it is concluded that the electron density irregularities seen during this flight are produced due to neutral turbulence. Similarly during Flight 2, large percentage amplitudes are seen in the altitude region from 77 to 85 km in all scalesize ranges, which coincides with the altitude range of moderate electron density gradients seen in the region from 77 to 85 km. This is roughly the same altitude region (76-85 km) where layers of turbulence have been identified (Fig. 3.34). Hence the electron density irregularities during this flight are also concluded to be produced due to neutral turbulence.

The electron density variation observed during Flight 3 is similar to what has been observed earlier (*Sinha and Prakash*, 1995, and references therein). The general trend of the daytime electron density profile over Thumba is a rapid increase up to 75 km, followed by a slower increase up to 85 km and a rapid increase up to 100 km above which the density remains almost constant. The electron density profile during Flight 3 is similar to this trend. During this flight, large percentage amplitudes of all scalesizes are seen in the altitude region from 87–90 km. This also coincides with the region from 87–99 km of sharp and moderate electron density gradients. However, layers of turbulence have not been identified in this altitude region. The presence of sharp electron density gradient from 87–90 km shows that these irregularities could have been produced due to the gradient drift instability as the conditions are very suitable for a plasma instability to grow. Below 87 km, thin isolated layers of turbulence have been identified in the altitude regions from 70-75 and from 84-87 km (Fig. 3.37). And at the altitudes of these thin layers, the percentage amplitudes are high, which are seen as spikes in Fig. 3.20. The level of turbulence is low and only thin layers are found during this flight. *Sheth et al.* (2006) have studied the fine structure of the mesosphere using the Jicamarca MST radar. Thin sheets were observed in the SNR maps, similar to the results of FLight 3, and these are thought to be due to isotropic and aspect sensitive scatterers rather than specular reflections.

The most important result of the present study is the detection of these thin layers of turbulence with thickness as small as 100 m. Although the presence of such thin layers was predicted by the direct numerical simulation (DNS) studies (*Fritts et al.*, 2003), these could not be detected earlier due to the limitation of analysis techniques of rocket data, which so far had a typical detection limit of layer thickness of about 1 km. The detection of these thin layers of turbulence and their exact location is thus made for the first time in the present study using rocket-borne electron density measurements over low latitudes and was possible due to the use of wavelet transform technique for analyzing the electron density perturbations. *Strelnikov et al.* (2003) had applied the same technique to mesospheric neutral density fluctuations measured by rocket borne ionization gauges. They also found thin layers of turbulence of 100 m thickness.

Thin layers of turbulence observed by the rocket in the present study are at the edges of the main region of turbulence. These layers of stratification could be part of a system restoring to laminar flow which surround the larger regions of turbulence and hence the observed morphology. During Flight 1 the strength of the backscattered echoes, which is a measure of the turbulence, observed by the MST radar at Gadanki was strongest during 1100 to 1130 hrs LT. Later, the strength reduced, which indicates that the turbulence started to decay. The LP launched at 1142 hrs on board the rocket hence measured the electron density fluctuations during the start of the decay phase of the turbulence. The strength of the radar echo during this time was still strong enough. Hence this confirms that the observed thin layers of turbulence during Flight 1 are part of the system restoring to laminar flow. Similarly during Flight 2 the strength of the backscattered echoes is very strong at the time of launch. The thin layers of turbulence observed during this flight also are at the edges of the main region of turbulence.

During Flight 3, the presence of turbulence was observed only in the thin isolated layers (100-200 m thick) indicating that turbulence activity was much weaker on the day of launch. There were no other simultaneous measurements to be compared with; however, the results from this flight show that weak turbulence can also exist in thin layers of 100 m thickness.

The estimated energy dissipation rates, ϵ, during the three flights are shown in Fig. 3.40, along with the corresponding heating rates. During Flight 1, ϵ ranged from 10 to 100 mW/kg in lower altitudes (75 to 84.5 km) and was much higher going up to 500 mW/kg at higher altitudes (84.5 to 89 km). The corresponding heating rate ranged from 1 to 10 K/day in the lower altitudes and went up to 40 K/day at higher altitudes. The ϵ value of 23 mW/kg estimated from the radar observations at 73.5–77.5 km falls in this range and matches very well with the rocket results. The ϵ values during Flight 2 vary from 1 to 30 mW/kg and the corresponding heating rates range from 0.1 to 3 K/day. The ϵ values during Flight 3 are less than 10 mW/kg below 80 km and the heating rates are less than 1 K/day. Above 80 km the ϵ values are high and show large variability. The summer and winter high altitude profiles of ϵ from *Lübken* (1997) and the equatorial results from *Sinha* (1992) are also shown in all the three figures for comparison. The present results are grossly in good agreement with previous studies (*Royrvik and Smith*, 1984; *Lübken*, 1997; *Sasi and Vijayan*, 2001; *Lehmacher et al.*, 2006).

The high latitude summer ϵ values given by *Lübken* (1997) range from 1 to 160 mW/kg in 79 to 97 km, with a peak at around 90 km. During winter, turbulence is observed in the entire mesosphere from 60 to 100 km but ϵ values are much smaller, ranging from 1 to 20 mW/kg. The winter high latitude average also contains the results from equinox flights. In the present study turbulence was observed in the lower altitudes during summer (Flight 1) similar to that observed over low latitudes (*Rao et al.*, 2001; *Sasi and Vijayan*, 2001; *Sheth et al.*, 2006; *Kumar et al.*, 2007) and the recent observations at high latitudes (*Rapp et al.*, 2004). During summer ϵ above 80 km was high and also showed large variability. This could be a result of enhanced breaking of gravity waves, which have been detected both by the MST

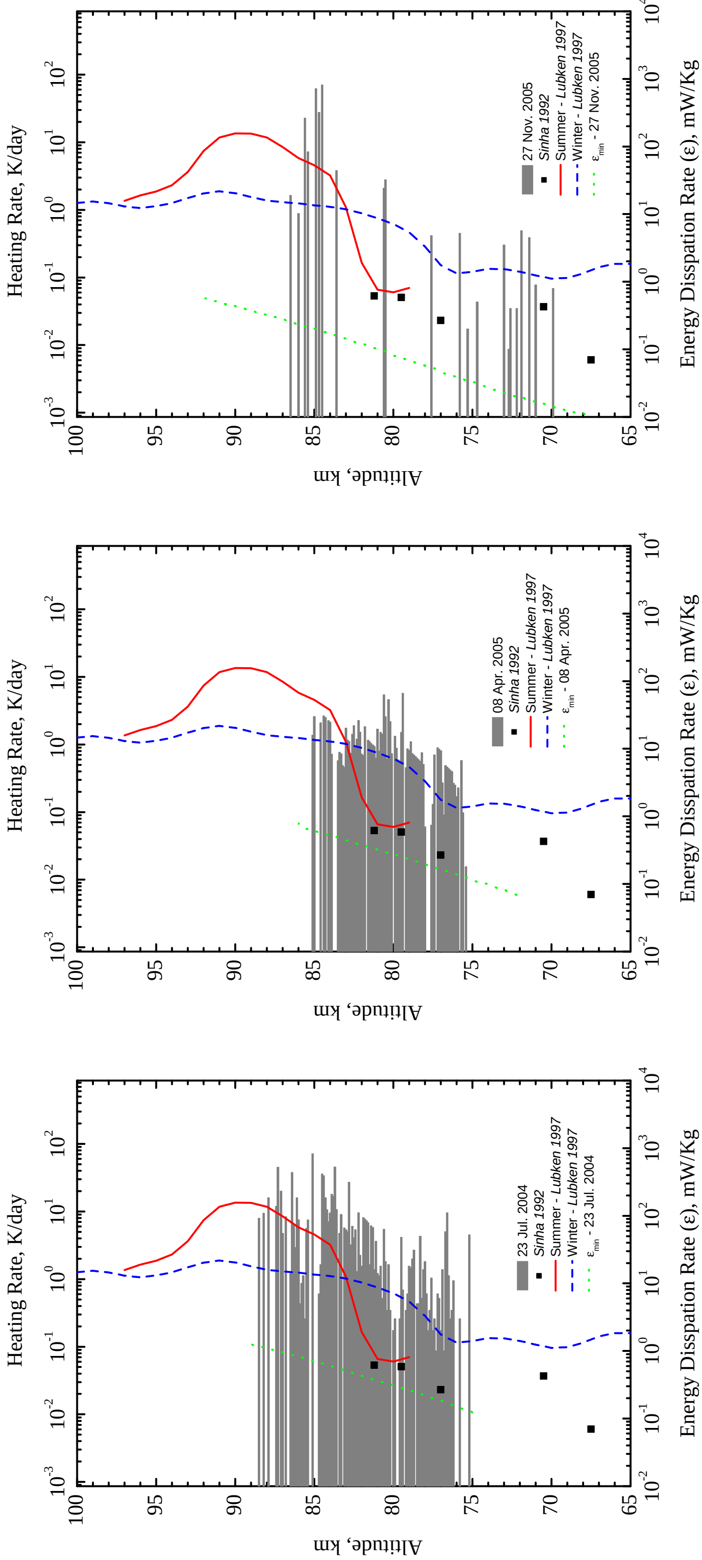

***Figure 3.40:** Estimated Energy Dissipation rates from the electron density measurements during Flights 1, 2 and 3. High latitude averages of both parameters from Lübken (1997) and equatorial results from Sinha (1992) are also shown for comparison.*

radar at Gadanki and the Chaff payloads on the day of the launch. During equinox (Flight 2) the estimated ϵ is in very good agreement with the winter high altitude average, which also contain the results from equinox flights. All the turbulence parameters during this equinox flight showed a smooth variation with altitude. The values of ϵ above 80 km were less compared to the summer flight (Fig. 3.41). These results are also in very good agreement with the value of 50 mW/kg at 86 km altitude reported over the equator at Peru by *Royrvik and Smith* (1984), using coordinated experiments of the Jicamarca radar and in situ measurements of electron density. The estimated ϵ values during the winter flight at equatorial latitudes in the present study are in good agreement with the high altitude winter average. However above 85 km, ϵ values were much higher. Plasma instabilities associated with the equatorial electrojet, such as gradient drift instability, could be affecting this altitude region, resulting in abnormally higher values of ϵ. The energy dissipation rates given by *Sinha* (1992) for the equatorial station, Thumba, seem to be underestimated, when compared to all the three flights. It should be remembered that the results by *Sinha* (1992) are from more than one flight, none of which was conducted with a view to study neutral turbulence. The present flights (Flight1 and Flight2) were conducted after ensuring with MST radar that strong turbulence present at the time of flight.

The eddy diffusion coefficients (K) computed by *Lübken* (1997) vary from 50–150 m^2s^{-1} and show little variation with season. The estimated K values in the present study (Fig. 3.41b) are also comparable with these high latitude results and exhibit the trends and variabilities as the energy dissipation rate discussed above. There is no significant difference in the profile shape of these two turbulence parameters as they are related to each other by the Brunt-Väisala frequency (ω_B) which shows no significant variation.

Rapp et al. (2004) observed turbulence below 82 km at high altitudes during the MaCWAVE/MIDAS summer program in July 2002. All ϵ values above 82 km resembled very closely the summer high latitude average given by *Lübken* (1997). However, ϵ values above 85 km were often greater than 500 mW/kg (Fig. 3.42). In

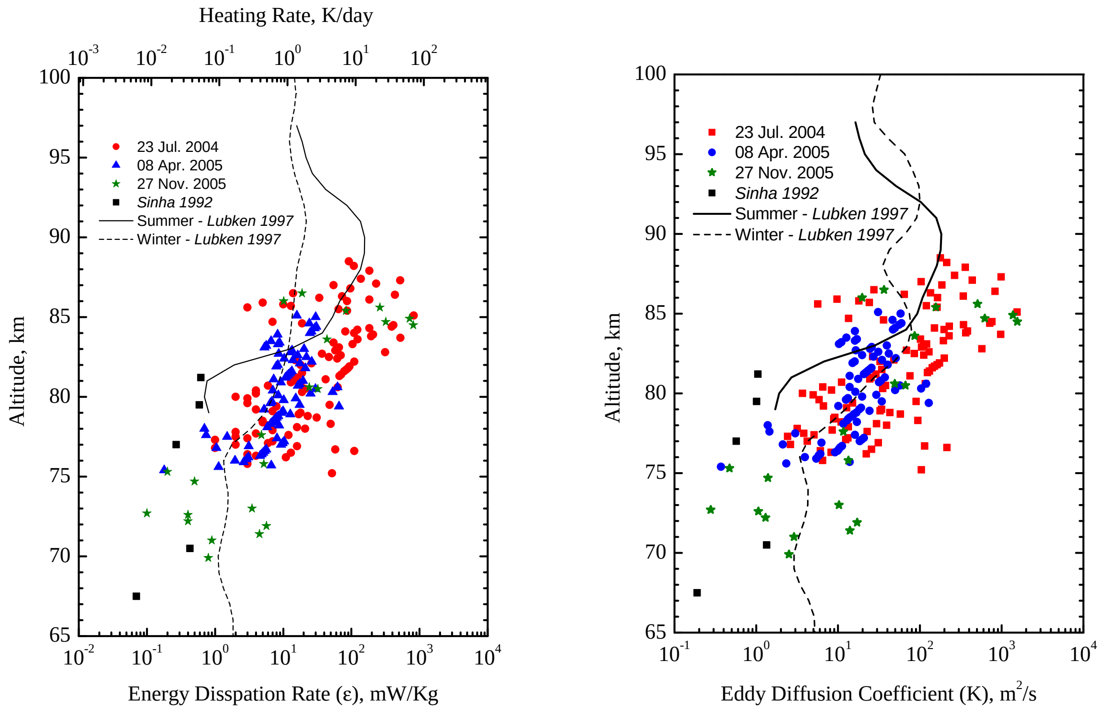

Figure 3.41: *Estimated energy dissipation rates and eddy diffusion coefficients during all the three flights. High latitude averages of both parameters from Lübken (1997) and equatorial results from Sinha (1992) are also shown for comparison.*

the present study also, the estimated ϵ values reached up to 500 mW/kg above 85 km during the summer flight over low latitudes. *Lehmacher et al.* (2006) also found a large energy dissipation rate of 170 mW/kg over an equatorial station at 90 km, where a Mesospheric Inversion Layer (MIL) was observed. Under such circumstances, enhanced wave breaking could have occurred resulting in large energy dissipation rates. There were no simultaneous temperature observations during the three rocket flights. Temperatures observed by SABER at near by locations before the launch of the rockets on 23 July 2004 at ∼1000 hrs LT are shown in Fig. 3.43 for Flight 1. Similarly Figs. 3.44 and 3.45 show the SABER temperatures on 8 April 2005 at ∼0540 hrs LT for Flight 2 and on 27 November 2005 at ∼0810 hrs LT for Flight 3, respectively. Intense gravity wave activity is observed in the profiles from 65–95 km during Flight 1. Winds measured by both the chaff payload and the MST radar during this flight also show large dynamic activity and hence the

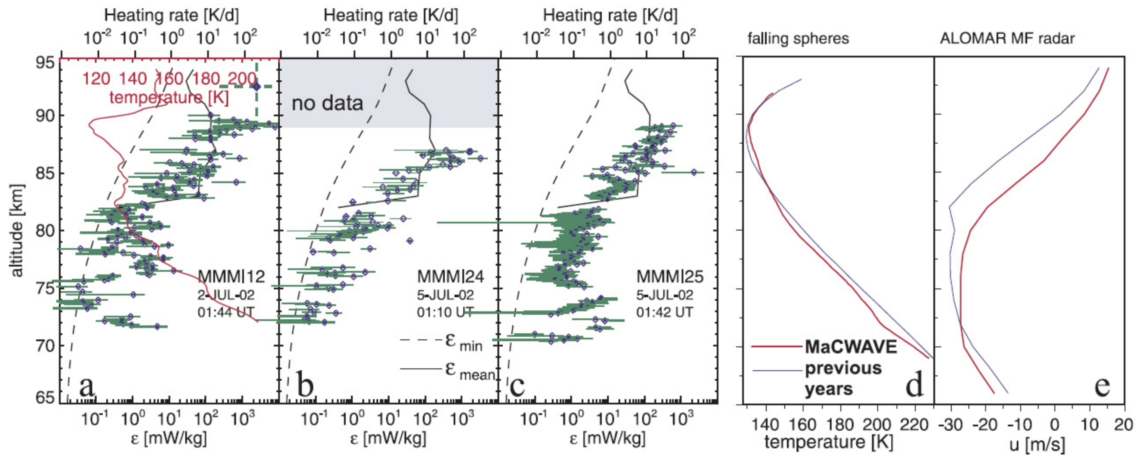

Figure 3.42: *Panel a-c: Energy dissipation rates and the corresponding heating rates during three flights of the MaCWAVE/MIDAS summer program in July 2002. Panels d and e show mean temperatures and zonal winds during the campaign. The figure is reproduced from Rapp et al. (2004).*

presence of gravity waves. The breaking of these waves thus could have caused the observed turbulence and large values of energy dissipation rate and eddy diffusion coefficients. During Flight 2 also, the SABER temperature profiles show gravity wave activity from 70 to 95 km. Chaff data was not available above 60 km for comparison during this flight. However, gravity wave breaking seems to be the cause of the observed turbulence during this flight also. During Flight 3 the gravity wave activity in the SABER profiles is much low. This supports the weak turbulence observed in Flight 3.

VHF radars at the equator and low latitudes also have studied the mesospheric turbulence. The study of mesospheric turbulence by *Sasi and Vijayan* (2001) using the MST radar at Gadanki showed that the energy dissipation rate peaks in summer months from June to September and varies from 7 to 100 mW/kg from the lower altitudes at 65 km to mesopause altitudes at 90-95 km (Fig. 3.46). During this period the energy dissipation rates remain high throughout the 65-95 km height region when compared to those values during other months. Similarly, the eddy diffusion coefficient, K, varies in the range of 25-300 m^2s^{-1} and is similar to the variation of K in the present study from 3-1000 m^2s^{-1} in the altitude region from

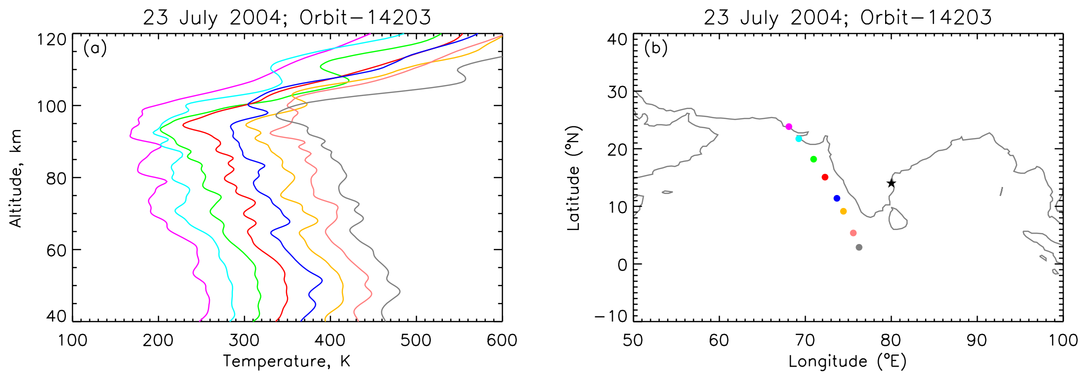

Figure 3.43: *(a) Temperature observed by SABER on 23 July 2004 along the orbit 14203 at ∼1000 hrs LT. Each profile is shifted by 30 K for proper visualization and the color of the profile corresponds to the location shown by the same color in figure (b).*

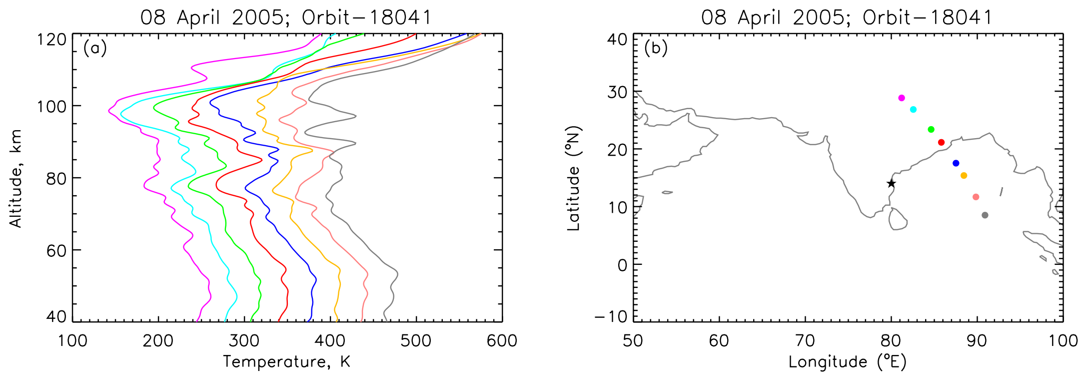

Figure 3.44: *(a) Temperature observed by SABER on 8 April 2005 along the orbit 18041 at ∼0540 hrs LT. Each profile is shifted by 30 K for proper visualization and the color of the profile corresponds to the location shown by the same color in figure (b).*

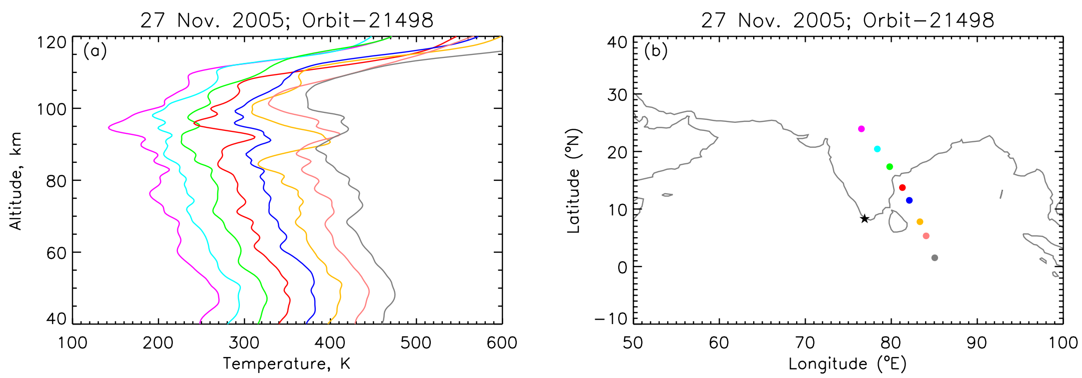

Figure 3.45: *(a) Temperature observed by SABER on 27 November 2005 along the orbit 21498 at ∼0810 hrs LT. Each profile is shifted by 30 K for proper visualization and the color of the profile corresponds to the location shown by the same color in figure (b).*

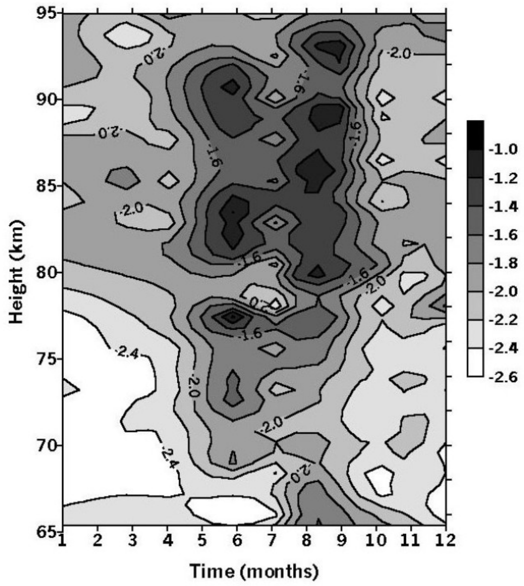

Figure 3.46: *Seasonal variation of energy dissipation rate in the mesosphere over Gadanki. This figure is reproduced from (Sasi and Vijayan, 2001).*

75 to 89 km. The values are larger at the higher altitudes, as observed in the energy dissipation rates. The energy dissipation rate over Gadanki during April increases with altitude from 65 km, reaches a maximum in the altitude region from 80 to 88 km and decreases above 88 km (*Sasi and Vijayan*, 2001). The energy dissipation rate values were in the range of 2-20 mW/kg and the eddy diffusivity values were in the range of 10-40 m^2s^{-1}. The present results of the April flight (Flight 2) match quiet well with these numbers. *Sasi and Vijayan* (2001) also analyzed the M100 rocket data of wind and temperature from 1978 to 1986 at Trivandrum (8.5°N, 77°E) in order to see any corresponding seasonal variation in mesospheric gravity wave activity. Both parameters showed a minimum during winter solstice and maxima during the equinoxes. A secondary maximum was observed during the summer.

A study using a Microwave Limb Sounder (MLS) onboard the Upper Atmosphere Research Satellite (UARS) by *McLandress et al.* (2000) showed that during the northern hemispheric summer (June to August), gravity wave activity at the 38 km level has a maximum lying on and near the Indian subcontinent. *McLandress* *et al.* (2000) also show that wave activity maxima are correlated with, to a large degree, with the satellite measurements of outgoing longwave radiation, indicating that deep convection is the source of these waves. Studies mentioned above show that stratospheric gravity wave activity at low latitudes is maximizing during the wet season, implying tropical convection as the source of these waves. This could result in a similar seasonal variation in the mesospheric gravity wave activity with a summer peak. *Sasi and Vijayan* (2001) suggested that the observed turbulent energy dissipation rate and the vertical eddy diffusion coefficient in the mesosphere over Gadanki is related to the enhanced gravity wave activity over the low latitude Indian subcontinent during the summer monsoon season (June to September). The present study also supports this view where high energy dissipation rates and eddy diffusion coefficients have been observed.

Fukao et al. (1994); *Kurosaki et al.* (1996) studied the seasonal variation of vertical eddy diffusivity in the troposphere, lower stratosphere and mesosphere using data (1986 to 1988) from MU radar at Shigaraki, Japan (35°N, 136°E). In the mesosphere a summer maximum in K was found and a similar summer maximum was found in the gravity wave activity observed by the MU radar. They suggested that the middle atmospheric turbulence is mainly induced by breaking of gravity waves. *Rao et al.* (2001) also studied the seasonal variation of vertical eddy diffusivity in the troposphere, lower stratosphere and mesosphere over Gadanki. The value of K in the mesosphere increased with height up to 75 km and again decreased above that height. The maximum values were seen during the summer, followed by equinoxes and a minimum during the winter. The percentage occurrence of temperature inversions show a maximum during the summer and a minimum during the winter season *Ratnam et al.* (2002) and match well with the occurrence of the maximum and minimum values of eddy diffusion coefficient. *Rao et al.* (2001) also concluded that the summer maximum in the mesospheric eddy diffusivity is due to the breaking of gravity waves.

Anisotropic Turbulence

The layer of turbulence seen by the radar on 23 July 2004 during the Flight 1 was only from 73.5–77.5 km, although the rocket observed layers of turbulence much above this altitude. The two instruments have probed a different part of the atmosphere over Gadanki and Sriharikota, separated horizontally by $>$100 km and the direction of the rocket trajectory also is in the opposite direction, owing to geographical constraints. If the turbulence observed was anisotropic then it is possible that turbulence was present in the region which the rocket traversed and the radar could not see the turbulent volume. Fig. 3.25 shows that there was anisotropy to a certain extent, as the strength of the echoes observed in all beams is not same. The North and the West beams showed stronger echoes, followed by the zenith beam. The South and the East beams showed weaker echoes. The Doppler spectra shown in Fig. 3.30 also show anisotropic nature; the spectra are broader in the East-West direction when compared to zenith and North-South directions. While the broadness shows that the backscattered echoes observed by the radar are due to turbulent scatterers, a difference in the broadness of the Doppler spectra in the different directions indicates that the turbulence was anisotropic (*Sheth et al.*, 2006). In the study by *Rao et al.* (2001) also, a comparison of Doppler spectral parameters in different beam directions showed anisotropy in both SNR maps and spectral widths in the mesosphere.

To further investigate the issue of anisotropy the gradient in the energy dissipation rate has been computed and is shown in Fig. 3.47. Gradients over 500 m were calculated in those altitude regions where the thickness of the turbulent layer was greater than 500 m. It can be seen that there are moderate gradients at 76 and 83 km, which are the edges of the main turbulent layers. Larger gradients are seen from 84 to 89 km. Studies by the Jicamarca radar (*Sheth et al.*, 2006) show that layer edges are dominated by anisotropic turbulence. Direct numerical simulation (DNS) studies predict that at the layer edges the gradients in the turbulent parameters are large (*Fritts et al.*, 2003). This is due to the efficient mixing within the turbulent layer. Hence the gradients in energy dissipation rate that are present at 76 and 83 km in the present study show that the layer edges are anisotropic. In the region from 84 to 87 km, the gradients are very large which show that the degree of anisotropy in this altitude region is very high. This could be one of the reasons why the MST radar could not detect any echoing layers at the same altitude over Gadanki. The calculation of such gradients was possible only by the use of the continuous wavelet transform, which otherwise would have been smeared out if the traditional methods like Fourier analysis had been used.

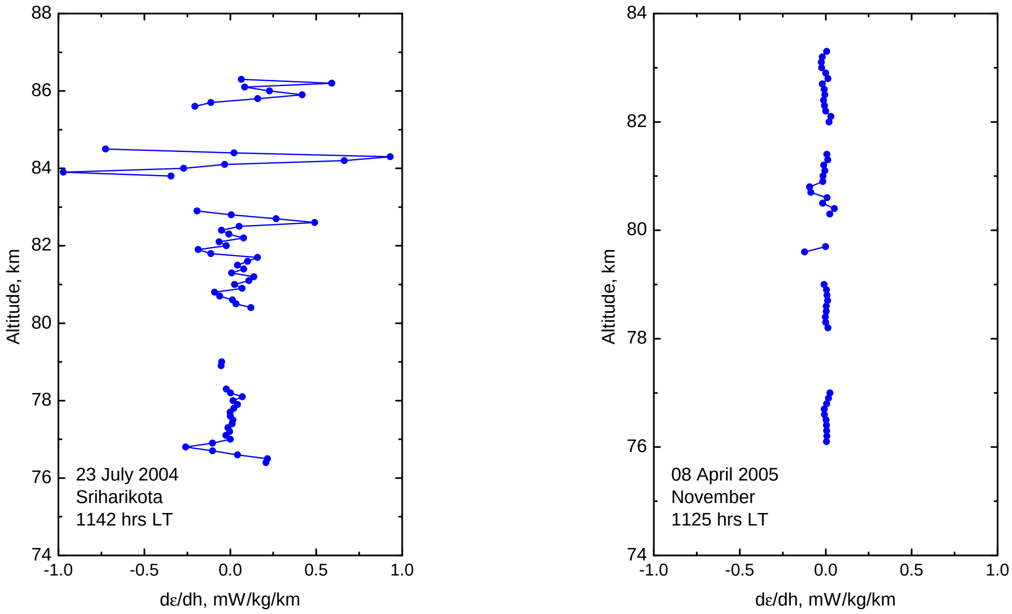

Figure 3.47: *Altitude variation of energy dissipation rate gradient during Flights 1 and 2.*

On 8 April 2005, the day of launch of Flight 2, the MST radar at Gadanki observed two strong layers. The rocket detected only the upper layer where turbulent parameters could be estimated. In the lower region also the power spectra showed the characteristic -5/3 slope, but the turbulence parameters could not be computed as the inner scale at this altitude was very small and was beyond the detection limit of the rocket payload. Even in the upper layer, the rocket detected turbulence from 75 to 85 km (there was no data beyond 85 km to mention about the turbulence above 85 km), where as the radar saw an echoing layer from 75 to

80 km only. There is no evidence of anisotropy as the echoes in all the beams of the radar look similar. Also there are no gradients in the estimated energy dissipation rates (Fig. 3.47), which again show that there is no anisotropy at the layer edges as proposed by *Fritts et al.* (2003). The only other explanation for such a discrepancy is that the strength of the turbulence at 3 m was very low above 80 km because of which the radar could not detect it. Hence it is conclude that the turbulence observed on 8 April 2005 by both the radar and the rocket was isotropic in nature.

Another reason for the discrepancy between the altitudes at which turbulence is observed is as follows. The radar can look at the 3 m irregularities only, whereas the rocket can measure a wide range of scale sizes. And as the inner scale increases with altitude, the 3 m scalesize falls more and more far into the viscous dissipation regime, and hence the radar could probably not detect the signal of such low power.

Possible Effect of Geomagnetic storm

The day of launch of Flight 1 was a geomagnetically disturbed day with $Ap = 52$ (Sec. 3.2). The storm was very intense and one can contemplate that the storm could also have had an effect on the observed turbulence. The effects of a geomagnetic storm in the F region of the ionosphere are generally strongest in the auroral zone, their amplitude weakens toward middle latitudes, some of them disappear at low latitudes, but some of them reappear or strengthen near the geomagnetic equator. However, the low-latitude boundary of a geomagnetic storm effects on the lower ionosphere (altitude < 100 km) is $\sim$ 35-37°N (geomagnetic coordinates) (*Danilov and Lastovicka*, 2001). Though, high turbulence is observed in the upper mesosphere during this flight, there is no proof that the geomagnetic storm had caused any disturbance. The question whether the storm has an effect on the low latitude mesosphere is left open. This can be answered from more studies on the coupling between the various regions of the atmosphere in altitude and latitude.

Effect of Electrojet Instabilities

During Flight 3, the winter flight over the equatorial station Thumba, the energy dissipation rates above 87 km were unusually high and were in the range of 10-100 W/kg. Such high ϵ are not physically possible and indicate that they are not produced by neutral turbulence mechanism. These values are hence not plotted in Fig 3.40c. The E-region ledge typical of the equatorial ionosphere is present from 87 to 90 km (Fig. 3.3). Strong positive electron density gradients are therefore observed between 87 and 90 km (Fig. 3.4). The percentage amplitude of the electron density irregularities in this region of the E-region ledge and above from 87 to 95 km is also very high for all scalesizes (Fig 3.20). In view of the special geometry over Thumba, which is located on the geomagnetic equator, plasma instabilities such as cross-field and two stream instability are other sources which can give rise to the observed irregularities *Sinha* (e.g., 1976)) other than neutral turbulence. *Goldberg et al.* (1997) and *Lehmacher et al.* (1997) also reported such high energy dissipation rates above 90 km over the equator during the CADRE/MALTED campaign. *Lehmacher et al.* (1997) suggest that the electron density fluctuations are a result of the instabilities in the electrojet region. In the present study also, it is plausible that the electrojet instabilities could be affecting the observed electron density fluctuations not only in the ledge region but below it also. This could have resulted in the comparatively high energy dissipation rates in the region from 85 to 87 km. Also around 100 km, the spectral index of the small scale irregularities (1-15 m scalesize) was near zero. Such flat spectra are typical characteristics of the two stream instability, which has been observed earlier at these altitudes (e.g., *Sinha*, 1976).

It is observed that turbulence can exist in layers and the thickness can be as small as 100 m. The observed turbulence during the three rocket flights is thought to be due to gravity wave breaking. Observations by Chaff payload, the MST radar and SABER temperatures support this argument. Enhanced turbulence is seen during summer, followed by equinox and the turbulence becomes weak in winter. Anisotropic turbulence is observed during the summer flight, whereas the equinox flight did not show any anisotropy. The use of the continuous wavelet transform made it possible to compute the turbulence parameters with better altitude resolution and hence the calculation of their gradients. The values of the turbulence parameters are in good agreement with the earlier studies using rockets and radars. No effect of geomagnetic storm on mesospheric turbulence over low latitudes is seen. Over the equator, in addition to the neutral turbulence, there is a considerable effect of plasma instabilities in the higher altitudes (above about 80 km) and decoupling the effect of these two processes is difficult. The differences between the results obtained by the rocket and the radar may be due to both localized/sporadic wave breaking and their lifetime.

CHAPTER 4

Results from Mesospheric Airglow Study

The motivation of the present study was to look for those features of 557.7 nm nightglow over mid-latitudes which were detected in satellite observations but some how evaded detection in the analysis of integrated ground data. It is with this view that a 16 year long data set of the intensities of atomic oxygen green line emission at 557.7 nm over a mid-latitude station Kiso (35.79°N, 137.63°E) is reanalyzed using the continuous wavelet transform to understand the long term variations and the inter-annual variabilities.

The data set of green line emission intensity spans approximately one and half solar cycle, with the decreasing half of cycle 21, starting from the peak in 1979 and ending in 1986, and most of cycle 22 up to 1994. Solar cycle 22 ended in April 1996. This time period of 16 years has two sunspot maximum years, *viz.,* 1979 and 1989, and one sunspot minimum year, 1986. Fig. 4.1 shows the monthly mean nocturnal variation of the green line emission observed over Kiso during the period 1979-1994. During the solar cycle 21, high emission is seen during 1979-1984, *i.e.,* from solar maximum year of 1979 and subsequent decreasing phase of the solar activity up to 1984. During the next solar cycle high emission is seen during

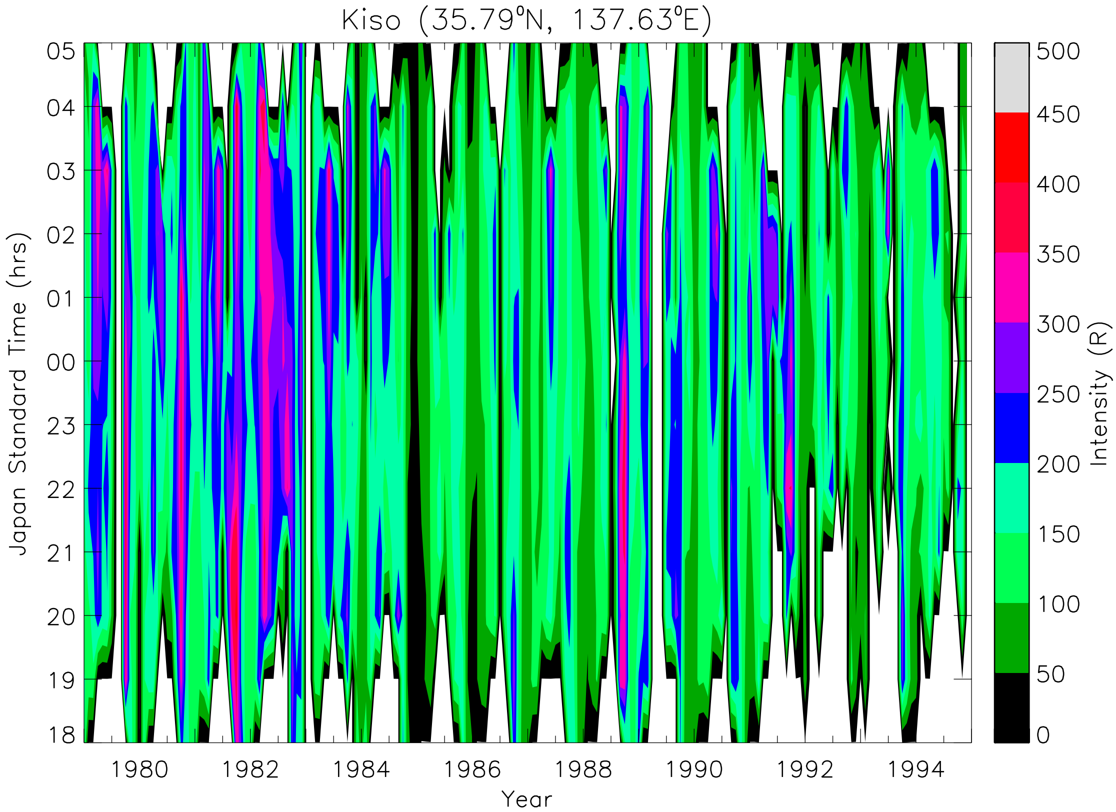

Figure 4.1: *Monthly averaged 557.7 nm integrated intensity at each hour between 1800 and 0500 hrs JST observed over Kiso during 1979-1994.*

1987–1992, which corresponds to the increasing phase of the solar activity to the just start of the decreasing phase. Minimum emission is seen around 1986, which is the sunspot minimum year. Thus the phase relationship between the emission maximum and solar activity is different in solar cycle 21 and 22, as observed by *Deutsch and Hernandez* (2003) for Kiso data.

The scalograms or the wavelet plots for the data series from 2000 to 0300 hrs JST are given in Figs. 4.2 to 4.9 and for the mean night intensity in Fig. 4.10. Figs. 4.2 to 4.10 contain three panels each. The lower panel is the time series of the monthly average (with one sigma variations) of the 557.7 nm intensity, which is used to compute the wavelet power spectrum. The black circles represent the observations and the red circles are the interpolated points. The top panel gives the wavelet plot of the data and the thick solid line is the cone of influence (COI) of the scalogram. Wavelet coefficients outside this cone are subject to edge effects and are not completely reliable. Wavelet powers with confidence levels of 95% and 90% are shown by continuous and dotted contours, respectively. The plot on the right is the global power spectrum obtained by averaging the wavelet power over the entire duration, *i.e.,* during 1979-1994. The solid and dotted lines show 95% and 90% confidence levels, respectively. The intensity of semi-annual, annual and quasi-biennial components, during different epochs, can be seen clearly in the central wavelet plot. This information is lost in the global power spectrum as well as in the case when Fourier, maximum entropy or other transforms are used.

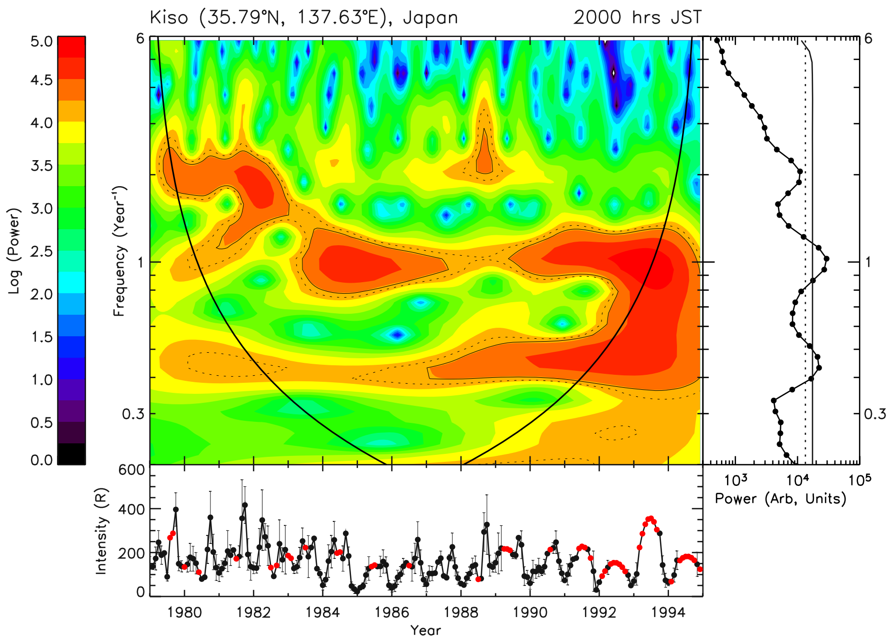

Figure 4.2: *The wavelet plot of 557.7 nm integrated emission at 2000 hrs JST. The thick solid line is the COI. Wavelet powers with confidence levels above* 95% *and* 90% *are continuous and dotted contours, respectively. The lower horizontal panel is the time series of the monthly average (with one sigma variations) used to compute the wavelet power spectrum. The black circles are base on the observations and the red circles are the interpolated points. The plot on the right is the global power spectrum of the entire epoch, 1979-1994, with* 95% *and* 90% *confidence levels shown as continuous and dotted lines.*

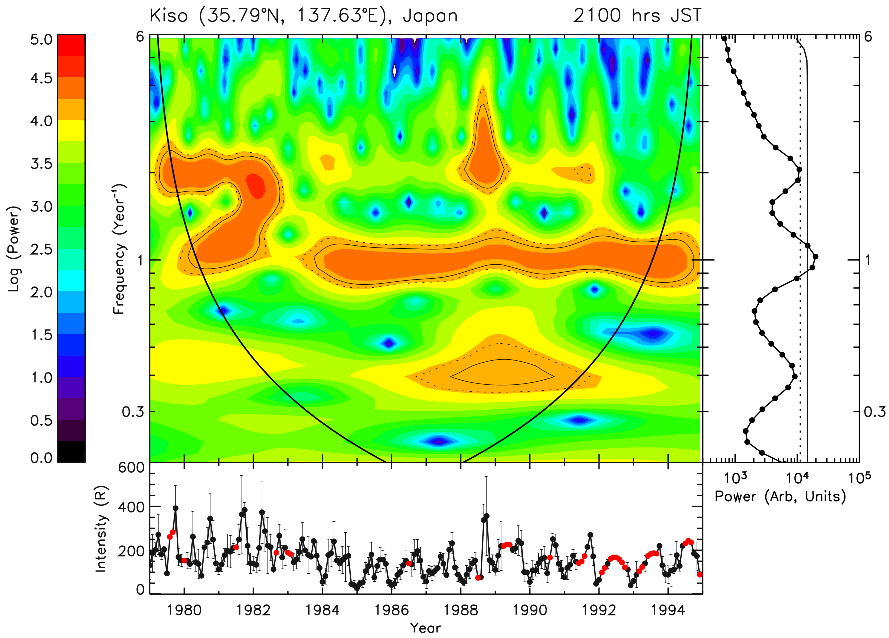

Figure 4.3: Same as Fig. 4.2 at 2100 hrs JST.

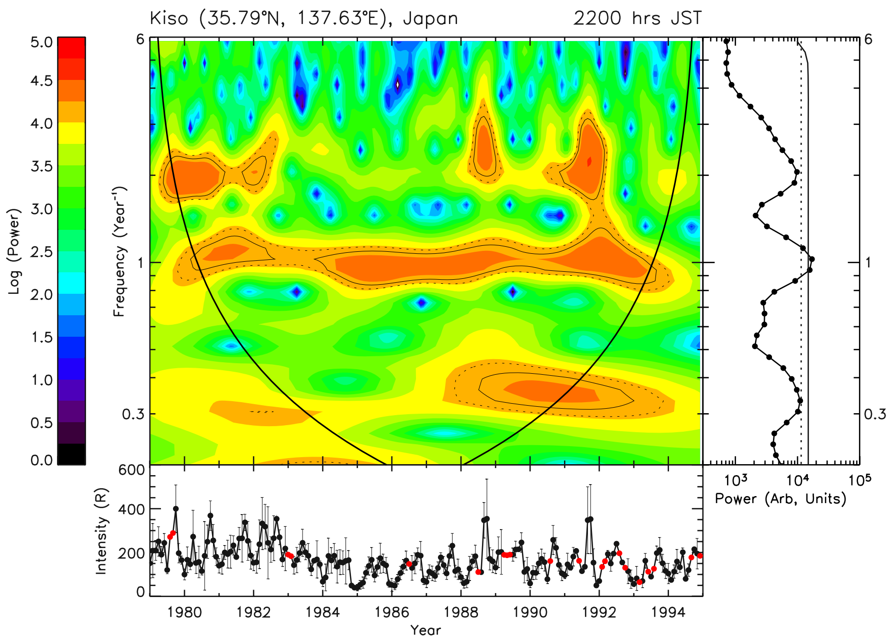

Figure 4.4: Same as Fig. 4.2 at 2200 hrs JST.

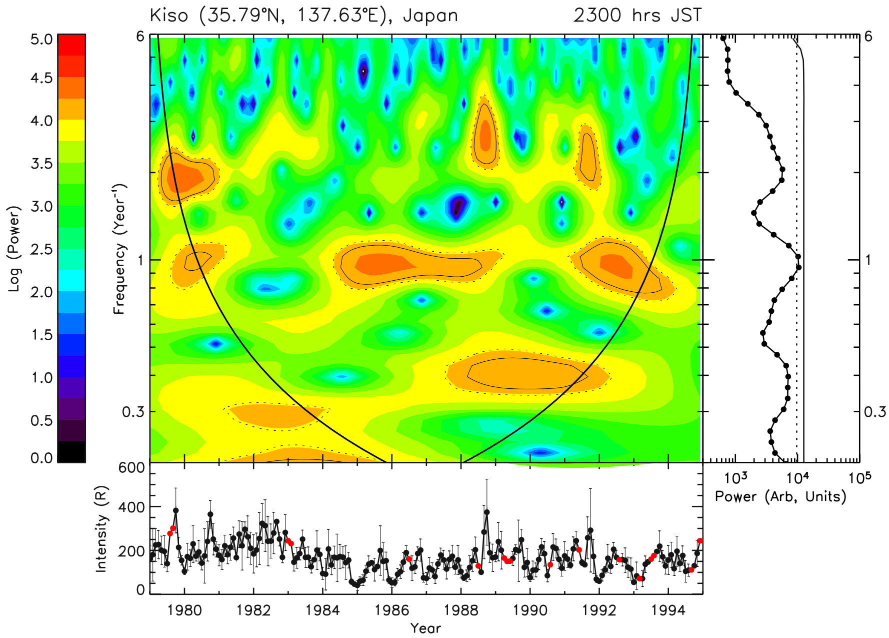

Figure 4.5: *Same as Fig. 4.2 at 2300 hrs JST.*

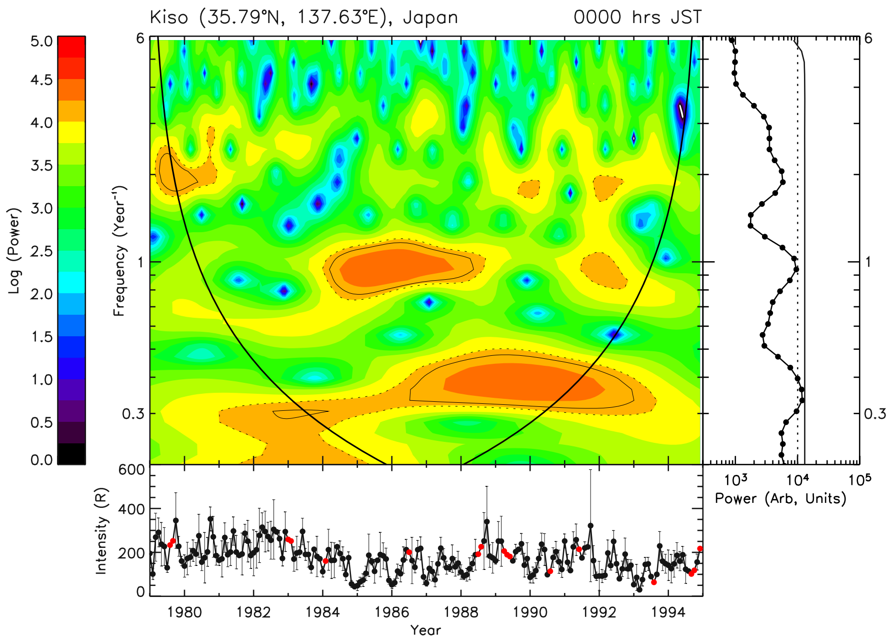

Figure 4.6: *Same as Fig. 4.2 at 0000 hrs JST.*

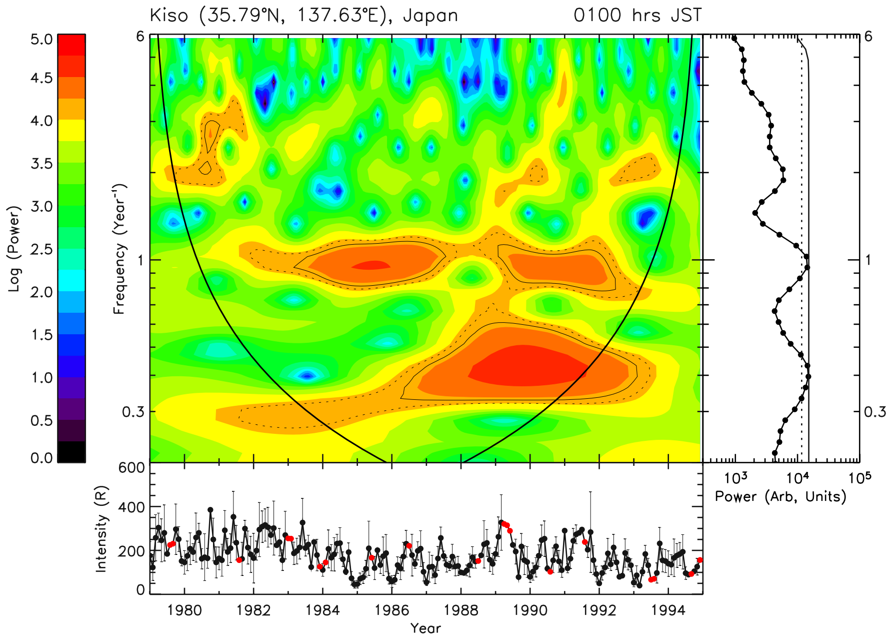

Figure 4.7: *Same as Fig. 4.2 at 0100 hrs JST.*

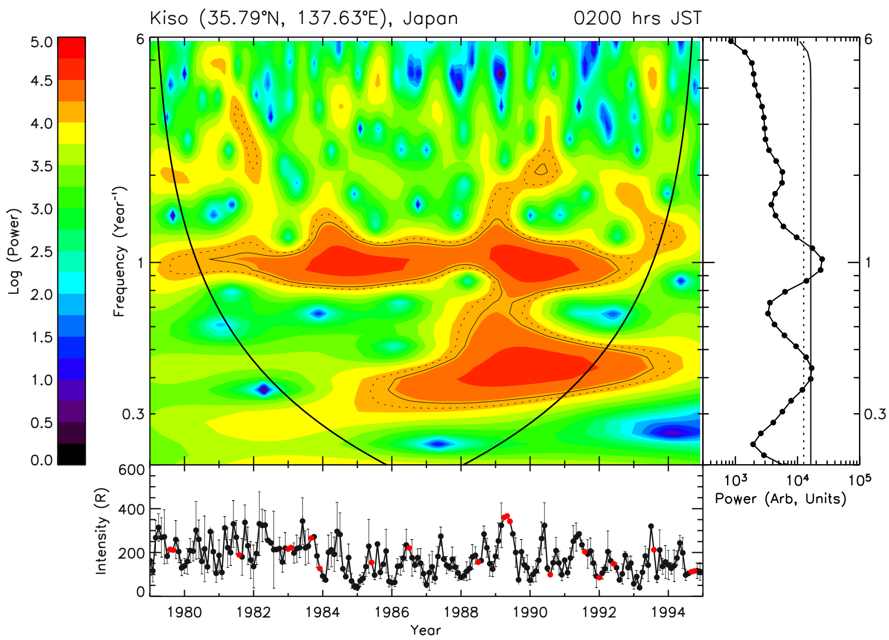

Figure 4.8: *Same as Fig. 4.2 at 0200 hrs JST.*

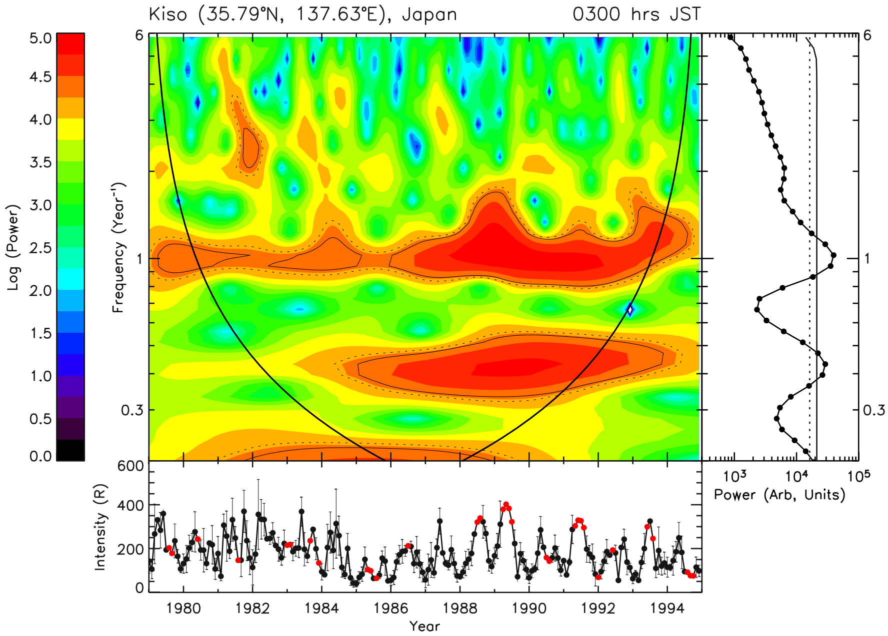

Figure 4.9: *Same as Fig. 4.2 at 0300 hrs JST.*

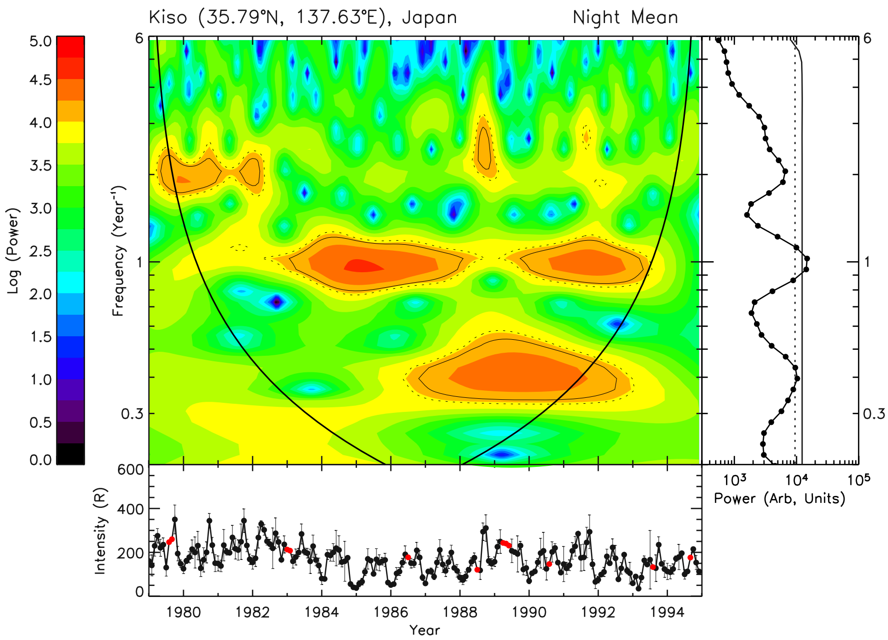

Figure 4.10: *Same as Fig. 4.2 for the night mean intensities.*

4.1 Semi-Annual Component of 557.7 nm

It can be seen from Fig. 4.2 that there is a strong semi-annual component during 1979-1982 at 2000 hrs JST, and a slightly weaker one from 1988-1991. The semi-annual component reduces in amplitude and becomes weaker as the night progresses, as is evident from the wavelet plots for 2100 to 0300 hrs (Figs. 4.3 to 4.9). After midnight, the semi-annual component practically disappears. Wavelet analysis also shows that during 1979-1982, the semi-annual oscillation dominated over the annual component at 2000 hrs and after 1982, the annual oscillation became more prominent. Fig. 4.10 shows the wavelet power spectrum calculated from the mean intensities averaged over the entire night. During the period from 1979-1982 the semi-annual component is dominant and the annual component is not significant. A time averaged wavelet power spectrum during this period from 1979 to 1982 will show a significant semi-annual peak and a statistically insignificant annual peak. This feature obtained here by using the nightly mean intensities, is in agreement with the findings of *Deutsch and Hernandez* (2003). If data from 1979 to 1982 was only available, then one would have arrived at the conclusion that the semi-annual oscillation was more prominent over Kiso. With the increase of the size of the data set, for the climatological study, the annual oscillation became more pronounced (Fig. 1.5). The wavelet power spectrum when averaged over the entire duration from 1979-1994 giving the global power spectrum also shows the same result (Fig. 4.10).

Shepherd et al. (2005) found well-defined semi-annual variations at mid-latitudes through both WINDII satellite measurements and TIME-GCM model results of the green line emission at 2000 hrs LT at 96 km, which weakened by midnight and disappeared by 0200 hrs LT. However, nightly averaged ground based observations detected only an annual variation but not a semi-annual variation. The wavelet plot (Fig. 4.2) of the ground based photometer data over Kiso, a mid latitude station, presented here shows clearly the presence of a semi-annual component in the nightglow variation at 2000 hrs JST, though only during certain epochs, from

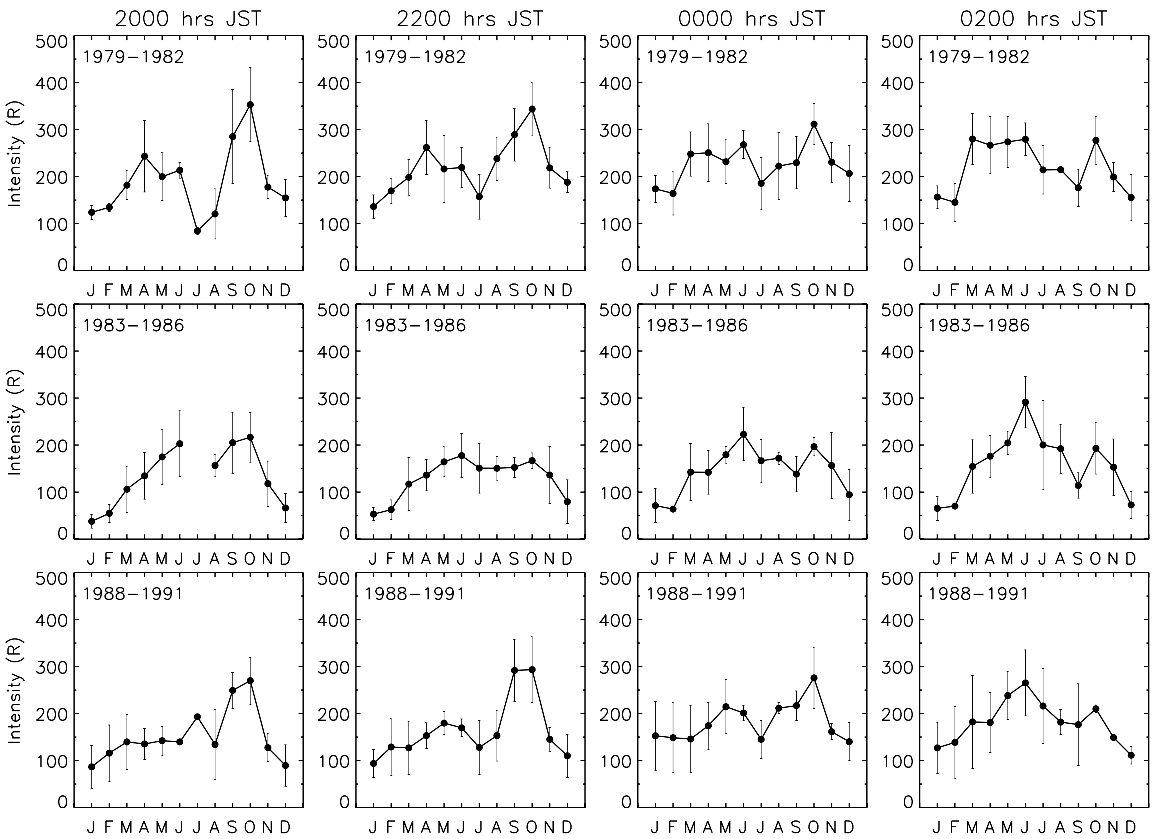

Figure 4.11: *Monthly averages of 557.7 nm integrated emission for the epochs 1979-1982 (top row), 1983-1986 (middle row) and 1988-1991 (bottom row) at 2000, 2200, 0000 and 0200 hrs JST, over Kiso (35.79°N, 137.63°E).*

1979-1982 and from 1988-1991, similar to what was observed by WINDII and then gradually disappears by 0200 hrs. To ascertain this point monthly averages at 2000, 2200, 0000 and 0200 hrs for these two epochs (top and bottom rows) and for the epoch 1983-1986 (middle row) are shown in Fig. 4.11. The results for these four times are discussed hereafter, as they represent the complete nocturnal evolution of the observed intensities. The autumnal peak in October is prominent at all times. The semi-annual component is seen very clearly during 1979-1982 (top row) with peaks in April and October, and it gradually decreases in strength as the night progresses, similar to what was observed in WINDII measurements and TIME-GCM predictions (*Shepherd et al.*, 2005). During 1988-1991 (bottom row), the semi-annual variation is observable, though not as a very strong variation, because it is superimposed on a more stronger annual variation. Unlike the period 1979-1982, the semi-annual component during 1988-1991 is strongest at 2200 hrs with two clear peaks in May and October and then as the night progresses it gradually weakens and gives way to the annual variation peaking in June by 0200 hrs. During the period 1983-1986 (middle row) the semi-annual component is not seen but the annual variation is prominent with a summer maximum and a winter minimum.

Fig. 4.12(a) gives the variation in percentage amplitude of the semi-annual component at 2000, 2200, 0000 and 0200 hrs for each month during 1979-1994. The percentage amplitude calculated from the nightly mean intensities is also shown. The continuous (dotted) lines in all three subplots are the statistically significant (insignificant) amplitudes, with confidence levels greater (less) than 95%. Variation of more than 8% is seen at 2000 hrs during 1979-1982 with a maximum amplitude of 11% during 1980 and it reduces as the night progresses. By 0200 hrs the amplitude is no longer statistically significant. This supports very clearly, the domination of the semi-annual component during different epochs. The percentage amplitude during the period 1988-1991 is statistically significant only during certain epochs but not through out as observed during the period 1979-1982. On an average, the amplitude is strong during 1988-1991 at 2200 hrs with maximum amplitude of more than 10%. As the night progressed the amplitude of the semi-annual component reduced, except for the year 1990, during which its amplitude peaked at 0200 hrs and was more than 8%. The percentage amplitudes of the semi-annual component obtained over Kiso using wavelet analysis are similar to the values (10% to 13%) obtained using maximum entropy method and periodic analysis for four mid latitude stations (36°N to 38°N) by *Fukuyama* (1977) for the period 1958-1969.

The profound local time dependence of the semi-annual variation shows that the pattern is of tidal origin. *Shepherd et al.* (1998) showed that over mid-latitudes during equinox the diurnal tide dominates the airglow emission and during solstice the diurnal tide does not penetrate to as a high an altitude to influence the

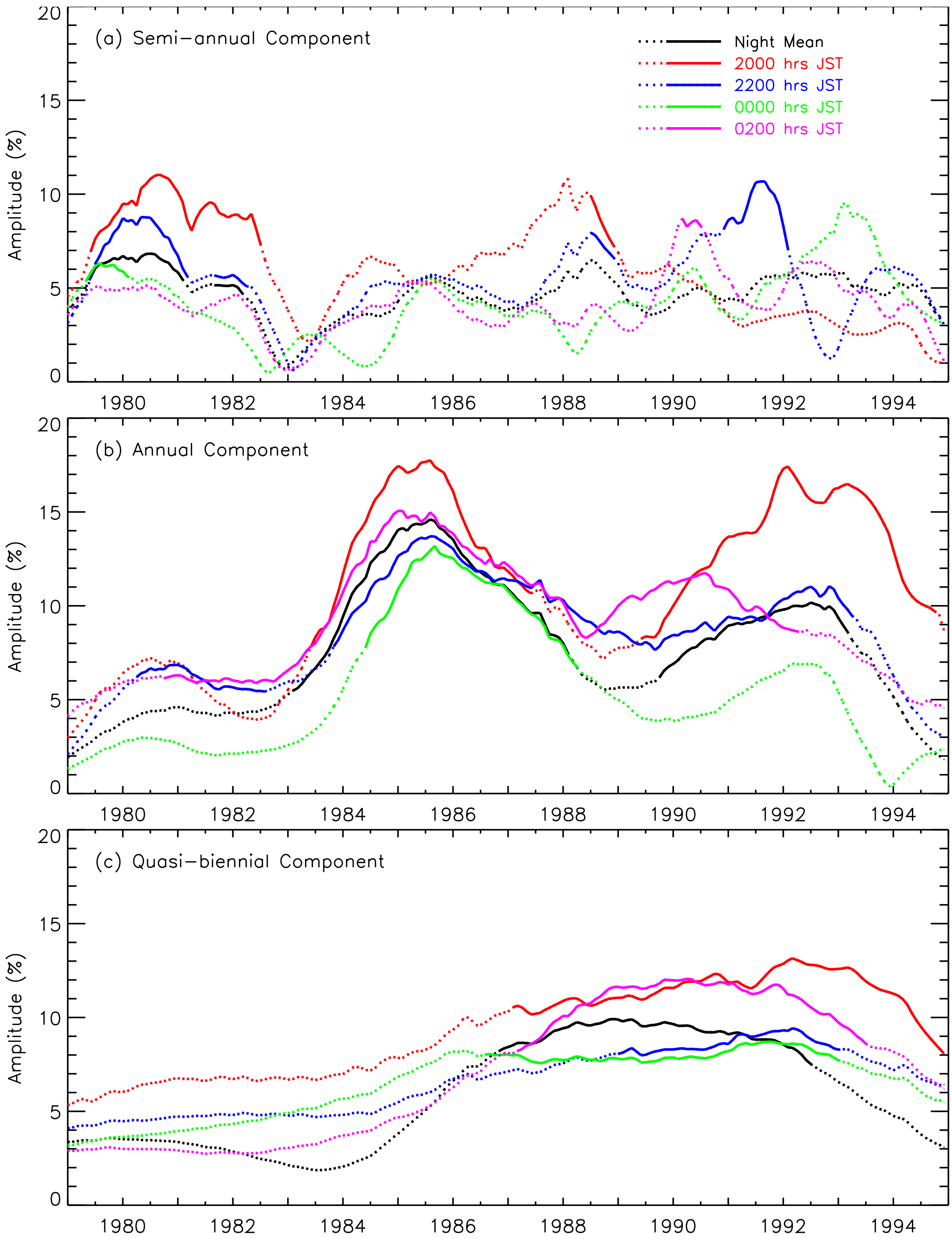

Figure 4.12: *The percentage amplitudes of the (a) semi-annual, (b) annual and (c) quasi-biennial components computed at different times of the night and also for the entire night as derived from the wavelet power spectra. The continuous lines are above 95% confidence level and dotted lines are below 95% confidence level.*

airglow emission and the in-situ semi-diurnal tide dominates during this period. Hence it is concluded from the present study also that the semi-annual variation observed with maxima during the equinoxes, i.e., April and October, is due to the upward propagating diurnal tide.

From the wavelet plot at 2000 hrs (Fig. 4.2) one can see that the contribution of the semi-annual component is not constant throughout and hence the total power in the global power spectrum is reduced, which results in a peak which is not statistically significant. The periods 1979-1982 and 1988-1991, when the semi-annual component is present, are during the decreasing phase of the solar activity and around the peak of the particular solar cycle, respectively. This is similar to the observed difference in increased intensities during the decreasing phase of solar activity of different solar cycles (*Deutsch and Hernandez*, 2003). The relation between the solar cycle and the semi-annual variation of the green line emission is, however, not clearly understood. Since this semi-annual variation is attributed to the semi-annual variation in the diurnal tide (*Fukuyama*, 1977), it is interesting to conclude that the diurnal tide also has a long term variation of approximately 12 years, spanning a solar cycle, but longer data sets are needed to confirm this.

The present study shows that the semi-annual oscillation is not present during every year and a model like that of *Garcia and Solomon* (1985) will thus fail during those epochs when the semi-annual oscillation is absent. Models should therefore consider the inter-annual variabilities of these long term variations to achieve better consistency with observations. Also, *Garcia and Solomon* (1985) did not include the diurnal variabilities caused due to the tides as the variations in the green line intensity was 10-30 %, which was small when compared to the seasonal and latitudinal changes of 100-200 %. However, the present study shows that the tidal variabilities are also important as the long term variations change appreciably with time. These tidal effects also should therefore be included in the models to achieve better consistency with observations.

4.2 Annual Component of 557.7 nm

A strong annual component is observed over Kiso in all the wavelet plots (Figs. 4.2 to 4.9). At 2000 hrs the annual component is significant during the epoch 1983-1994. As the night progresses the annual component weakens up to midnight, where the power levels associated are significant during 1984-1988. After midnight, the amplitude of the annual component increases again in strength and by 0200 hrs and thereafter becomes a very strong feature for the entire epoch. In the global power spectra, the annual component is above the confidence level at all times, except at midnight, when it just touches the same. The wavelet plot of nightly mean intensities (Fig. 4.10) also shows that the annual variation is statistical significant during 1982-1992. The global power spectrum of the nightly averaged data shows that the annual variation is statistical significant, which is in agreement with the results obtained by *Deutsch and Hernandez* (2003). These results are also in conformity with studies using ground based photometric data at other stations (*Fukuyama*, 1977) and studies using satellite data (*Shepherd et al.*, 2005).

Fig. 4.12(b) gives the variation in the percentage amplitude of the annual component at 2000, 2200, 0000 and 0200 hrs and for the night mean intensities for each month during 1979-1994. The percentage amplitude is highest at 2000 hrs, decreases till midnight and then starts increasing again at 0200 hrs. The amplitude is not constant and varies from 6 to 18%, clearly showing an inter-annual variation. *Fukuyama* (1977) also obtained similar amplitudes (8% to 18%) for other mid latitude stations, near Kiso, using the Maximum Entropy Method. During 1979-1982, the amplitude of the annual component is small, $\sim$ 6%, when compared to the remaining part of the data set and is also not statistically significant as the semi-annual component. Hence, as explained earlier, the semi-annual component dominates and can be seen very clearly in the original data, which is plotted in the top row of Fig. 4.11. However, during 1988-1991, there is also a strong annual component over which the semi-annual component is superimposed. Hence the semi-annual component is not observed as a strong feature in the original data, which is shown in the bottom row of Fig. 4.11.

The local time dependence seen in the annual variation also shows that the pattern is of tidal origin. However it is not understood why the amplitude of the variation is showing a minimum at midnight. This variation is also not significant at all epochs which shows that the tides also show a different annual variation in different years. Satellite studies, which can address the variability of tides on a global scale, have looked into the seasonal variation only (*Shepherd et al.*, 1998). It should also be remembered that while using satellite data for long term variations, the zonal averaging of the winds and temperature smears out the tidal effects. And with the airglow data alone, it is difficult to arrive at a possible conclusion regarding the inter annual variation of tides and also their variation with time of the night. More long term measurements and studies, both ground and satellite based, in order to understand the tidal variations may probably be able to explain these observed variations.

4.3 Quasi-Biennial Component of 557.7 nm

The wavelet analysis of the Kiso data (Figs. 4.2 to 4.10) shows the presence of a 2-3 year component also, whose amplitude and frequency vary during different hours of the night as well as during different epochs of the data series. At 2000 hr JST, this component is quasi-biennial with a frequency of 0.43 year^{-1} and is seen most prominently during the entire epoch (1979-1994). This component gradually becomes quasi-triennial with a frequency of 0.33 year^{-1} by 2200 hrs and its amplitude also decreases. It remains of the same nature until midnight and once again by 0200 hrs, it becomes quasi-biennial with a frequency of 0.43 year^{-1} and again its amplitude also increases. From 2200 hrs onwards, the variation is seen more prominently only during the years 1989-1992. In all the global power spectra, one can see this as one of the most prominent feature. However it is statistically significant at 2000, 0200 and 0300 hrs when it is of quasi-biennial nature. The quasi-triennial component at other times is statistically insignificant in the global power spectra. Fig. 4.12(c) shows the percentage amplitude of the quasi-biennial component. The amplitudes are above 95% confidence levels during 1987-1992, *i.e.,* in the second half of the data set. This shows that the mesospheric quasi-biennial component, arising from the leakage of the quasi-biennial oscillation of stratospheric zonal wind, also behaves differently during different solar cycles. The quasi-triennial component observed here must have arisen due to prolonged easterlies. At 2000 hrs the amplitude is in the range of 10%-13% during 1989-1992, which is stronger than the amplitude of the semi-annual component and around midnight it is slightly less and is of the order of 8%. By 0200 hrs it builds up again to 10%-13% and by 0300 hrs the power increases significantly and the peak in the global power spectrum is much above the 95% confidence level. These amplitudes are similar to what were obtained by *Fukuyama* (1977) at mid-latitudes north of $35^{\circ}N$. The wavelet power spectrum calculated from night mean intensities however detects a quasi-biennial component with a frequency of 0.4 year^{-1}. The amplitude is statistically significant (greater than 95%) for the second part of the dataset, *i.e.,* during solar cycle 22. An average of the peak frequencies from 2000 to 0300 hrs seems to appear as the peak frequency in this wavelet plot of night mean intensities.

Inspite of the fact that the amplitude of the quasi-biennial component is higher than the semi-annual component, during certain epochs, it could not be detected by (*Deutsch and Hernandez*, 2003) in their periodogram analysis of the same data. The data used by them was during low geomagnetic activity and in the present study the complete data has been taken, without considering the geomagnetic activity. The Kiso data was reanalyzed for low geomagnetic activity to address this problem and no significant differences from the original results have been found in the long term variations. Thus the present work reports for the first time the presence of a quasi-biennial component in the Kiso data that was not seen by *Deutsch and Hernandez* (2003).

This period when a QBO was found in airglow over Kiso also matches with the period when QBO was observed by *Kurosaki et al.* (1996) in the vertical eddy diffusivity over Shigaraki, a station very close to Kiso. The local time variation of the QBO in the present study shows that this pattern is also of tidal origin, similar to the annual and the semi-annual variations. The comparison with the long term variations of airglow in the vertical eddy diffusivity shows that in addition to tides, the mesospheric turbulence and breaking of gravity waves also effect these airglow variations.

4.4 Conclusions

The 16 year long dataset of OI 557.7 nm green line emission intensity, observed by ground based photometer over Kiso is reanalyzed using the continuous wavelet transform. Statistically significant semi-annual, annual and the quasi-biennial oscillations have been observed. It is seen that these oscillations are present at certain time of the night and during certain epochs. The nocturnal variation shows that the green line emission is influenced greatly by the tidal dynamics and by vertical eddy diffusion also. The semi-annual oscillation is thought to be produced by the diurnal tide and the annual oscillation is a result of the solar insolation (*Fukuyama*, 1977; *Deutsch and Hernandez*, 2003). QBO which was not detected by *Deutsch and Hernandez* (2003) is also seen over Kiso. Similar variations have been observed over Buckland Park (34.9°S, 138.6°E) near Adelaide, Australia, which is a geographically conjugate station. The inter-annual variabilities observed in the present study show that the long term variations are not permanent dynamical characteristics. Hence these results can be used to improve the present models of the mesosphere and the lower thermosphere like that of *Garcia and Solomon* (1985).

CHAPTER 5

Summary and Scope for Future Work

In the present work two issues related to the mesosphere and the lower thermosphere were studied. The first issue, which was dealt in this thesis is the mesospheric neutral turbulence and the second is the long term variations in the OI 557.7 nm mesospheric airglow emission.

Three rocket flights, carrying Langmuir probes, were conducted from Sriharikota and Thumba to measure electron density fluctuations to study the mesospheric turbulence. The electron densities measured are in good agreement with previous studies. Electron density irregularities were observed in 67–90 *km* region during all the three rocket flights. Strong positive and negative electron density gradients were present in vertical extents ranging between 2 and 12 *km* in the altitude range of 67–90 *km*. All scale sizes ranging from 1 *km* down to 10 *m* showed large percentage amplitudes in those altitude ranges where sharp electron density gradients were present. Some of the important results obtained in the present study are summarized as follows.

- The most important result of the present study is the detection of thin layers of turbulence with thickness as small as 100 *m*. This was possible due to the use of the continuous wavelet transform. Though their presence was proposed by numerical simulation studies, such thin layers could not be detected earlier due to the limitation of techniques employed for the analysis of rocket data, with typical altitude resolution of turbulence parameters of 1 km. This result therefore forms an experimental proof of the results from modelling studies.

- Turbulent layers of thickness ranging between 1.4 to 3.0 km were also observed which were sandwiched by these thin layers having layer thicknesses in the range of 100 to 200 m.
- During Flight 1, the energy dissipation rate ranged from 10–100 mW/kg in lower altitudes (75–84.5 km) and was much higher going upto 500 mW/kg in the higher altitudes (84.5–89 km). The corresponding heating rate ranged from 1 to 10 K/day in the lower altitudes and went upto 40 K/day in the higher altitudes.
- During Flight 2, the energy dissipation rate ranged from 1 to 30 mW/kg and the corresponding heating rates ranged from 0.1 to 3 K/day.
- During Flight 3, the energy dissipation rates were less than 10 mW/kg below 80 km and the heating rates were less than 1 K/day. Above 80 km the values were high and showed large variability.
- The turbulence observed in these flights is thought to be caused by gravity wave breaking. Large gravity wave activity was seen in Chaff winds, radar winds and also in SABER temperature profiles.
- Large gradients in the energy dissipation rate were seen at the edges of the turbulence region during Flight1. This shows that the edge region turbulence is anisotropic. No such gradients are seen during Flight 2.
- Flight 1 happened to be during magnetically disturbed period. Though, high turbulence was observed in the upper mesosphere during this flight, there is

no proof that the geomagnetic storm had caused any disturbance.

- During Flight 3, very high energy dissipation rates were found below and in the E-region ledge. Instabilities in the equatorial electrojet region could also have affected the electron density fluctuations in this region in addition to the neutral turbulence.

In order to identify the irregularities produced due to the neutral turbulence, it is suggested that (a) simultaneous measurements of plasma and neutral density be made along with neutral wind measurements using techniques such as Lithium vapor release, (b) use Langmuir probe with frequency response up to 5 kHz so that Kolmogorov microscales as small as 20 cm or so can be detected enabling construction of viscous dissipation regime spectra even at lower altitudes and (c) to use rocket range where there is a radar in the vicinity so that the same volume could be probed by rocket and radar.

A summary of the airglow emission study is as follows. The longest available data set of ground based measurements of OI 557.7 nm green line emission intensities over a mid-latitude station Kiso was studied for long term variations using the continuous wavelet transform. Statistically significant semi-annual, annual and quasi-biennial components have been observed in this study.

- The WINDII satellite measurements and TIME-GCM model predictions of a strong semi-annual component of O(^{1}S), coming from 96 km, at 2000 hrs LT is also found in the ground photometric data of Kiso. The rapid local time variation observed in these satellite and model results, i.e, the weakening of the semi-annual component from 2000 hrs to midnight and its complete disappearance by 0200 hrs is also observed in the Kiso data.

- The amplitude of the semi-annual component of the O(^{1}S) emission at 2000 hrs JST is statistically significant during epochs 1979-1982 and 1988-1991.

- During the epoch 1979-1982, the semi-annual component of O(^{1}S) emission dominated over the annual component.

- The annual component is statistically significant at all times except at midnight when it becomes weak and just touches the confidence level in the global power spectrum.

- The present analysis shows the presence of a very strong biennial component during the epoch 1989-1992, which corresponds to the period of solar cycle 22. This component also shows a large variation during the night with highest amplitudes observed around 2000 and 0200 hrs JST. Around midnight the component becomes quasi-triennial and its amplitude is weaker than the quasi-biennial amplitude.

- Tides are thought to be the source of the observed variations with time of these long term variabilities in the green line airglow emission. In addition, the vertical eddy diffusion and breaking of gravity waves might also be playing an important role.

The present study of airglow shows that there is a significant inter-annual variation in the semi-annual, annual and quasi-biennial components observed in the Kiso data. However, this study is over a single station. Long term satellite data and ground photometer data from a number of other stations needs to be studied to get a global picture of these variations.

The results of the present study regarding turbulence and airglow can be used as valuable inputs in future modelling studies to estimate the energy budget of the mesosphere and the lower thermosphere region for which both turbulence and airglow are significant contributors.

References

Altaisky, M. V. (2005), *Wavelets Theory Applications Implementations*, Universities Press.

Baldwin, M. P., L. J. Gray, T. J. Dunkerton, K. Hamilton, P. H. Haynes, W. J. Randel, J. R. Holton, M. J. Alexander, I. Hirota, T. Horinouchi, D. B. A. Jones, J. S. Kinnersley, C. Marquardt, K. Sato, , and M. Takahashi (2001), The quasi-biennial oscilaltion., *Rev. Geophys.*, *39*, 179229.

Barth, C. A. (1964), Three body reactions, *Ann. Geophys.*, *20*, 182–196.

Barth, C. A., and A. F. Hildebrandt (1961), The 5577 Å airglow emission mechanism, *J. Geophys. Res.*, *66*, 985–986.

Batchelor, G. K. (1953), *The theory of homogeneous turbulence*, Cambridge Science Classice, Cambridge University Press.

Bates, D. R. (1992), Nightglow emissions from oxygen in the lower thermosphere, *Planet. Space. Sci.*, *40*, 211–221.

Blix, T. A., E. V. Thrane, and Ø. Andreassen (1990), In situ measurements of the fine-scale structure and turbulence in the mesosphere and lower thermosphere by means of electrostatic positive ion probes, *J. Geophys. Res.*, *95*, 5533–5548.

Blood, S. P., J. D. Mitchell, C. L. Croskey, T. D. Raymund, E. V. Thrane, T. A. Blix, U. P. Hoppe, D. C. Fritts, and F. J. Schmidlin (1988), Studies of high latitude mesospheric turbulence by radar and rocket 2: Measurements of small scale turbulence, *J. Atmos. Terr. Phys.*, *50*, 963–976.

Brenton, J. G., and S. M. Silverman (1970), A study of the diurnal variations of the 5577 Å [OI] airglow emission at selected IGY stations, *Planet. Space Sci.*, *18*, 641–653.

Campbell, I. M., and C. N. Gray (1973), Rate constants for O(^{3}P) recombination and association with N(^{4}S), *Chemical Physics Letters*, *18*, 607–609.

Chakrabarty, D. K., G. Beig, J. S. Sidhu, and S. R. Das (1989), Fine scale structure and turbulence parameters in the equatorial middle atmosphere, *J. Atmos. Terr. Phys.*, *51*, 19–27.

Chakravarty, S. C., D. Jayati, and C. P. Revankar (1992), Climatology of long period oscillations in the equatorial middle atmosphere over Thumba, India, *Curr. Sci.*, *63*, 33–42.

Chakravarty, S. C., J. Datta, S. Kamala, and S. P. Gupta (2004), High-resolution mesospheric layer structures from MST radar backscatter echoes over low latitude, *J. Atmos. Sol. Terr. Phys.*, *66*, 859–866, doi:10.1016/j.jastp.2004.02.003.

Chen, F. F. (1983), *Introduction to Plasma Physics and Controlled Fusion*, vol. 1, second ed., Plenum Press.

Chen, W. Y. (1974), Energy dissipation rates of free atmospheric turbulence, *J. Atmos. Sci.*, *31*, 2222.

Chui, C. K. (1992), *An Introduction to Wavelets*, Academic Press.

Cogger, L., R. Elphinstone, and J. Murphree (1981), Temporal and latitudinal 5577 Å airglow variations, *Can. J. Phys.*, *59*, 1296–1307.

Croskey, C. L., J. D. Mitchell, R. A. Goldberg, T. A. Blix, M. Rapp, R. Latteck, M. Friedrich, and B. Smiley (2004), Coordinated investigation of plasma and neutral density fluctuations and particles during the MaCWAVE/MIDAS summer 2002 program, *Geophys. Res. Lett.*, *31*, L24S08, doi:10.1029/2004GL020169.

Danilov, A. D., and J. Lastovicka (2001), Effects of geomagnetic storms on the ionosphere and atmosphere, *Int. J. Geomagn. Aeron.*, *2*, 209–224.

Das, U., and H. S. S. Sinha (2008), Long term variations in oxygen green line emission over Kiso, Japan from ground photometric observations using continuous wavelet transform, *Revised version submitted to J. Geophys. Res.*

Deutsch, K. A., and G. Hernandez (2003), Long-term behavior of the OI 558 nm emission in the night sky and its aeronomical implications, *J. Geophys. Res.*, *108*, 1430, doi:10.1029/2002JA009611.

Donahue, T. M., B. Guenther, and R. J. Thomas (1973), Distribution of atomic oxygen in the upper atmosphere deduced from Ogo 6 airglow observations, *J. Geophys. Res.*, *78*, 6662–6689.

Farge, M. (1992), Wavelet transforms and their applications to turbulence, *Annu. Rev. Fluid Mech.*, *24*, 395–457.

Fritts, D. C., C. Bizon, J. A. Werne, and C. K. Meyer (2003), Layering accompanying turbulence generation due to shear instability and gravity-wave breaking, *J. Geophys. Res.*, *108*, 8452, doi:10.1029/2002JD002406.

Fukao, S., T. Sato, R. M. Harper, and S. Kato (1980), Radio waves scattering from the tropical mesosphere observed with the Jicamarca radar, *Radio Sci.*, *15*, 447–457.

Fukao, S., M. D. Yamanaka, N. Ao, W. K. Hocking, T. Sato, M. Yamamoto, T. Nakamura, T. Tsuda, and S. Kato (1994), Seasonal variability of vertical eddy diffusivity in the middle atmosphere 1. Three-year observations by the middle and upper atmosphere radar, *J. Geophys. Res.*, *99*, 18,973–18,987.

Fukuyama, K. (1976), Airglow variations and dynamics in the lower thermosphere and upper mesosphere - I. Diurnal variation and its seasonal dependency, *J. Atmos. Terr. Phys.*, *38*, 1279–1287.

Fukuyama, K. (1977), Airglow variations and dynamics in the lower thermosphere and upper mesosphere - II. Seasonal and long-term variations, *J. Atmos. Terr. Phys.*, *39*, 1–14.

Gage, K. S., and B. B. Balsley (1980), On the scattering and reflection mechanisms contributing to clear air radar echoes from the troposphere, stratosphere and mesosphere, *Radio Sci.*, *15*, 243–257.

Garcia, R. R., and S. Solomon (1985), The effect of breaking gravity waves on the dynamics and chemical composition of the mesosphere and lower thermosphere, *J. Geophys. Res.*, *90*, 3850–3868.

Giraud, A., and M. Petit (1978), *Ionospheric Techniques and Phenomena*, *Geophysics and Astrophysics Monographs*, vol. 13, first ed., D. Reidel Publishing Company.

Goldberg, R. A., D. C. Fritts, H. G. Chou, J. R. Barcus, and F. J. Schmidlin (1988), Studies of high latitude mesospheric turbulence by radar and rocket 1. Energy deposition and wave structure, *J. Atmos. Terr. Phys.*, *50*, 951–961.

Goldberg, R. A., G. A. Lehmacher, F. J. Schmidlin, D. C. Fritts, J. D. M. andC. L. Croskey, M. Friedrich, and W. E. Swartz (1997), Equatorial dynamics observed by rocket, radar and satellite during the CADRE/MALTED campaign:1. Programmatics and small-scale fluctuations, *J. Geophys. Res.*, *102*, 26,179–26,190.

Hedin, A. E. (1991), Extension of the MSIS thermosphere model into the middle and lower atmosphere, *J. Geophys. Res.*, *96*, 1159–1172.

Hedin, A. E., E. L. Fleming, A. H. Manson, F. J. Schmidlin, S. K. Avery, R. R. Clark, S. J. Franke, G. J. Fraser, T. Tsuda, F. Vial, and R. A. Vincent (1996), Empirical wind model for the upper, middle and lower atmosphere, *J. Atmos. Terr. Phys.*, *58*, 1421–1447.

Heisenberg, W. (1948), Zur statistischen theorie der turbulenz, *Z. Physik.*, *124*, 628–657.

Heisenberg, W. (1949), On the theory of statistical and isotropic turbulence, *Proceedings of the Royal Society*, *195*, 402–406.

Hill, R. J., and S. F. Clifford (1978), Modified spectrum of atmospheric temperature fluctuations and its application to optical propagation, *J. Opt. Sci. Am.*, *68*, 892–899.

Hines, C. O. (1960), Internal atmospheric gravity waves at ionospheric heights, *Can. J. Phys.*, *38*, 1441–1481.

Hocking, W. K. (1982), On the extension of atmospheric turbulence parameters from radar backscatter Doppler spectra -1: Theory, *J. Atmos. Terr. Phys.*, *45*, 89–102.

Hocking, W. K. (1990), Turbulence in the region 80-120 km, *Adv. Space Res.*, *10*, (12)153–(12)161.

Hocking, W. K., and J. Röttger (2001), The structure of turbulence in the middle and lower atmosphere seen by and deduced from MF, HF and VHF radar, with special emphasis on small-scale features and anisotropy, *Ann. Geophys.*, *19*, 933944.

Kamala, S., D. NarayanaRao, S. C. Chakravarty, J. Datta, and B. S. N. Prasad (2003), Vertical structure of mesospheric echoes from the indian MST radar, *J. Atmos. Sol. Terr. Phys.*, *65*, 71–83.

Killeen, T. L., and R. M. Johnsson (1995), Upper atmospheric waves, turbulence, and winds: Importance for mesospheric and thermospheric studies, *Rev. Geophys.*, *33 Suppl.*

Kubo, K., T. Sugiyama, T. Nakamura, and S. Fukao (1997), Seasonal and interannual variability of mesospheric echoes observed with the Middle and Upper atmosphere radar during 1986-1995, *Geophys. Res. Lett.*, *24*, 1211–1214.

Kumar, G. K., M. V. Ratnam, A. K. Patra, V. J. Rao, S. V. B. Rao, and D. N. Rao (2007), Climatology of the low-latitude mesospheric echo characteristics observed by Indian MST radar, *J. Geophys. Res.*, *112*, D06109, doi:10.1029/2006JD007609.

Kurosaki, S., M. D. Yamanaka, H. Hashiguchi, T. Satot, and S. Fukao (1996), Vertical eddy diffusivity in the lower and middle atmosphere : a climatology based on the MU radar observations during 1986-1992, *J. Atmos. Terr. Phys.*, *58*, 727–734.

Larsen, M. F. (2002), Winds and shears in the mesosphere and lower thermosphere: Results from four decades of chemical release wind measurements, *J. Geophys. Res.*, *107*, 28(1)–28(14), doi:10.1029/2001JA000218.

Lehmacher, G. A., R. A. Goldberg, F. J. Schmidlin, C. L. Croskey, J. D. Mitchell, and W. E. Swartz (1997), Electron density fluctuations in the equatorial mesosphere: Neutral turbulence or plasma instabilities, *Geophys. Res. Lett.*, *24*, 1715–1718.

Lehmacher, G. A., C. L. Croskey, J. D. Mitchell, M. Friedrich, F.-J. Lübken, M. Rapp, E. Kudeki, and D. C. Fritts (2006), Intense turbulence observed above a mesospheric temperature inversion at equatorial latitude, *Geophys. Res. Lett.*, *33*, L08808, doi:10.1029/2005GL024345.

Lily, D. K., D. E. Waco, and S. I. Adelfang (1974), Stratospheric mixing estimated from high-altitude turbulence measurements, *J. Appl. Meteorol.*, *13*, 488–493.

Lübken, F. J. (1992), On the extraction of turbulent parameters from atmospheric density fluctuations, *J. Geophys. Res.*, *97*, 20,385–20,395.

Lübken, F. J. (1997), Seasonal variation of turbulent energy dissipation rates at high latitudes as determined by in situ measurements of neutral density fluctuations, *J. Geophys. Res.*, *102*, 13,441–13,456.

Lübken, F.-J., W. Hillert, G. Lehmacher, and U. von Zahn (1993), Experiments revealing small impact of turbulence on the energy budget of the mesosphere and the lower thermosphere, *J. Geophys. Res.*, *98*, 20,369–20,384.

Lumley, J. L. (1964), The spectrum of nearly inertial turbulence in a stably stratified fluid, *J. Atmos. Sci.*, *21*, 99–102.

McDade, I., D. P. Murtagh, R. G. H. Greer, P. H. G. Dickinson, G. Witt, J. Stegman, E. J. Llewellyn, I. Thomas, and D. B. Jenkins (1986), ETON 2: Quenching parameters for the propose precursors of $O_2(^1\sum_g^+)$ and O (^{1}S) in the terrestrial nightglow, *Planet. Space. Sci.*, *34*, 789–800.

McDade, I. C. (1998), The photochemistry of the MLT Oxygen airglow emissions and the expected influences of tidal perturbations., *Adv. Space Res.*, *21*, 787–794.

McLandress, C., M. J. Alexander, and D. L. Wu (2000), Microwave Limb Sounder observations of gravity waves in the stratosphere: A climatology and interpretation, *J. Geophys. Res.*, *105*, 11,947–77,967.

Melo, S. M. L., H. Takahashi, B. R. Clemesha, P. P. Batista, and D. M. Simonich (1996), Atomic oxygen concentrations from rocket airglow observations in the equatorial region, *JATP*, *58*, 1935–1942.

Meriwether, J. W., and A. J. Gerrard (2004), Mesosphere inversion layers and stratosphere temperature enhancements, *Rev. Geophys.*, *42*, RG3003, doi:10.1029/2003RG000133.

Perrier, V., T. Philipovitch, and C. Basdevant: (1995), Wavelet spectra compared to Fourier spectra, *J. Math. Phys.*, *36*, 1506–1519.

Pope, S. B. (2000), *Turbulent Flows*, Cambridge University Press.

Prakash, S., S. P. Gupta, B. H. Subbaraya, and R. Pandey (1980), A review of the electron density irregularities in the equatorial D & E region, *Adv. Space Explorations*, *8*, 3–16.

Rajesh, P. K., J. Y. Liu, H. S. S. Sinha, S. B. Banerjee, R. N. Misra, N. Dutt, and M. B. Dadhania (2007), Observations of plasma depletions in 557.7-nm images over Kavalur, *J. Geophys. Res.*, *112*, A07307, doi:10.1029/2006JA012055.

Rao, D. N., M. V. Ratnam, T. N. Rao, and S. V. B. Rao (2001), Seasonal variation of vertical eddy diffusivity in the troposphere, lower stratosphere and mesosphere over a tropical station, *Ann. Geophys.*, *19*, 975–984.

Rao, P. B., A. R. Jain, P. Kishore, P. Balamuralidhar, S. H. Damle, and G. Viswanathan (1995), Indian MST radar, I: System description and sample vector wind measurements in ST mode, *Radio Sci.*, *30*, 1125–1138.

Rapp, M., B. Strelnikov, A. Müllemann, F.-J. Lübken, and D. C. Fritts (2004), Turbulence measurements and implications for gravity wave dissipation during the MaCWAVE/MIDAS rocket program, *Geophys. Res. Lett.*, *31*, L24S07.

Ratnam, M. V., D. N. Rao, T. N. Rao, M. Krishnaiah, Y. B. Kumar, V. S. Kumar, and P. B. Rao (2002), Coordinated MST radar and lidar observations for the study of mesospheric structures over a tropical station, *J. Atmos. Sol. Terr. Phys.*, *64*, 349358.

Reid, I. M., and J. M. Woithe (2007), The variability of 558 nm OI nightglow intensity measured over Adelaide, Australia, *Adv. Space Res.*, *39*, 12371247.

Royrvik, O., and L. G. Smith (1984), Comparison of mesospheric VHF radar echoes and rocket probe electron concentration measurements, *J. Geophys. Res.*, *89*, 9014–9022.

Sasi, M. N., and L. Vijayan (2001), Turbulence characteristics in the tropical mesosphere as obtained by MST radar at Gadanki (13.5°N, 79.2°E), *Adv. Space Res.*, *19*, 1019–1025.

Schunk, R. W., and A. F. Nagy (2000), *Ionospheres: Physics, Plasma Physics, and Chemistry*, Cambridge Atmospheric and Space Science Series, Cambridge University Press.

Shepherd, G. G., C. McLandress, and B. H. Solheim (1995), Tidal influence on O(^{1}S) airglow emission rate distributions at the geographic equator as observed by WINDII, *Geophys. Res. Lett.*, *22*, 275–278.

Shepherd, G. G., R. G. Roble, C. McLandress, and W. E. Ward (1997), WINDII observations of the 558 nm emission in the lower thermosphere: The influence of dynamics on composition, *J. Atmos. Sol. Terr. Phys.*, *59*, 655–667.

Shepherd, G. G., R. G. Roble, S.-P. Zhang, C. McLandress, and R. H. Wiens (1998), Tidal influence on midlatitude airglow: Comparison of satellite and ground-based observations with TIME-GCM predictions, *J. Geophys. Res.*, *103*, 14,741–14,751.

Shepherd, G. G., G. Liu, and R. G. Roble (2005), Large-scale circulation of atomic oxygen in the upper mesosphere and lower thermosphere, *Adv. Space Res.*, *35*, 1945–1950.

Shepherd, M. G., G. Liu, and G. G. Shepherd (2006), Mesospheric semiannual oscillation in temperature and nightglow emission, *J. Atmos. Sol. Terr. Phys.*, *68*, 379–389.

Sheth, R., E. Kudeki, G. Lehmacher, M. Sarango, R. Woodman, J. Chau, L. Guo, , and P. Reyes (2006), A high-resolution study of mesospheric fine structure with the Jicamarca MST radar, *Ann. Geophys.*, *24*, 1281.

Shiokawa, K., and Y. Kiyama (2000), A search for the springtime transition of lower thermospheric atomic oxygen using long-term midlatitude airglow data, *J. Atmos. Sol. Terr. Phys.*, *62*, 1215–1219.

Shur, G. H. (1962), *Tr. Tsent. Aerolog. Obs.*, *43*, 79.

Sinha, H. S. S. (1976), Studies in equatorial aeronomy, Ph.D. thesis, Gujarat University.

Sinha, H. S. S. (1992), Plasma density irregularities in the equatorial D - region produced by neutral turbulence, *J. Atmos. Terr. Phys.*, *54*, 49–61.

Sinha, H. S. S., and S. Prakash (1995), Electron densities in the equatorial lower ionosphere over Thumba and Shar, *Adv. Space Res.*, *18*, 311–318.

Slanger, T. G., P. C. Cosby, and D. L. Huestis (2004), Co-variation of nightglow emission from the $O_2(A^3\Sigma_u^+)$ and $O_2(c^1\Sigma_u^-)$ states and the oxygen green line, observed with the Keck I/II telescopes, *J. Atmos. Sol. Terr. Phys.*, *66*, 617–622.

Smith, L. G. (1969), Small rocket instrumentation, *Tech. rep.*

Strelnikov, B., M. Rapp, and F.-J. Lübken (2003), A new technique for the analysis of neutral air density fluctuations measured in situ in the middle atmosphere., *Geophys. Res. Lett.*, *30*, 1–5, doi:10.1029/2003GL018271.

Thrane, E. V., and B. Grandal (1981), Observations of the fine scale structure in the mesosphere and lower thermosphere, *J. Atmos. Terr. Phys.*, *43*, 179–189.

Thrane, E. V., Ø. Andreassen, T. Blix, B. Grandal, A. Brekke, C. R. Philbrick, F. J. Schmidlin, H. U. Widdel, U. von Zahn, and F. J. Lübken (1985), Neutral air turbulence in the upper atmosphere observed during the energy budget campaign, *J. Atmos. Terr. Phys.*, *47*, 243–264.

Thrane, E. V., T. A. Blix, C. Hall, , T. L. Hansen, U. V. Zahn, , W. Meyer, P. Czechowsky, G. Schmidt, , H. U. Widdel, and A. Neumann (1987), Small scale structure and turbulence in the mesosphere and lower thermosphere at high latitudes in winter, *J. Atmos. Terr. Phys.*, *49*, 751–762.

Torrence, C., and G. P. Compo (1998), A practical guide to wavelet analysis, *Bull. Amer. Meteorol. Soc.*, *79*, 61–78.

Ward, W. E. (1999), A simple model of diurnal variations in the mesospheric oxygen nightglow, *Geophys. Res. Lett.*, *26*, 3565–3568.

Weinstock, J. (1981a), Energy dissipation rates of turbulence in the stable free atmosphere, *J. Atmos. Sci.*, *38*, 880–883.

Weinstock, J. (1981b), Vertical turbulence diffusivity for weak or strong stable stratification, *J. Geophys. Res.*, *86*, 9925–9928.

Xue, X., W. Wan, J. Xiong, and X. Dou (2007), Diurnal tides in mesosphere/low-thermosphere during 2002 at Wuhan (30.6°N, 114.4°E) using canonical correlation analysis, *J. Geophys. Res.*, *112*, D06104, doi:10.1029/2006JD007490.

Yee, J.-H., G. Crowley, R. G. Roble, W. R. Skinner, M. D. Burrage, and P. B. Hays (1997), Global simulations and observations of $O(^1S)$, $O_2(^1\Sigma)$ and OH mesospheric nightglow emissions, *J. Geophys. Res.*, *102*, 19,949 – 19,968.

Presentations in Conferences/Symposia/Workshops

i. **Uma Das**, H. Chandra, H. S. S. Sinha, R. N .Misra, S. R. Das, Jayati Datta, S. C. Chakravarty, A. K. Patra, N. Venkateswara Rao, D. Narayan Rao, "Mesospheric turbulence study from coordinated rocket and MST radar measurements over Indian low latitude region", Accepted for Oral presentation at 37^{th} COSPAR Scientific Assembly, July 13-20, 2008, Montreal, Canada.

ii. **Uma Das** and H. S. S. Sinha, "Long term variations in oxygen green line emission over Kiso from ground based observations using Continuous Wavelet Transform", International Symposium on Equatorial Aeronomy - 12 (ISEA-12), May 18-24, 2008, Crete, Greece.

iii. H. S. S. Sinha, **Uma Das**, R. N. Misra, M. B. Dadhania, Swaroop Banerjee and N. Dutt, "Study of Mesospheric Turbulence using Rocket-borne Electron Density Measurements", International Symposium on Equatorial Aeronomy - 12 (ISEA-12), May 18-24, 2008, Crete, Greece.

iv. H. Chandra, H. S. S. Sinha, R. N .Misra, S. R. Das, **Uma Kota**, D. Narayan Rao, A. K. Patra, S. C. Chakravarty, Jayati Datta, "Mesospheric Turbulence Studies using Rocket and Indian MST Radar", Proceedings of the Eleventh-International Workshop on Technical and Scientific aspects on MST RADAR

(MST11), December 11-15, 2006, Gadanki, India.

v. H. Chandra, H. S. S. Sinha, R. N .Misra, S. R. Das, **Uma Kota**, Jayati Datta, S. C. Chakravarty, A. K. Patra, D. N. Rao, "Mesospheric turbulence studies using rocket and MST radar over low latitude: campaign of July, 2004", 36th COSPAR Scientific Assembly, July 16-23, 2006, Beijing, China.

vi. H. Chandra, H. S. S. Sinha, R. N .Misra, S. R. Das, **Uma Kota**, D. Narayan Rao, A. K. Patra, S. C. Chakravarty, Jayati Datta, Geetha Ramkumar, C. V. Devasia, S. Gurubaran, S. Alex, A. R. Jain, "Mesospheric turbulence and stratification studies using rocket-borne, MST radar and other ground based experiments", 11th International Symposium on Equatorial Aeronomy, May 9-14, 2005, Taipei, Taiwan, R.O.C.

vii. H. S. S. Sinha, P. K. Rajesh, J. Y. Liu, R. N. Misra, S. B. Banerjee, N.Dutt, M. B. Dadhania, **Uma Kota**, "All Sky Imaging of Plasma Depletions Over Indian Zone Durng Solar Maximum", 11th International Symposium on Equatorial Aeronomy, May 9-14, 2005, Taipei, Taiwan, R.O.C.

Publications

i. **Uma Das** and H. S. S. Sinha, "Long term variations in oxygen green line emission over Kiso, Japan from ground photometric observations using continuous wavelet transform", *Revised version submitted to J. Geophys. Res.*

ii. H. Chandra, H. S. S. Sinha, **Uma Das**, R. N. Misra, S. R. Das, Jayati Datta, S. C. Chakravarty, A. K. Patra, N. Venkateswara Rao and D. Narayana Rao, "First mesospheric turbulence study made using coordinated rocket and MST radar measurements over Indian low latitude region", *Revised version submitted to Ann. Geophys.*

iii. **Uma Das** and H. S. S. Sinha, "Studies of Neutral Turbulence from Electron Density Measurements in Low Latitude Mesosphere using Wavelet Analysis", *To be submitted shortly to J. Geophys. Res.*

iv. **Uma Das**, H. S. S. Sinha, R. N. Misra, M. B. Dadhania, Swaroop Banerjee and N. Dutt "Study of Equatorial Mesospheric Turbulence using Rocket-borne Electron Density Measurements", *To be submitted shortly to Ann. Geophys.*

Memoirs

A few glimpses of my work and myself during my Ph.D. tenure at PRL. (*a*) Our team with the rocket and the MTS payload that is ready to fly from Sriharikota, (*b*) MTS scientific payload consisting of the Langmuir probe and the spherical probe, (*c*) Our team along with the RSR members at the rocket launcher, Sriharikota, (*d*) RH 200 take off (*e*) RH 300 take off from FM building, (*f*) During the testing of ABHA payload, (*g*) in PRL's lab with the team, (*h*) Calibrating the photometers with Misraji and Sinhaji, (*i*) The ABHA payload with Sinhaji and Gohilji, (*j*) With my poster during ISEA-12, at Greece, (*k*) During my oral presentation at ISEA-12, Greece, (*l*) Doing Kuchipudi (India Today, August 2006 and PRL News, January 2007), (*m*) With Mom, Dad and Kousi, (*n*) Srikanth, (*o*) My marriage with Sanat, (*p*) Bindu with Adi, (*q*) Adi, Sanat and myself.


a
b
c
d
e
f
g
h
i
j
k
Long term variations in oxygen green line emission over Kiso from ground based observations using Continuous Wavelet Transform
Uma Das* and H.S.S. Sinha
Physical Research Laboratory
Ahmedabad, India
l
m
n
o
p
q